2015

Design and Optimization of Nanoplasmonic Waveguide Devices

Pouya Dastmalchi
Louisiana State University and Agricultural and Mechanical College, pouya.dastmalchi@gmail.com

DESIGN AND OPTIMIZATION OF NANOPLASMONIC WAVEGUIDE DEVICES

A Dissertation

Submitted to the Graduate Faculty of the
Louisiana State University and
Agricultural and Mechanical College
in partial fulfillment of the
requirements for the degree of
Doctor of Philosophy

in

The School of Electrical Engineering and Computer Science

by
Pouya Dastmalchi
B.Sc., Khajeh Nasir Toosi University of Technology, 2007
M.Sc., Khajeh Nasir Toosi University of Technology, 2010
December 2015

Dedicated to my parents

تقدیم به

پدر و مادر عزیزم

که درس زندگی و محبت را به من آموخته اند.

Acknowledgments

First I would like to acknowledge my advisor Dr. Georgios Veronis for his patience, support and excellent guidance over the years. Without his insightful and innovative ideas, this thesis could not have been accomplished.

It is not easy to appreciate the invaluable support and dedication I received from my parents, Sorour and Ali, to whom this dissertation is dedicated. They taught me the value of education and hard work. I can never repay them enough for what they have done for me and I'm truly blessed to have them as my parents. Also I am grateful to my lovely sister Nasim and supportive brother Reza who always do their best for my success.

I would like to thank Professors Jin-Woo Choi, Theda Daniels-Race, Jonathan P. Dowling, and Stephen Shipman for being members of my general and final examination committees and providing me with their thoughtful comments and suggestions.

Special thanks to my colleagues at Louisiana State University for their friendship and helps, Yin Huang, Ali Haddadpour, and Amirreza Mahigir. I am also grateful to my friends Erfan Soltanmohammadi, Kasra Fattah-Hesary, and Ata Mesgarnejad.

I would like also to thank the administrative team at the Division of Electrical and Computer Engineering, Louisiana State University. I wish to express my appreciation to Beth R. Cochran for her constant support.

Table of Contents

Acknowledgments iii
Abstract vi

Chapter
1 Introduction 1
1.1 Historical background and motivation 1
1.2 Outline of the Dissertation 9

2 Compact Multisection Cavity Switches in Metal-Dielectric-Metal Plasmonic Waveguides 11
2.1 Introduction 11
2.2 Results 12

3 Efficient Design of Nanoplasmonic Waveguide Devices Using the Space Mapping Algorithm 24
3.1 Introduction 24
3.2 Algorithm 25
3.2.1 Aggressive space mapping 26
3.2.2 Parameter extraction 28
3.2.3 Application of the space mapping algorithm to design of nanoplasmonic waveguide devices 29
3.3 Results 30
3.3.1 MDM waveguide side-coupled to two MDM stub resonators 30
3.3.2 MDM waveguide side-coupled to two arrays of MDM stub resonators 37
3.3.3 Two nanorods juxtaposed in parallel in a waveguide 40
3.3.4 Emulation of 2D MDM plasmonic waveguide devices with 3D coaxial waveguide devices 46

4 Sensitivity Analysis of Active Nanophotonic Devices 51
4.1 Introduction 51
4.2 Derivation of the analytical sensitivity formula 53
4.3 Numerical implementation 62
4.3.1 2D example 62
4.3.2 Sensitivity at resonance 68
4.3.3 3D example 78

5 Concluding Remarks and Recommended Future Work 89
5.1 Conclusions 89
5.2 Recommended future work 91

References 93

Appendix
A Proof of Eq. 2.1 102
B Transmission Line Models 106
C Proof of Eq. 4.25 112
D Boundary Conditions 116
Vita 119

Abstract

In this dissertation, we introduce compact absorption switches consisting of plasmonic metal-dielectric-metal (MDM) waveguides coupled to multisection cavities. The optimized multisection cavity switches lead to greatly enhanced modulation depth compared to optimized conventional Fabry-Perot cavity switches. We find that the modulation depth of the optimized multisection cavity switches is greatly enhanced compared to the optimized conventional Fabry-Perot cavity switches due to the great enhancement of the total electromagnetic field energy in the cavity region.

We then investigate how to improve the computational efficiency of the design of nanoplasmonic devices. More specifically, we show that the space mapping algorithm, originally developed for microwave circuit optimization, can enable the efficient design of nanoplasmonic waveguide devices which satisfy a set of desired specifications. Space mapping utilizes a physics-based coarse model to approximate a fine model accurately describing a device. Here the fine model is a full-wave finite-difference frequency-domain (FDFD) simulation of the device, while the coarse model is based on transmission line theory. We demonstrate that, when the iterative space mapping algorithm is used, it converges fast to a design which meets all the specifications. In addition, full-wave FDFD simulations of only a few candidate structures are required before the iterative process is terminated. Use of the space mapping algorithm therefore results in large reductions in the required computation time when compared to any direct optimization method of the fine FDFD model.

We finally introduce a method for the sensitivity analysis of active nanophotonic waveguide devices to variations in the dielectric permittivity of the active material. More specifically, we present an analytical adjoint sensitivity method for the power transmission coefficient of nano optical devices, which is directly derived from Maxwell's equations, and is not based on any specific numerical discretization method. We apply the derived formula to

calculate the sensitivity of the power transmission coefficient with respect to the real and imaginary parts of the dielectric permittivity of the active material for two-dimensional and three-dimensional plasmonic devices, and compare the results with the ones obtained by directly calculating the sensitivity.

Chapter 1
Introduction

1.1 Historical background and motivation

Moore's law has predicted the advancement of semiconductor devices for almost half a century so far. Although the main observation of Moore's law is related to the number of transistors in dense integrated circuits, it could also have implications for the reduction of cost and power consumption in integrated circuits. Not only this law was applicable to the CMOS integrated technology, but it has also been shown that previous computational technologies followed almost the same trend (Figure 1.1) [1].

Considering integrated circuits as the fifth generation of computational technologies, one of the most promising technologies which could be called as the sixth generation is photonics [2]. Because of its potentially small size, high speed, and low power consumption many companies and research institutions are investigating photonic integrated circuits (PICs) as the next generation technology which can still satisfy Moore's law. Nevertheless, any technology encounters its own problems and photonics is not an exception. Diffraction limit of light is a significant problem which puts an upper bound to the integration of photonic devices [3, 4]. For telecommunication wavelengths the smallest photonic device which can efficiently guide and modulate light cannot have dimensions smaller than almost 200 nm [5]. Figure 1.2(a) clearly demonstrates this limitation for conventional dielectric waveguides [4]. This issue challenged researchers to find a way to break this diffraction limit.

Metallic nanophotonics and plasmonics have merged recently to overcome the above mentioned significant obstacle because they have the potential to lead to nanoscale devices not limited by diffraction. The interface between a metal and a dielectric supports the so-called surface plasmon-polariton (SPP) modes of electromagnetic waves cou-

pled to the collective oscillations of the electron plasma in the metal. When the operating frequency approaches the surface plasmon frequency, the field profile of these modes is highly confined in a deep subwavelength region at the metal-dielectric interface [6, 7, 8, 9, 10, 11, 12, 13, 4, 14, 3]. Therefore, the emerging area of plasmonics enables manipulating light at the nanosacle, and could potentially address the technological challenge described in the previous paragraph. In Figure 1.2(b) plasmonic metal nanowires with different core diameters are demonstrated. This figure shows that, in contrast to the behavior of dielectric fibers [Figure 1.2(a)], when the diameter of the nanowire d is decreased below the wavelength of the SPP, not only the modal size does not increase but it also experiences a strong localization [4]. This feature significantly helps to achieve higher order of miniaturization and integration of optical devices. The only new hurdle with metallic nanophotonic devices is the unavoidable ohmic loss which is introduced because of the metallic layer.

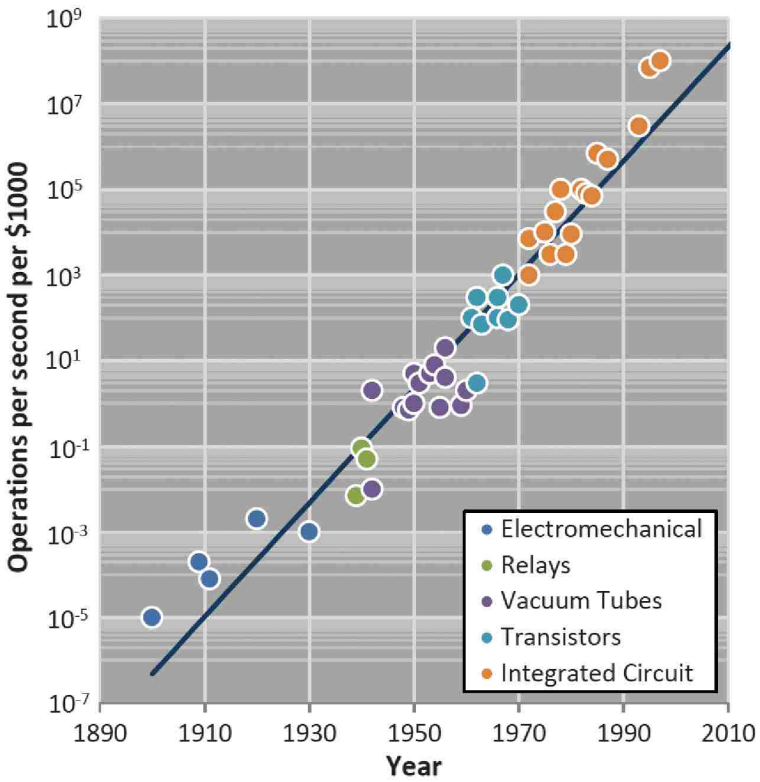

Figure 1.1: Graph illustrating the scaling of computational technologies over time. Integrated circuits represent the fifth generation of scaling. To continue the scaling into the future a new technology platform should be investigated. (Adapted from Moore's Law: The Fifth Paradigm [1]).

As for any other generation of technology for nanophotonics, in addition to developing passive devices, there is another challenge which is achieving active or dynamic devices. A fundamental function of any integrated circuit is to encode or route the data, which

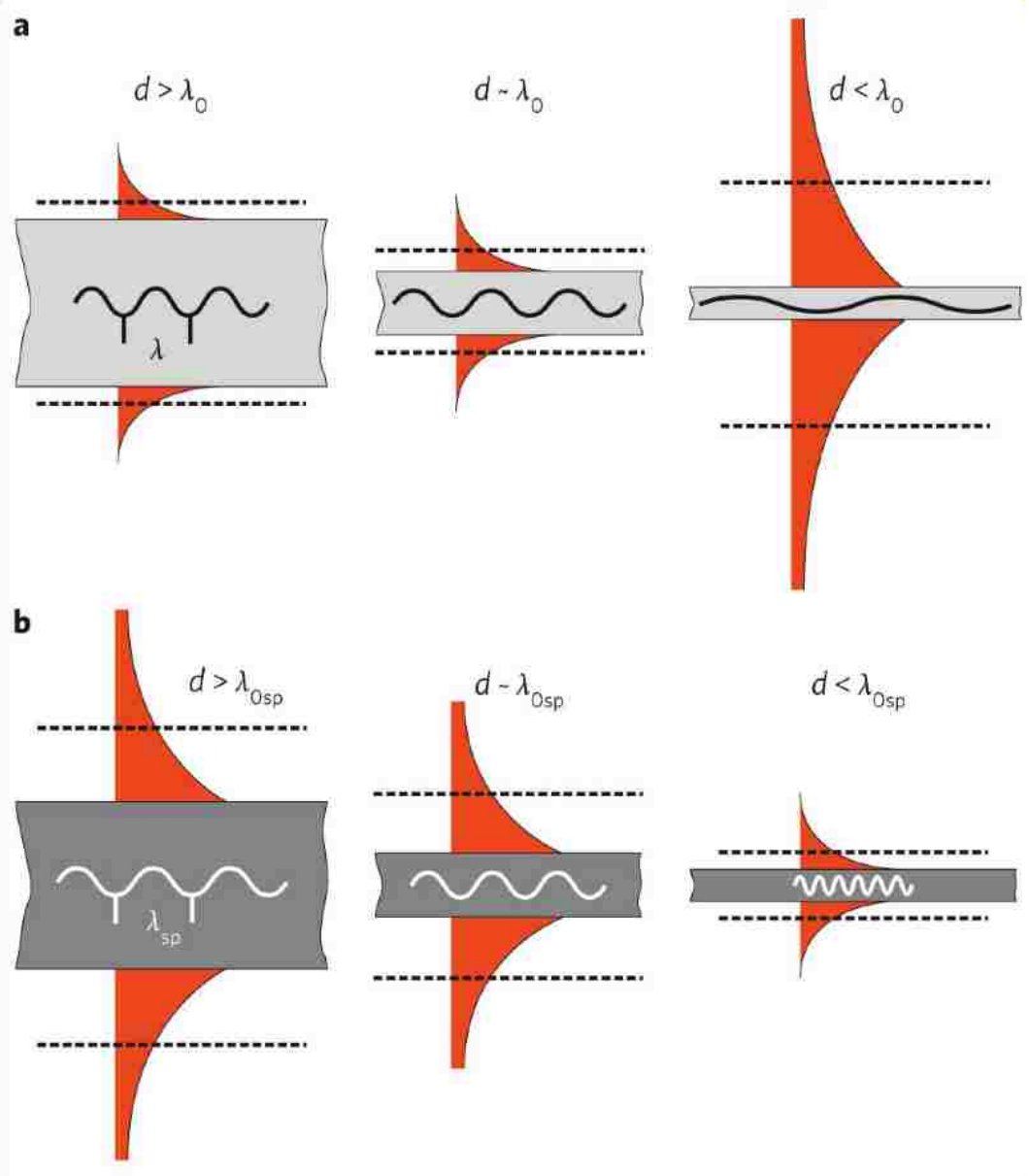

Figure 1.2: Typical field structures, localization and wavelengths of the fundamental modes guided by (a) dielectric fibers and (b) cylindrical metal nanowires for different core diameters. Here, λ_0 and λ_{0sp} are the mode wavelengths for infinite-diameter fibers and metal nanowires, respectively. The dashed horizontal lines show the localization of the mode at the $1/e$ level of maximum field amplitude [4].

can be considered as a switching or modulation function. Similar devices with analogous functionality are needed in PICs.

In general, there are two options (electrical and optical) for each of the control signal and the carrier. So, overall there are four options for switching and the type of the device depends on whether the modulation is being done on electrical or optical signal, and the switching is implemented using an optical or electrical gate [15, 16]. Figure 1.3 shows these four cases.

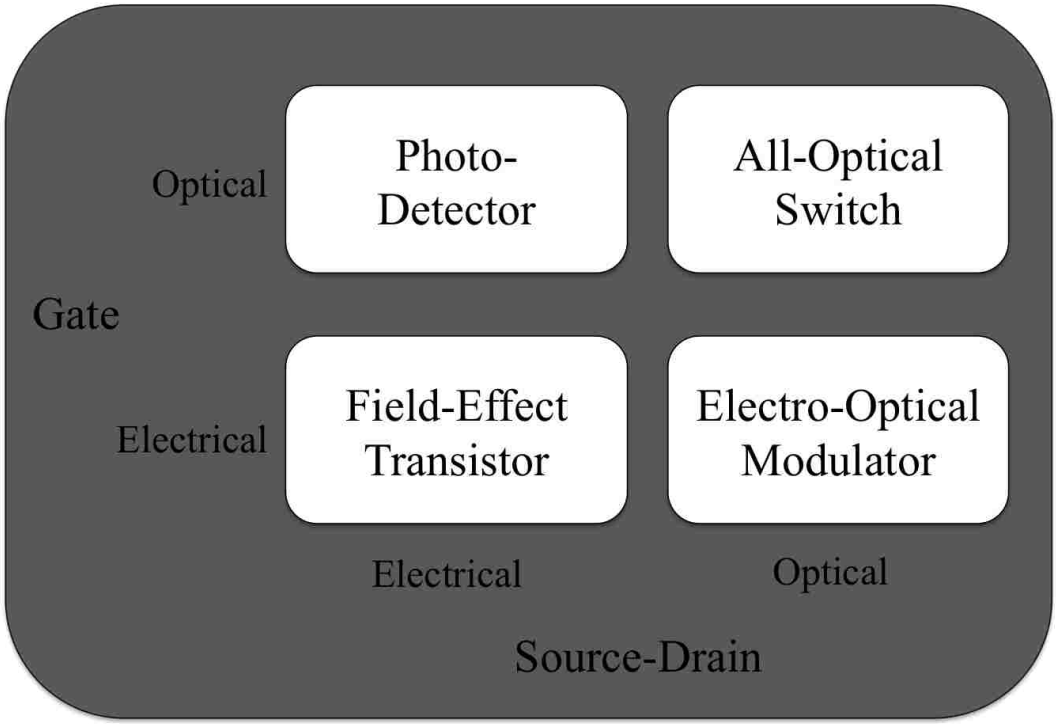

Figure 1.3: In general, there are four possibilities for logic using optics and electronics. For photonic integrated circuits, three options are of interest; electrical data can be encoded onto an optical beam via an electro-optic modulator [15].

For example, in field-effect transistors the electrical signal is modulated using an electrical gate, while photo-detectors resemble optical transistors in which the electrical signals are switched by optical gates [17, 18]. Nonlinearity is commonly used for optical switching of optical signals but usually a long interaction length or a high optical power are required to obtain a sufficient gating effect. This is the consequence of weak optical nonlinear ef-

fects. Since optical nonlinearities are weak, high intensity optical power sources are needed such as high power laser beams [19, 20]. The last approach to encode optical signal is to use an electrical gate [21, 22, 23, 24]. Therefore, electro-optic modulators are fundamental and essential components of photonic integrated circuits, which can also be considered as an interconnect between electronic and optical information. A commonly used electro-optic modulator is shown schematically in Figure 1.4. An electrically encoded signal going through the gate of an electro-optic modulator modulates an optical signal such as a continuous wave (cw) laser beam. More specifically, the data carrying voltage applied to the gate encodes the continues wave optical laser beam by changing the refractive index of the optical mode. This approach depending on whether the real or imaginary part of the refractive index changes can lead to two different modulators, interferometer type phase modulator (Mach-Zehnder) [25] or electroabsorption modulator [26, 27, 15].

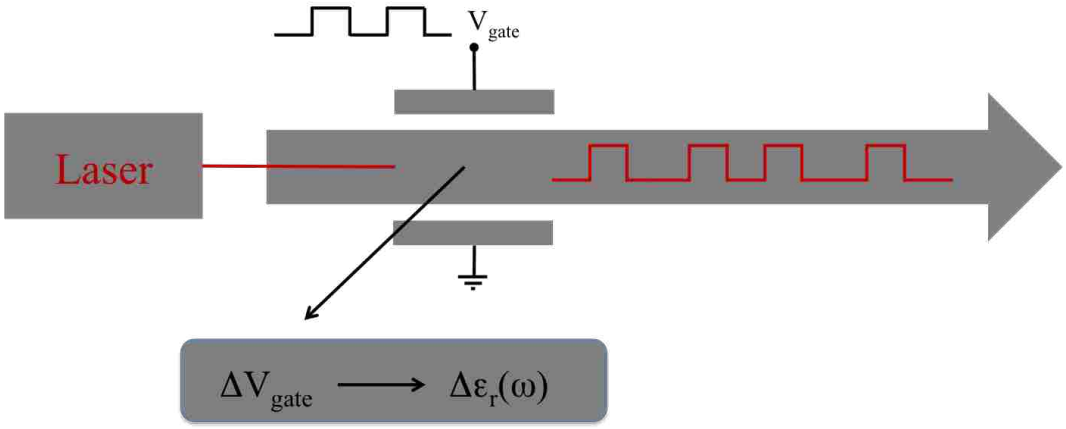

Figure 1.4: Schematic of the electro-optic modulator. It shows how an encoded applied voltage to the gate leads to a shift of the active material's relative permittivity [$\Delta\epsilon_r(\omega)$, with ω being the angular frequency] and consequently to a shift in the real and imaginary parts of the propagation modal index. With this method, either a phase or an absorption modulator can be designed [15].

Although a phase delay alone does not affect the intensity of a light beam, placing a phase modulator in one branch of an interferometer can function as an intensity modulator called Mach-Zehnder interferometer (MZI). The main idea is to change the refractive index of one of the routes of the light beam in order to adjust the optical path difference and

thus have destructive interference with the light beam coming through the other branch (Figure 1.5) [28].

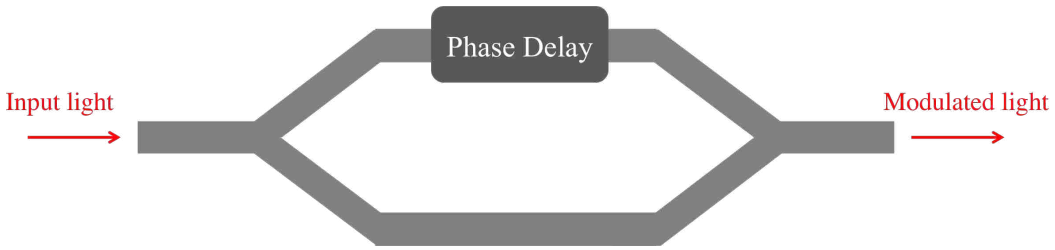

Figure 1.5: Schematic of an integrated optical Mach-Zehnder interferometer.

Although usually very good modulation depth is achievable by interference, the fact that the phase change is normally a cumulative effect and requires a remarkable propagation length, causes an intrinsic limit for the scalability of the manufacturing processes used for Mach-Zehnder modulators. Taking advantage of surface plasmon polaritons (SPPs), the high confinement of the light, and consequently the enhanced interaction of the light beam with the active materials, this problem could be partially solved. Inspired by this solution numerous groups have used and investigated interferometric modulators based on SPPs [29, 30, 31, 32]. Figure 1.6 shows one of the interesting and pioneering layouts of nanoplasmonic MZI modulator [32]. In this work a plasmonic slot waveguide based MZI modulator is proposed by S. Zhu and co-authors. Their structure consists of a 3 μm metal-SiO_2-Si-metal phase shifter followed by a 0.35 μm long combiner. The metal is assumed to be silver and the width of the SiO_2 layer is 2 nm while the Si layer is 50 nm thick. 7.3 dB modulation was achieved at the wavelength of $\lambda = 1.55$ μm with only 3 dB of insertion losses.

In general, electro-absorption modulators in contrast to Mach-Zehnder interferometers, are based on amplitude change of the propagating wave rather than phase change. This change is a result of optically or electrically manipulating the refractive index of a core material. There are two different strategies, either changing the real part or the imaginary

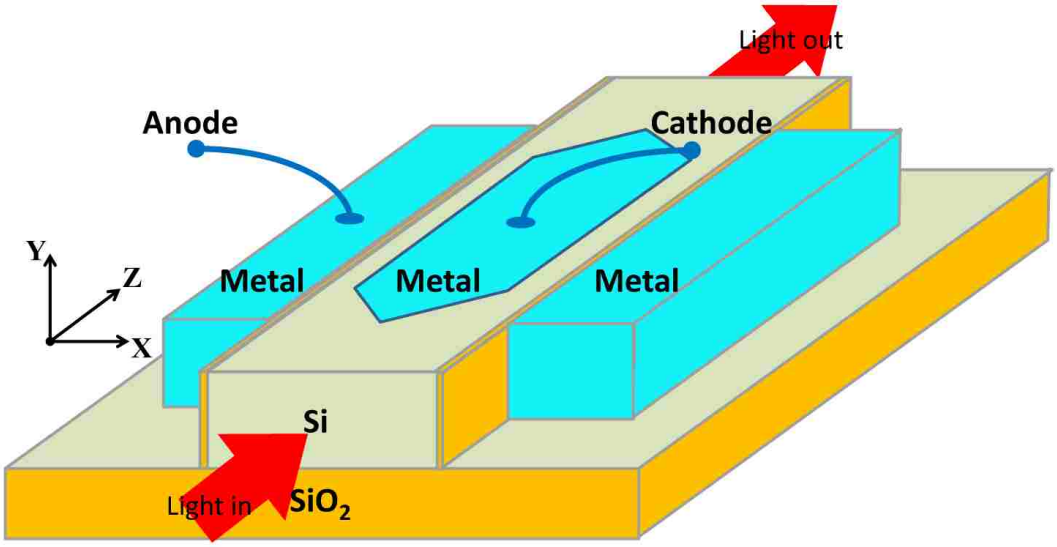

Figure 1.6: Three-dimensional (3-D) schematic of a Si nanoplasmonic MZI modulator, which is composed of a splitter to deliver light from the input Si dielectric waveguide into two plasmonic waveguides. These are horizontal metal-SiO_2-Si-metal MOS-type plasmonic slot waveguides whose optical properties can be modified by the applied voltage. The device also includes a combiner to combine light from the two plasmonic waveguides to the output Si waveguide [32].

part of the dielectric permittivity. Using the former approach, if an appropriate variation of the real part occurs, it will be followed by a fast change in the allowed propagating modes and an efficient modulation is achieved. The second strategy takes advantage of the change of the absorption of the active material leading to modification of the propagation losses [2].

Several different approaches have been proposed in order to achieve efficient modulators. Some of the commonly used methods are incorporation of electro-optic [33, 34], nonlinear [35, 36] or gain [37] media in plasmonic devices, making thermally-induced changes in the refractive index [38, 39, 29], or direct ultrafast optical excitation of the metal [40].

As an example, one of the most remarkable electro-absorption modulators is the one proposed by J. Dionne and co-workers which was based on a metal-oxide-Si planar structure [26]. As shown in Figure 1.7, the device, which is named plasmostor by the authors, utilized a metal-dielectric-metal (MDM) waveguide geometry forming a capacitor. Here, the main idea is to manipulate the refractive index of the Si layer sandwiched between the two

metal layers, forming an electrical capacitor. The applied gate voltage can induce free carrier concentration change leading to carrier accumulation and shift of silicon's optical dispersion. By optimizing the source-drain separation distance d, the device can no longer propagate power from the source to the drain at accumulation.

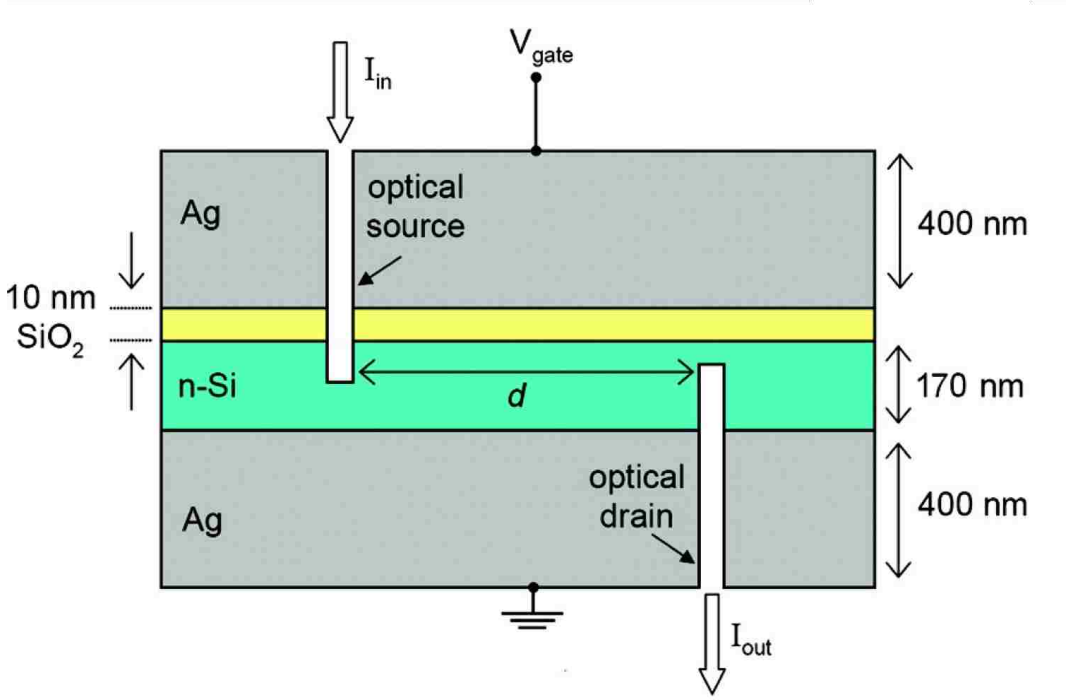

Figure 1.7: Cross-sectional schematic of the Si field effect plasmonic modulator (plasmostor). A 170 nm thick Si film is coated with a thin, 10 nm SiO_2 layer and clad with Ag. Subwavelength slits milled through the Ag cladding form the optical source and drain, through which light is coupled into and out of the modulator [26].

The propagating mode is localized within the 10 nm oxide layer acting as a channel between the optical source and optical drain. This results in high confinement of the field and leads to efficient modulation depth of 10 dB for only 1 volt applied voltage to the bias at telecommunication wavelengths (1.3 to 1.55 μm). While the insertion loss of the fabricated structure was relatively high (-20 dB in the ON state $V_{\text{gate}} = 0$), it can be reduced by optimizing the design parameters. Using the proposed modulator combined with a photodiode connected to the plasmostor gate, Dionne and co-workers have suggested an all-optical modulator (Figure 1.8) [26]. Assuming that the photodiode could provide

the required power, it could modulate the channel properties. This would be a promising first step towards an all-optical nanoplasmonic modulator.

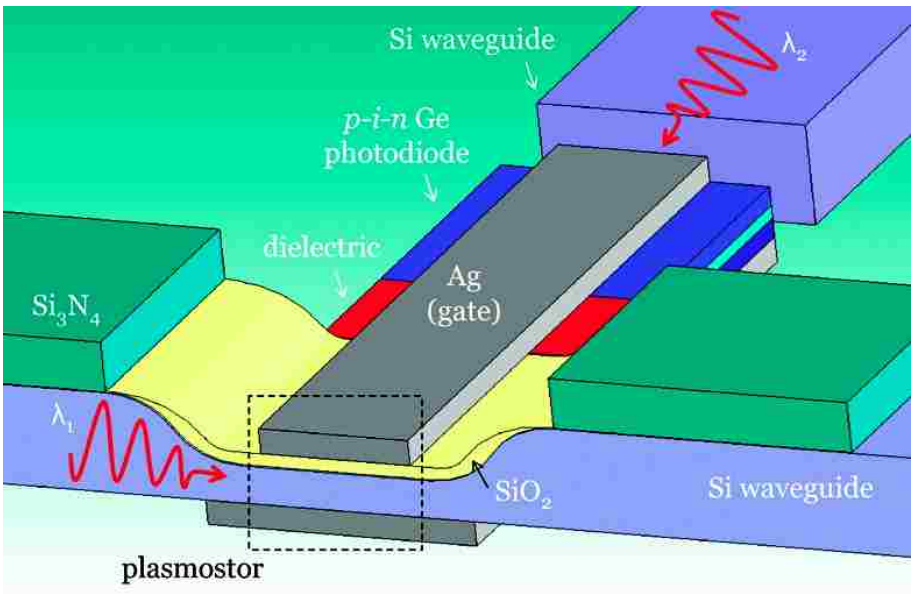

Figure 1.8: An all-optical, SOI-based plasmostor. An ideal photo-diode is connected to a load resistor and the plasmostor, forming a three-terminal device capable of gigahertz operation [26].

1.2 Outline of the Dissertation

The remainder of this dissertation is organized as follows. In Chapter 2, an absorption switch consisting of a MDM plasmonic waveguide coupled to a conventional Fabry-Perot cavity is investigated. Although this compact optical switch structure takes advantage of the subwavelength modal size of MDM waveguides to enhance the interaction between light and the active material inside the cavity, the modulation depth of such a switch when optimized is relatively low. We then introduce a compact absorption switch consisting of a multisection cavity and compare its performance with the performance of the Fabry-Perot cavity switch.

Chapter 3 is dedicated to the space mapping algorithm, originally developed for microwave circuit optimization. We show that it can enable the efficient design of nanoplas-

monic devices which satisfy a set of desired specifications. In this chapter we describe the space mapping algorithm used in this work for the design of nanoplasmonic waveguide devices, and then we present several examples of the application of the algorithm for the design of such devices.

In Chapter 4, we introduce an analytical adjoint sensitivity method for the power transmission coefficient of nano optical devices which is directly derived from Maxwell's equations and is not based on any specific numerical discretization method. We then apply the derived formula to calculate the sensitivity of the power transmission coefficient with respect to the real and imaginary parts of the dielectric permittivity of the active material for two-dimensional and three-dimensional plasmonic devices and compare the results with the ones obtained by directly calculating the sensitivity. Finally, in Chapter 5 we summarize our conclusions and give some recommendations for future work.

Chapter 2
Compact Multisection Cavity Switches in Metal-Dielectric-Metal Plasmonic Waveguides

2.1 Introduction

Plasmonic waveguide devices could be potentially important in providing an interface between conventional diffraction limited optics and nanoscale electronic and optoelectronic devices [41]. One of the main challenges in plasmonics is achieving active control of optical signals in nanoscale plasmonic devices [42]. Active plasmonic devices such as switches and modulators will be critically important for on-chip applications of plasmonics [43].

One of the main concerns when designing nanoplasmonic devices is the insertion loss which is an inevitable characteristic of them because of the material loss in the metal. On the other hand in plasmonic devices such as switches and sensors which incorporate active materials, it is needed to enhance the interaction between light and matter in order to increase the modulation depth. A variety of methods to achieve this goal exist, including field enhancement in the active region or increasing the size of the active region. Usually these approaches also lead to increasing the loss of the device. In plasmonic switches and modulators this leads to a trade off between modulation depth and insertion loss of the device.

Here, we first investigate an absorption switch consisting of a MDM plasmonic waveguide coupled to a conventional Fabry-Perot cavity. The modulation depth of such a switch when optimized is relatively low. We then introduce a compact absorption switch consisting of a multisection cavity. The optimized multisection cavity switch leads to greatly enhanced modulation depth compared to the optimized Fabry-Perot cavity switch.

2.2 Results

We use the finite-difference frequency-domain (FDFD) method to investigate the properties of the absorption switches. This method allows us to directly use experimental data for the frequency-dependent dielectric constant of metals such as silver [44], including both the real and imaginary parts, with no approximation. Perfectly matched layer (PML) absorbing boundary conditions are used at all boundaries of the simulation domain [45]. In all cases considered, the widths of the MDM plasmonic waveguides are much smaller than the wavelength, so that only the fundamental TM waveguide mode is propagating.

We first consider a conventional Fabry-Perot cavity switch consisting of a MDM plasmonic waveguide coupled to a rectangular cavity resonator formed by two MDM stubs (Figure 2.1). The waveguide and resonator are filled with an active material with refractive index $n = 2.02 + i\kappa$, whose absorption coefficient is tunable [42, 46, 47]. The *on* state of the switch corresponds to $\kappa = 0$. When κ is changed to $\kappa = 0.05$ in the cavity region, the switch is turned *off*.

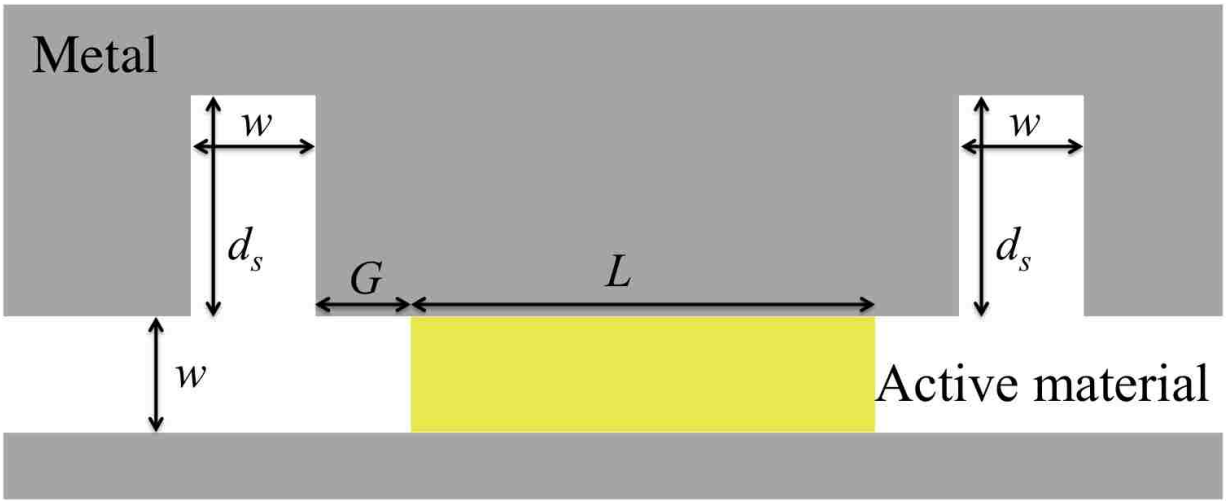

Figure 2.1: Schematic of a conventional Fabry-Perot cavity switch consisting of a MDM plasmonic waveguide coupled to a rectangular cavity resonator formed by two MDM stubs. The waveguide and resonator are filled with an active material with refractive index $n = 2.02 + i\kappa$, where κ is tunable. The *on* state of the switch corresponds to $\kappa = 0$. When κ is changed to $\kappa = 0.05$ in the shaded $L \times w$ cavity region, the switch is turned *off*.

In all cases we consider highly compact subwavelength structures with the length and width of the active region limited to less than 250 nm. The cavity length L as well as the stub length d_s are optimized using a genetic global optimization algorithm in combination with FDFD [48] to maximize the modulation depth of the switch (defined as the difference between the transmission in the *on* and *off* states normalized to the transmission in the *on* state):

$$MD = \frac{T(\kappa = 0) - T(\kappa = 0.05)}{T(\kappa = 0)}, \tag{2.1}$$

at $\lambda_0 = 1.55$ μm, subject to the constraint that the transmission in the *on* state is at least 0.5 (i.e., the insertion loss defined as $-10 \log_{10} [T(\kappa = 0)]$ is less than 3dB). The optimized parameters are $L = 188$ nm and $d_s = 94$ nm resulting in modulation depth of 0.24 and transmission of 0.51. The transmission spectra $T(\kappa = 0)$ for the optimized switch obtained using this approach are shown in Figure 2.2. The optimized conventional Fabry-Perot cavity switch exhibits a resonance at the $\lambda_0 = 1.55$ μm wavelength at which it was optimized. The on resonance transmission is 0.51, exceeding the 0.5 threshold. However, the modulation depth of the optimized switch at $\lambda_0 = 1.55$ μm is 0.24, which is relatively low. The transmission and modulation depth for the switch if the metal is lossless are also obtained and shown in Figures 2.2 and 2.3, respectively (blue dashed lines). In the absence of loss in the metal, the resonance happens at the same wavelength but the complete on resonance transmission demonstrates that the structure is perfectly matched and that there is no loss associated with reflection [49].

We next consider a multisection cavity switch in which the resonator cavity comprises of multiple sections of varying widths (Figure 2.4). The structure is symmetric with respect to a vertical mirror plane which bisects the middle section of the cavity, and, as in the previous case, the total length and width of the active region are limited to less than 250 nm. As in the conventional Fabry-Perot cavity switch case, the cavity sections widths d_1,

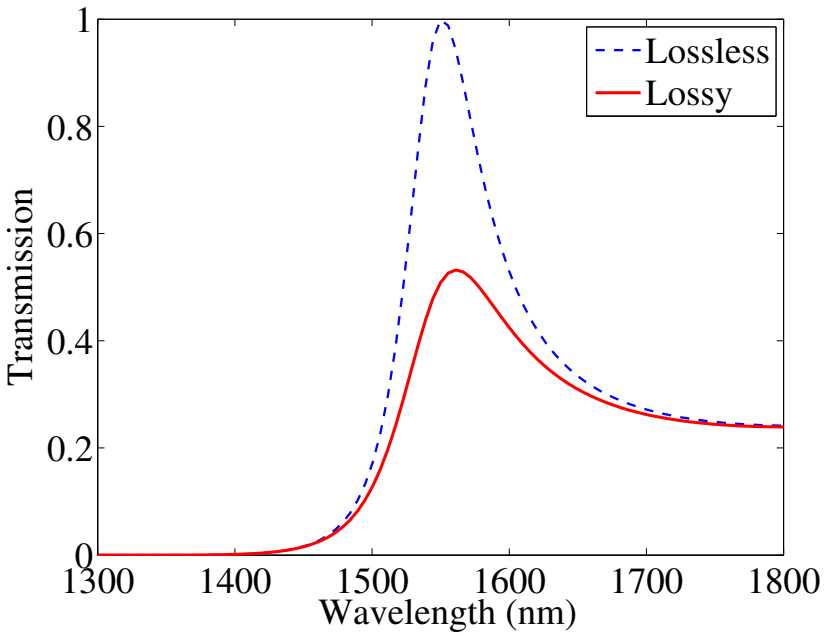

Figure 2.2: Transmission spectra $T(\kappa = 0)$ for the optimized Fabry-Perot cavity switch of Figure 2.1 in the *on* state (solid line). Also shown are the transmission spectra if the metal is lossless (dashed line). Results are shown for $w = 50$ nm, $d_s = 94$ nm, $G = 50$ nm, $L = 188$ nm. The metal is silver.

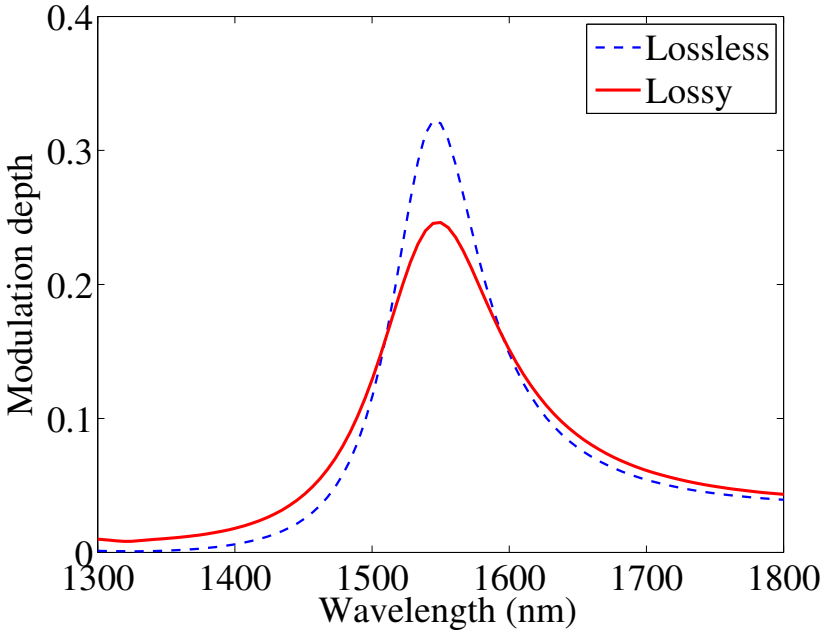

Figure 2.3: Modulation depth as a function of wavelength for the optimized switch of Figure 2.1 (solid line). Also shown is the modulation depth if the metal is lossless (dashed line).

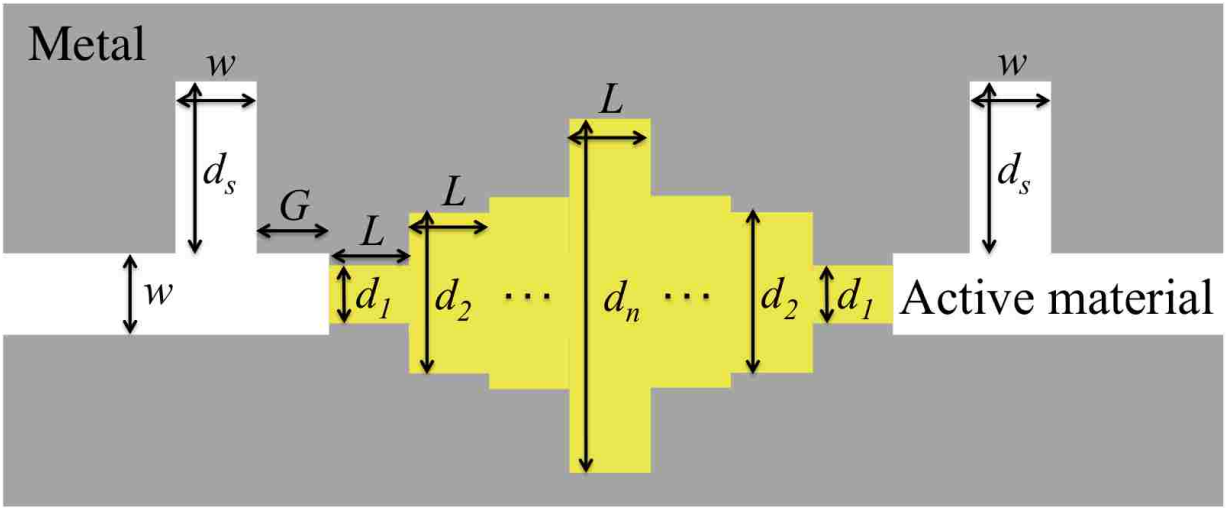

Figure 2.4: Schematic of a multisection cavity switch consisting of a MDM plasmonic waveguide coupled to a resonator. The resonator is formed by a cavity comprising of multiple sections of varying widths sandwiched between two MDM stubs.

..., d_n as well as the stub length d_s are optimized to maximize the modulation depth of the switch, subject to the constraint that the transmission in the *on* state is at least 0.5.

The optimized parameters for a multisection cavity (Figure 2.4) with 5 sections (n=3) are $d_1 = 250$ nm, $d_2 = 250$ nm, $d_3 = 150$ nm, $d_s = 172$ nm. The length of each section L is 50 nm, so that the total length of the active region is 250 nm. The optimized structure has a relatively simple shape and can be considered as a perturbation of the maximum size cavity by reducing the width of the middle section (Figure 2.5).

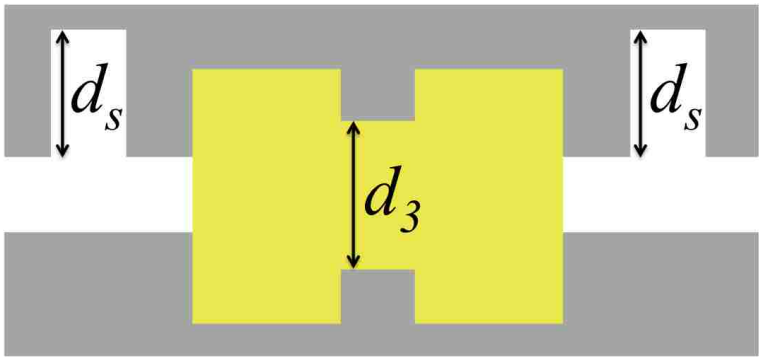

Figure 2.5: Schematic of the optimized multisection cavity switch.

As in the previous case, the optimized multisection cavity switch exhibits a resonance at the 1.55 μm wavelength at which it was optimized, and the on resonance transmission of 0.51, exceeds the 0.5 threshold (Figure 2.6). In addition, the on resonance modulation depth of the optimized multisection cavity switch is 0.69 (Figure 2.7), and is greatly enhanced with respect to the conventional Fabry-Perot cavity switch (Figure 2.3).

The modulation depth of the switches is associated with the sensitivity of their transmission to the imaginary part of the dielectric constant of the active material, which is in turn directly related to the electric field energy in the cavity region [50, 51, 52, 53]. We found that the modulation depth of the optimized multisection cavity switch (Figure 2.4) is greatly enhanced compared to the optimized Fabry-Perot cavity switch (Figure 2.1) due to the great enhancement of the total electric field energy in the cavity region. The profile of electric field amplitude for the optimized switch is given in Figure 2.8. The concentration of electric field is around the tips of the middle section of the cavity filled with active material. The enhanced field energy in the cavity increases the interaction of light with matter, and the absorption in the *off* state is therefore enhanced.

Again the transmission and modulation depth for the switch if the metal is lossless are also obtained and shown in Figures 2.6 and 2.7, respectively (blue dashed lines). It can be seen that in the absence of loss in the metal perfect matching leads to complete transmission at the 1.55 μm wavelength at which the structure was optimized.

The two stubs before and after the cavity can be considered as the mirrors for the structure to enhance the interaction of light and matter. As it can be seen in Figure 2.9 there is a trade off between transmission and modulation depth when the stub length d_s is varying. The optimized length of the stubs obtained by the optimization algorithm is $d_s = 172$ nm. As can be seen in Figure 2.9, the choice of this parameter is dictated by the

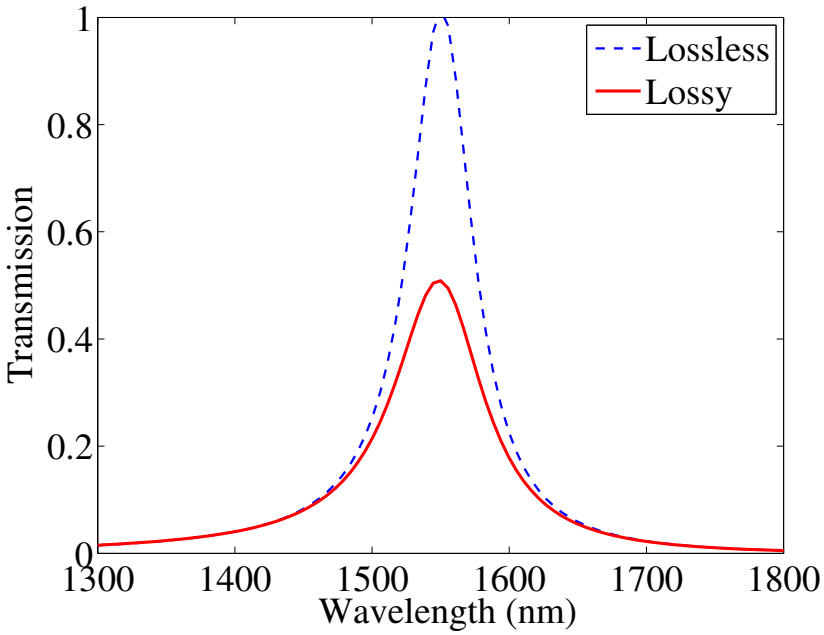

Figure 2.6: Transmission spectra $T(\kappa = 0)$ for the optimized multisection cavity switch of Figure 2.4 in the *on* state (solid line). Also shown are the transmission spectra if the metal is lossless (dashed line). Results are shown for $w = 50$ nm, $d_s = 172$ nm, $G = 50$ nm, $d_1 = 250$ nm, $d_2 = 250$ nm, $d_3 = 150$ nm, $L = 50$ nm.

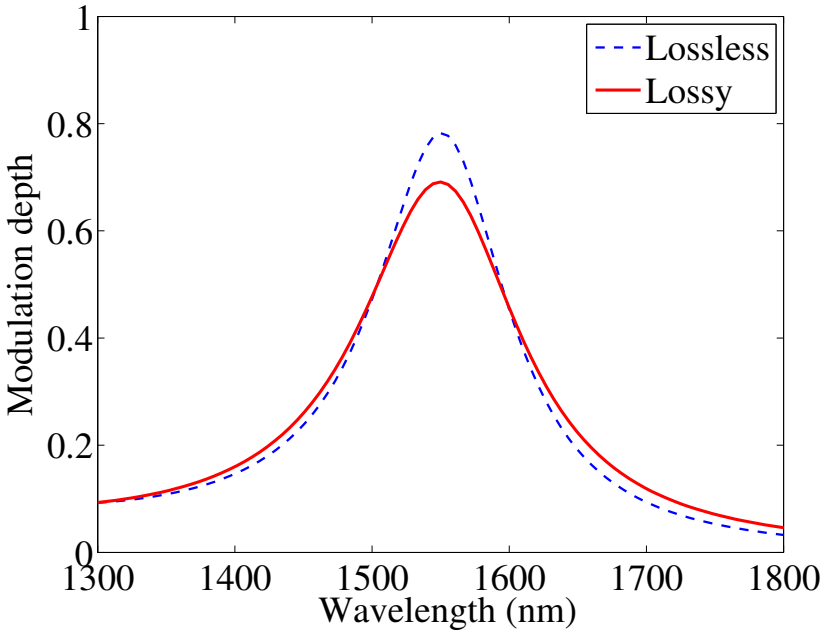

Figure 2.7: Modulation depth as a function of wavelength for the optimized switch of Figure 2.4 (solid line). Also shown is the modulation depth if the metal is lossless (dashed line). All other parameters are as in Figure 2.6.

constraint that the transmission in the *on* state must be at least 0.5. Further increasing d_s improves the modulation depth but also reduces the transmission (Figure 2.9).

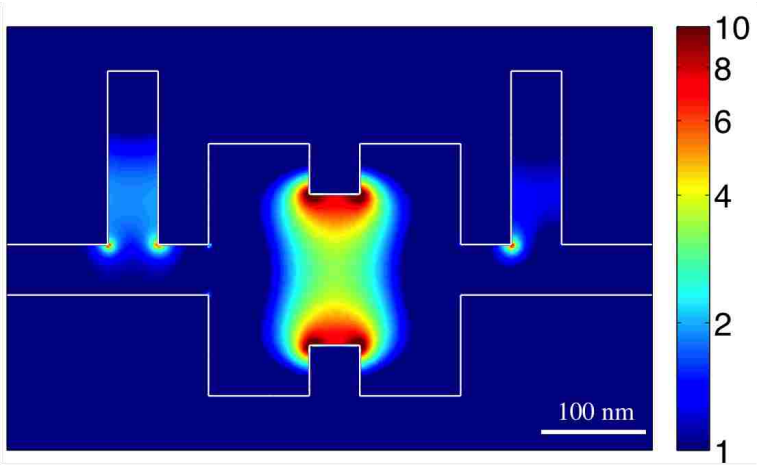

Figure 2.8: Profile of the electric field amplitude for the optimized switch of Figure 2.4 at $\lambda_0 = 1.55$ μm, normalized with respect to the maximum field amplitude of the incident MDM waveguide mode.

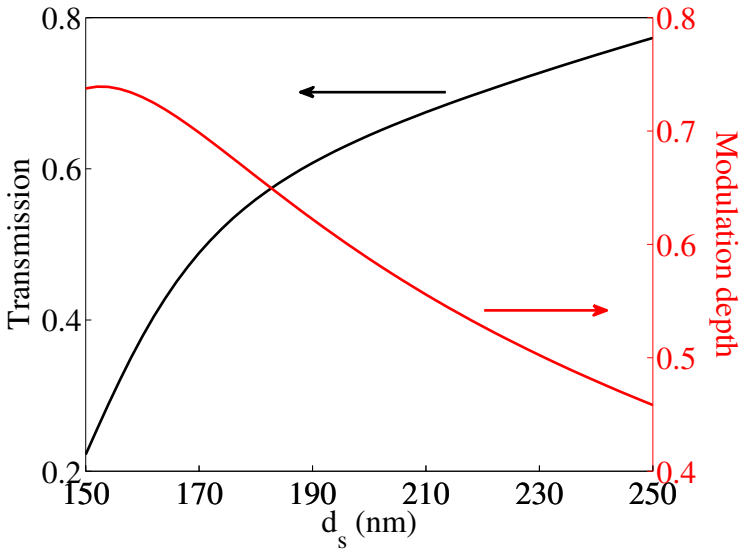

Figure 2.9: Transmission (black curve) and modulation depth (red curve) of the optimized multisection cavity switch (Figure 2.5) as a function of the length of the MDM stubs d_s. All other parameters are as in Figure 2.6.

In addition, the width of the middle section d_3 is a tuning parameter of the resonator. More specifically, by changing d_3 one can tune the resonant wavelength of the cavity (Figure 2.10). Figures 2.11 and 2.12 show that the maximum transmission and maximum modulation depth of the switch are both achieved when the width of the middle section is $d_3 = 150$ nm. This is due to the fact that when $d_3 = 150$ nm, the resonant wavelength of the cavity coincides with the operating wavelength (Figure 2.9). When the structure is on resonance, the sensitivity of the transmission to the imaginary part of the dielectric constant of the active material ϵ_{r_i}, $T^{-1}\frac{\partial T}{\partial \epsilon_{r_i}}$ and therefore the modulation depth are maximized (Figure 2.13).

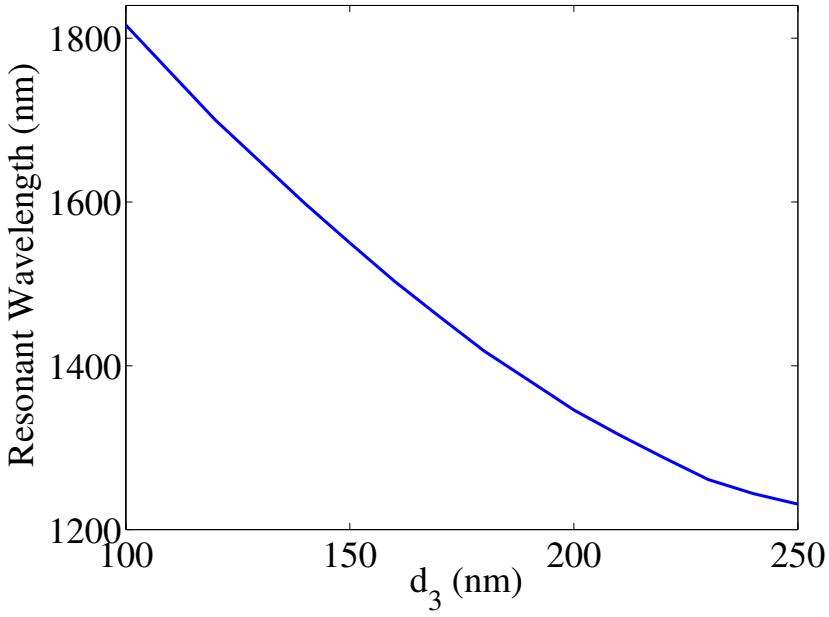

Figure 2.10: Resonant wavelength of the multisection cavity as a function of the width of the middle section d_3. All other parameters are as in the optimized structure of Figure 2.6.

Based on transmission line theory, the multisection cavity switch is equivalent to multiple transmission line sections sandwiched between two short-circuited transmission line resonators of length d_s [41, 54, 55]. The transmission of the multisection cavity absorption

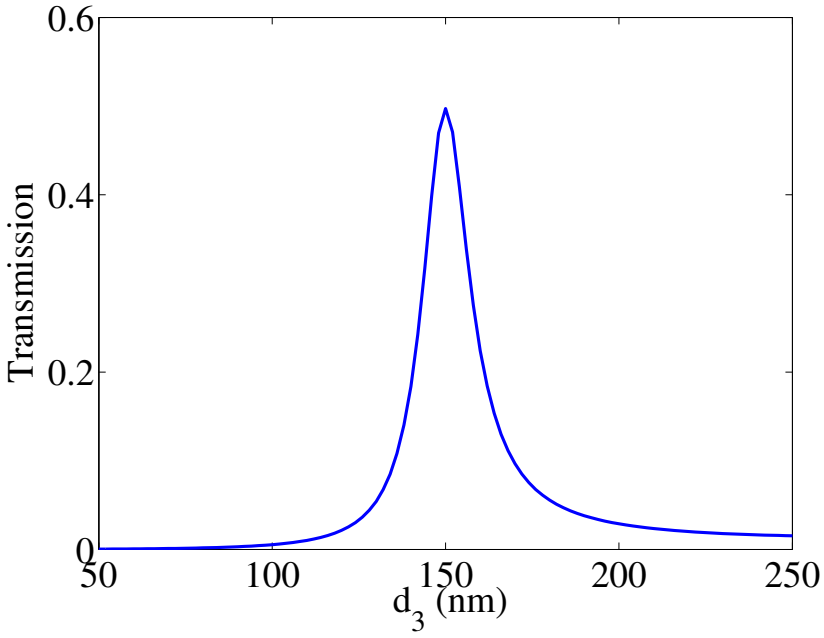

Figure 2.11: Transmission of the multisection cavity switch as a function of the width of the middle section d_3. All other parameters are as in Figure 2.6.

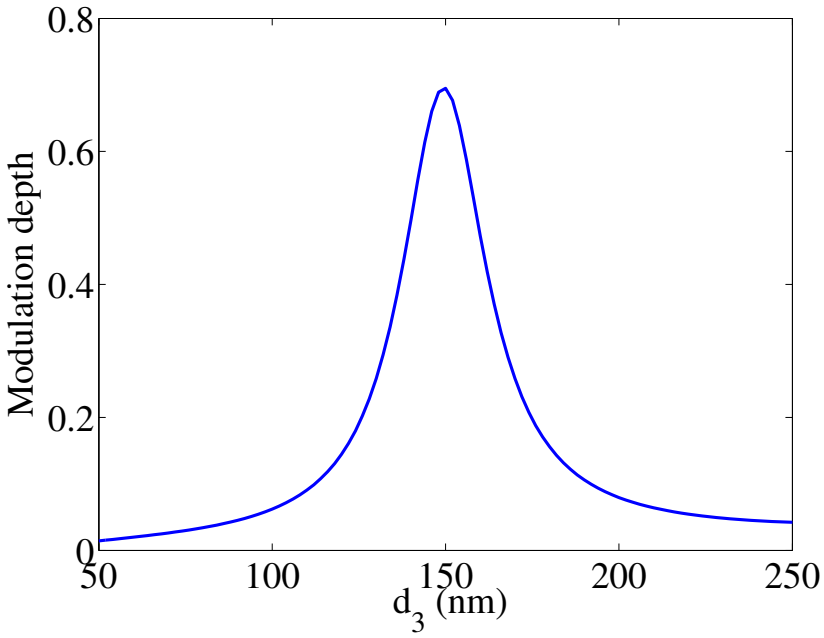

Figure 2.12: Modulation depth of the multisection cavity switch as a function of the width of the middle section d_3. All other parameters are as in Figure 2.6.

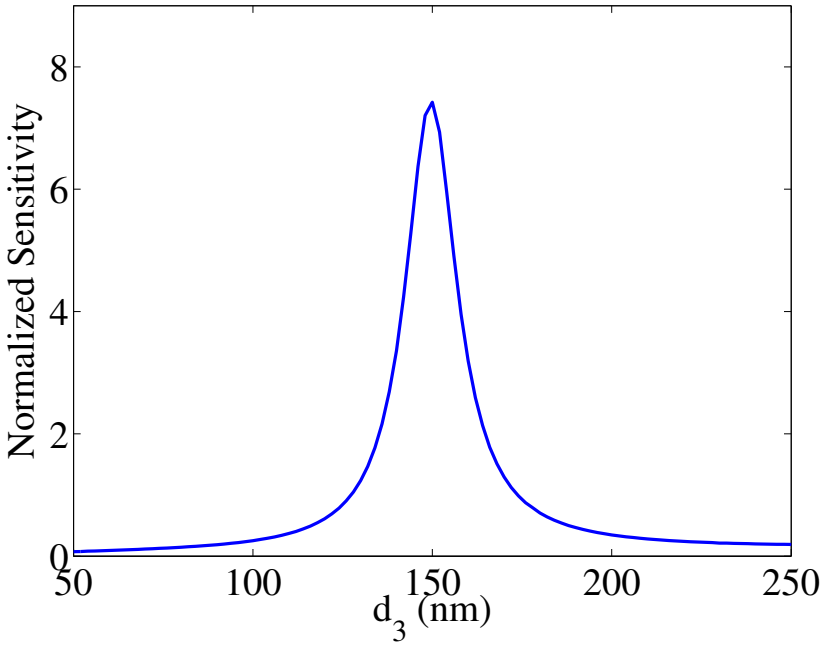

Figure 2.13: Normalized sensitivity of the transmission of the multisection cavity switch to the imaginary part of the dielectric constant of the active material ϵ_{r_i}, $T^{-1}\frac{\partial T}{\partial \epsilon_{r_i}}$, as a function of the width of the middle section d_3.

switch can also be investigated by using a transfer matrix model. The structure of Figure 2.4 can be considered as a combination of five cascade sections: the left stub, the left gap, the cavity, the right gap and the right stub. The complex magnetic field reflection and transmission coefficients for the stubs (r_s and t_s) and cavity (r_c and t_c) can be extracted from the fields obtained by FDFD (Figures 2.14 and 2.15). Because of the symmetry of the structure these coefficients are the same for the left and right stubs. The power transmission of the switch can then be calculated as (Appendix A):

$$T = \left| \frac{t_s^2 t_c e^{-2\gamma G}}{1 - 2r_s r_c e^{-2\gamma G} + (r_s^2 r_c^2 - r_s^2 t_c^2) e^{-4\gamma G}} \right|^2, \tag{2.2}$$

where γ is the propagation constant for the MDM waveguide with the width of $w = 50$ nm and G is the length of the gap between the stubs and the cavity. The transmission

calculated using the transfer matrix model is in excellent agreement with the one obtained by FDFD (Figure 2.16).

Comparing Eq. 2.2 with the transmission for a conventional Fabry-Perot cavity, it is obvious that the former is more complicated. In the absence of the cavity, the switch can be considered as a conventional Fabry-Perot structure with the distance between the

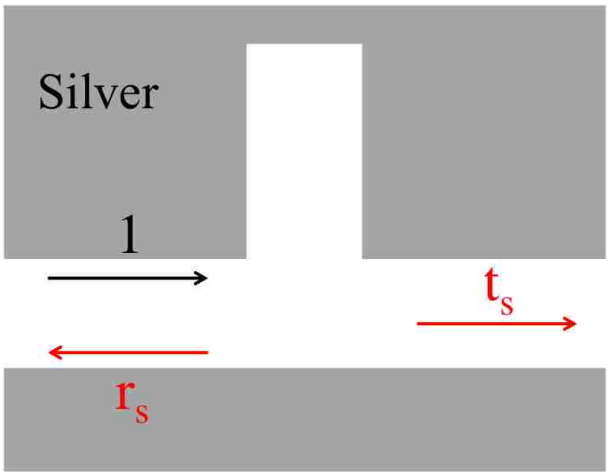

Figure 2.14: Schematic defining the reflection coefficient r_s, and transmission coefficient t_s when the fundamental TM mode of the MDM waveguide is incident at a single stub of the proposed absorption switch.

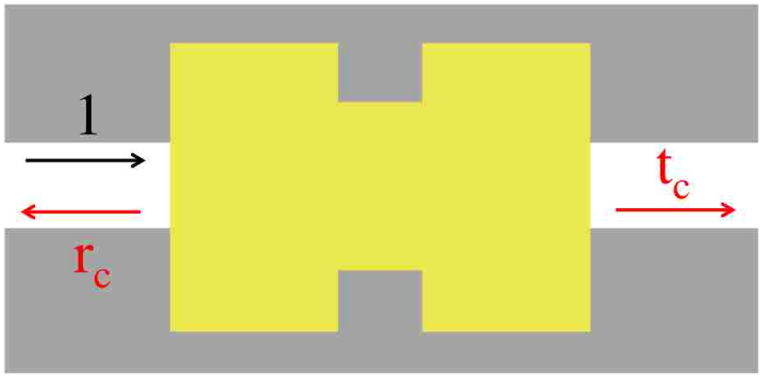

Figure 2.15: Schematic defining the reflection coefficient r_c, and transmission coefficient t_c when the fundamental TM mode of the MDM waveguide is incident at a cavity of the proposed absorption switch.

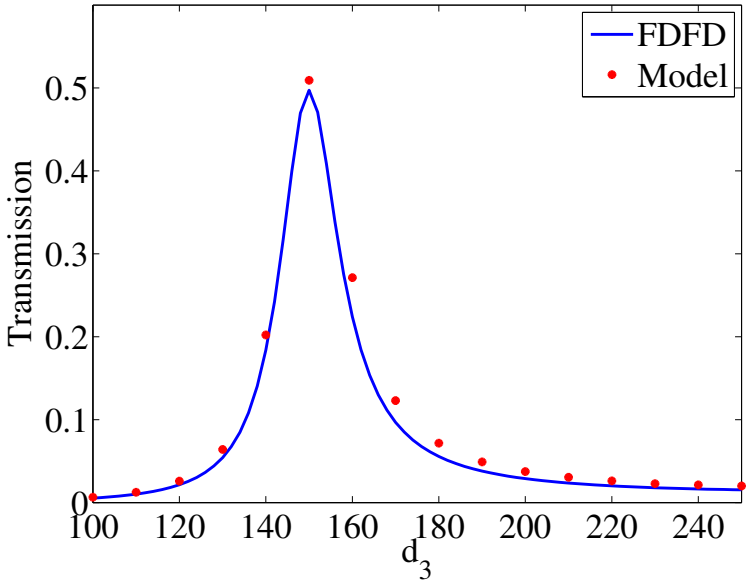

Figure 2.16: Transmission as a function of the width of the middle section d_3 for the structure of Figure 2.4, calculated using FDFD (red solid line) and scattering matrix theory (blue dots) at $\lambda_0 = 1550$ nm.

mirrors of $l = 2G$. Assuming $t_c = 1$, $r_c = 0$ and substituting these parameters in Eq. 2.2 the well-known transmission equation for Fabry-Perot structures is obtained [56]:

$$T = \left| \frac{t_s^2 e^{-\gamma l}}{1 - r_s^2 e^{-2\gamma l}} \right|^2 . \tag{2.3}$$

Chapter 3
Efficient Design of Nanoplasmonic Waveguide Devices Using the Space Mapping Algorithm

3.1 Introduction

The unique properties of surface plasmons could enable a wide range of applications for plasmonics, including light guiding and manipulation at the nanoscale [9, 57, 11, 58, 12, 4]. The realization of active and passive nanoplasmonic devices with optimal performance for high-density optical information processing could have profound implications for computing and communications. In designing such nanoplasmonic devices, ideally one would like to solve inverse problems starting from design specifications imposed on the device response. This can be achieved by combining global optimization algorithms with electromagnetic simulations [48, 59, 60]. Such an approach leads to an extremely powerful design technique which can enable high performance nanoplasmonic devices. In many cases, the highly efficient device designs coming out of this approach cannot be obtained with any conventional design method based on analytical techniques [61]. However, integrated nanoplasmonic devices consist of multiple components and therefore have several design parameters [62, 63]. Thus, the solution of inverse problems by combining global optimization algorithms with electromagnetic simulations often requires simulation of hundreds to thousands of candidate structures before a design which satisfies all the specifications is reached. In most cases, full-wave electromagnetic simulation methods are too computationally expensive for this purpose. Thus, alternative approaches to solve inverse design problems for nanoplasmonic devices need to be explored.

Here, we show that the space mapping algorithm, originally developed for microwave circuit optimization, can enable the efficient design of nanoplasmonic devices which satisfy

a set of desired specifications. Space mapping utilizes a physics-based coarse model to approximate a fine model accurately describing a device. The main concept in the algorithm is to find a mapping that relates the fine and coarse model design parameters. If such a mapping is established, we can then avoid directly optimizing the computationally expensive fine model during the design process. Instead, we perform optimization of the computationally efficient coarse model, and then use the mapping to find the corresponding fine model design.

More specifically, we demonstrate the use of the space mapping algorithm for the design of metal-dielectric-metal (MDM) plasmonic waveguide devices [55]. Such devices could be potentially important in providing an interface between conventional optics and subwavelength electronic and optoelectronic devices [41, 54]. In our case, the fine model is a full-wave finite-difference frequency-domain (FDFD) simulation of the device, while the coarse model is based on transmission line theory. Through several examples, we demonstrate that simply optimizing the transmission line model of the device is not enough to obtain a device which satisfies all the required design specifications. On the other hand, we show that, when the iterative space mapping algorithm is used, it converges fast to a design which meets all the specifications. In addition, full-wave FDFD simulations of only a few candidate structures are required before the iterative process is terminated. Use of the space mapping algorithm therefore results in large reductions in the required computation time when compared to any direct optimization method of the fine FDFD model.

The remainder of this chapter is organized as follows. In Section 3.2, we describe the space mapping algorithm used in this work for the design of nanoplasmonic waveguide devices. In Section 3.3, we present several examples of the application of the algorithm for the design of such devices.

3.2 Algorithm

Space mapping utilizes a physics-based coarse model to approximate a fine model which accurately describes a device [64, 65, 66]. The coarse and fine model design parameters are

denoted by $\mathbf{x}_c$ and $\mathbf{x}_f$, respectively, while the corresponding responses are denoted by R_c and R_f. In this work it is assumed that $\mathbf{x}_c$ and $\mathbf{x}_f$ have the same dimensionality. In other words, the number of design parameters n is the same for both models. The main concept in the space mapping algorithm is to find a mapping $\mathbf{P}$ that relates the fine and coarse model parameters through

$$\mathbf{x}_c = \mathbf{P}(\mathbf{x}_f), \tag{3.1}$$

such that

$$R_c(\mathbf{P}(\mathbf{x}_f)) \simeq R_f(\mathbf{x}_f). \tag{3.2}$$

We assume that such a one-to-one mapping exists in the region of interest. If such a mapping is established, we can then avoid using the direct optimization of the computationally expensive fine model to find the solution $\mathbf{x}_f^*$. Instead, we perform optimization of the computationally efficient coarse model to find its optimal solution $\mathbf{x}_c^*$, and then use

$$\bar{\mathbf{x}}_f \equiv \mathbf{P}^{-1}(\mathbf{x}_c^*) \tag{3.3}$$

to find an estimate of the fine model solution $\mathbf{x}_f^*$.

3.2.1 Aggressive space mapping

More specifically, here we use the aggressive space mapping implementation of the algorithm [64], which incorporates a quasi-Newton iteration. In this approach we assume that $\mathbf{x}_c$ is a nonlinear vector function $\mathbf{P}$ of $\mathbf{x}_f$ (Eq. 3.1).

In the first step, we perform optimization of the computationally efficient coarse model and find its optimal solution $\mathbf{x}_c^*$. Eq. 3.3 can be rewritten as

$$\mathbf{P}(\bar{\mathbf{x}}_f) - \mathbf{x}_c^* = 0. \tag{3.4}$$

Thus, the solution of the space mapping algorithm $\bar{\mathbf{x}}_f$ can be found by solving the system of nonlinear equations

$$\mathbf{g}(\mathbf{x}_f) = 0, \tag{3.5}$$

where

$$\mathbf{g}(\mathbf{x}_f) \equiv \mathbf{P}(\mathbf{x}_f) - \mathbf{x}_c^*. \tag{3.6}$$

We can therefore use a quasi-Newton iterative method to solve this problem. Since the Jacobian matrix corresponding to Eq. 3.5

$$\mathbf{J}(\mathbf{x}_f) = \left[\frac{\partial^T \mathbf{g}(\mathbf{x}_f)}{\partial \mathbf{x}_f}\right]^T \tag{3.7}$$

cannot be directly calculated, we use an approximation for the Jacobian matrix based on the Broyden formula [64, 67].

The initial point for the algorithm is the optimal solution of the coarse model $\mathbf{x}_c^*$

$$\mathbf{x}_f^{(1)} = \mathbf{x}_c^*. \tag{3.8}$$

If $\mathbf{x}_f^{(j)}$ is the jth approximation to the solution of Eq. 3.5 then $\mathbf{x}_f^{(j+1)}$ is found by

$$\mathbf{x}_f^{(j+1)} = \mathbf{x}_f^{(j)} + \mathbf{h}^{(j)}, \tag{3.9}$$

where $\mathbf{h}^{(j)}$ is the solution of the following linear system

$$\mathbf{B}^{(j)}\mathbf{h}^{(j)} = -\mathbf{g}^{(j)}. \tag{3.10}$$

In the above equation $\mathbf{g}^{(j)}$ is obtained by

$$\mathbf{g}^{(j)} \equiv \mathbf{g}(\mathbf{x}_f^{(j)}) = \mathbf{P}(\mathbf{x}_f^{(j)}) - \mathbf{x}_c^*, \tag{3.11}$$

where $\mathbf{P}(\mathbf{x}_f^{(j)})$ is calculated using the parameter extraction procedure described below, while $\mathbf{B}^{(j)}$ is obtained by the Broyden formula [67]

$$\mathbf{B}^{(1)} = \mathbf{I}, \tag{3.12}$$

$$\mathbf{B}^{(j)} = \mathbf{B}^{(j-1)} + \frac{\mathbf{g}^{(j)}\mathbf{h}^{(j-1)^T}}{\mathbf{h}^{(j-1)^T}\mathbf{h}^{(j-1)}}. \tag{3.13}$$

The iterative procedure is terminated after M iterations when the fine model response $R_f(\mathbf{x}_f^{(M)})$ satisfies the set of desired specifications.

3.2.2 Parameter extraction

At each iteration of the space mapping algorithm we use a parameter extraction procedure to obtain the mapping $\mathbf{x}_c = \mathbf{P}(\mathbf{x}_f)$ which corresponds to the optimum match between the coarse and fine model responses. More specfically, we use an optimization algorithm in combination with the coarse model of the structure to minimize the objective function $H(\mathbf{x}_c)$

$$\min_{\mathbf{x}_c} H(\mathbf{x}_c), \tag{3.14}$$

where

$$H(\mathbf{x}_c) = \sum_{i=1}^{n} \rho_k(e_i(\mathbf{x}_c)). \tag{3.15}$$

Here, e_i is the error at frequency ω_i, defined as the difference between the responses calculated with the coarse and fine models

$$e_i(\mathbf{x}_c) \equiv R_c(\mathbf{x}_c, \omega_i) - R_f(\mathbf{x}_f, \omega_i), \tag{3.16}$$

and $\rho_k(e_i)$ is the Huber norm [68, 69] given by

$$\rho_k(e_i) \equiv \begin{cases} e_i^2/2 & \text{, if } |e_i| \leq k \\ k|e_i| - k^2/2 & \text{, if } |e_i| > k. \end{cases} \tag{3.17}$$

The Huber norm is robust against large errors e_i [64]. Here we use $k = 0.04$.

3.2.3 Application of the space mapping algorithm to design of nanoplasmonic waveguide devices

Here, we demonstrate the use of the space mapping algorithm for the design of nanoplasmonic waveguide devices. We assume that a set of desired specifications are imposed on the transmission response of the device. We wish to find the design parameters of the device so that its transmission response satisfies all the specifications. In our case, the fine model is a full-wave finite-difference frequency-domain (FDFD) simulation of the device [70, 50]. This method allows us to directly use experimental data for the frequency-dependent dielectric constant of metals such as silver [44], including both the real and imaginary parts, with no approximation. Perfectly matched layer (PML) absorbing boundary conditions are used at all boundaries of the simulation domain [45, 71]. We use a fine spatial grid size in FDFD to ensure the convergence of the numerical results. Thus the fine FDFD model gives essentially the exact solution of the Maxwell's equations for the given device and therefore accurately describes the device. The coarse model is based on transmission line theory and will heretofore be referred to as the transmission line model of the device.

In our case the fine model design parameters are a set of geometric dimensions $\mathbf{L} = [L_1 \quad L_2 \quad \cdots \quad L_n]^T$ of the plasmonic device. The coarse transmission line model parameters have a one-to-one corespondence to the fine model parameters and are denoted as $\mathbf{L}_{\mathrm{TL}} = [L_{\mathrm{TL1}} \quad L_{\mathrm{TL2}} \quad \cdots \quad L_{\mathrm{TLn}}]^T$. The fine and coarse model responses are the transmission of the plasmonic device calculated with FDFD, T_{FDFD}, and the transmission line model, T_{TL}, respectively.

3.3 Results

In this section, we present several examples of the application of the space mapping algorithm for the design of nanoplasmonic waveguide devices.

3.3.1 MDM waveguide side-coupled to two MDM stub resonators

In the first example, the structure considered consists of a plasmonic MDM waveguide side-coupled to two MDM stub resonators (Figure 3.1). The fundamental TM mode of the MDM waveguide is incident from the left. This system is a plasmonic analogue of electromagnetically-induced transparency (EIT) [72].

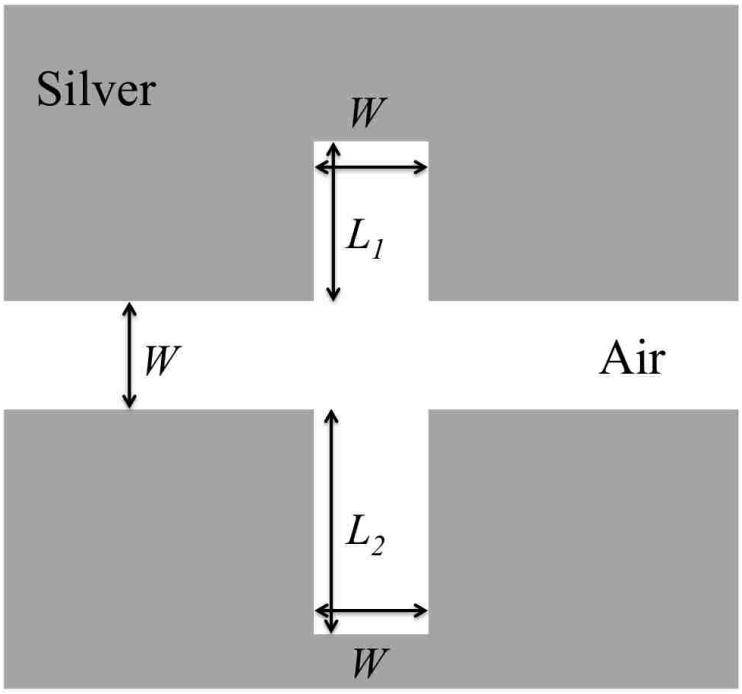

Figure 3.1: Schematic of a MDM plasmonic waveguide side-coupled to two MDM stub resonators.

Using such a waveguide device geometry, we wish to design a structure with a bandpass filter response. More specifically, the design specifications imposed on the transmission response T of the structure are:

$$T > 0.75 \quad \text{for} \quad 180 \text{ THz} < f < 200 \text{ THz}, \tag{3.18a}$$

$$T < 0.2 \quad \text{for} \quad 130 \text{ THz} < f < 160 \text{ THz} \quad \text{and} \quad 240 \text{ THz} < f < 270 \text{ THz}, \tag{3.18b}$$

where f is the frequency. The specifications are indicated in Figures 3.3 and 3.4 with solid red lines. Here the design parameters are the lengths of the stub resonators L_1 and L_2, while the width w of all waveguide sections is fixed at $w = 50$ nm.

Based on transmission line theory, the transmission line model of this structure consists of two short-circuited transmission line resonators of lengths L_{TL1} and L_{TL2}, propagation constant γ, and characteristic impedance Z, which are connected in series to a transmission line with the same propagation constant γ and characteristic impedance Z [73, 42] (Figure 3.2). The characteristic impedance is given by [41, 42]

$$Z = \frac{\gamma}{j\omega\varepsilon} w, \tag{3.19}$$

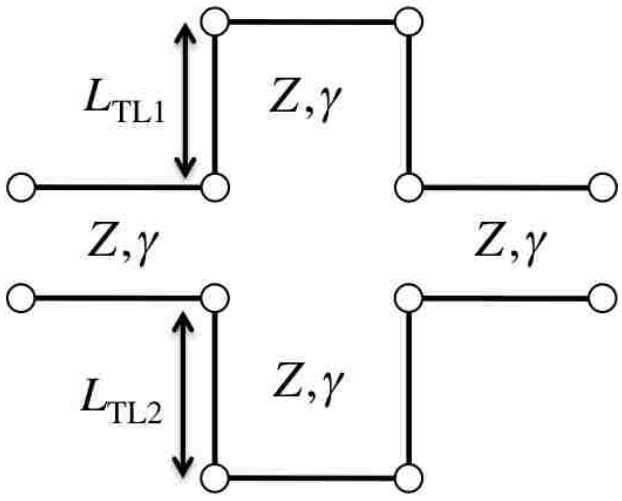

Figure 3.2: Schematic of the transmission line model for the structure of Figure 3.1. Here $Z(\omega)$ and $\gamma(\omega)$ are the characteristic impedance and complex propagation constant of the fundamental TM mode of a silver-air-silver plasmonic waveguide with width w.

where $\omega = 2\pi f$, $j = \sqrt{-1}$, and ϵ is the dielectric permittivity of the dielectric region of the MDM waveguide. Based on transmission line theory, the transmission line model response

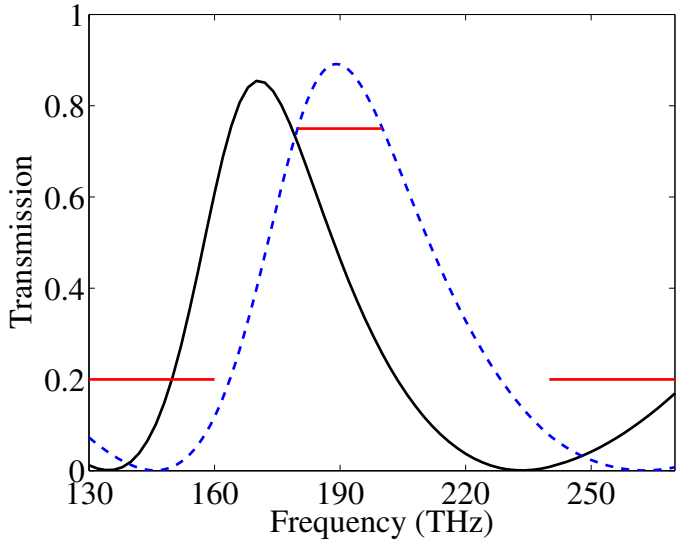

Figure 3.3: Transmission line model response $T_{\mathrm{TL}}(L^*_{\mathrm{TL1}}, L^*_{\mathrm{TL2}})$ of the structure of Figure 3.1 for parameters $L^*_{\mathrm{TL1}} = 210$ nm and $L^*_{\mathrm{TL2}} = 384$ nm obtained by optimizing the transmission line model of Figure 3.2 (dashed blue line). We also show the transmission response calculated using FDFD, $T_{\mathrm{FDFD}}(L_1 = L^*_{\mathrm{TL1}}, L_2 = L^*_{\mathrm{TL2}})$ for the same parameters (solid black line). Results are shown for $w = 50$ nm. The red lines are the design specifications imposed on the transmission response of this structure.

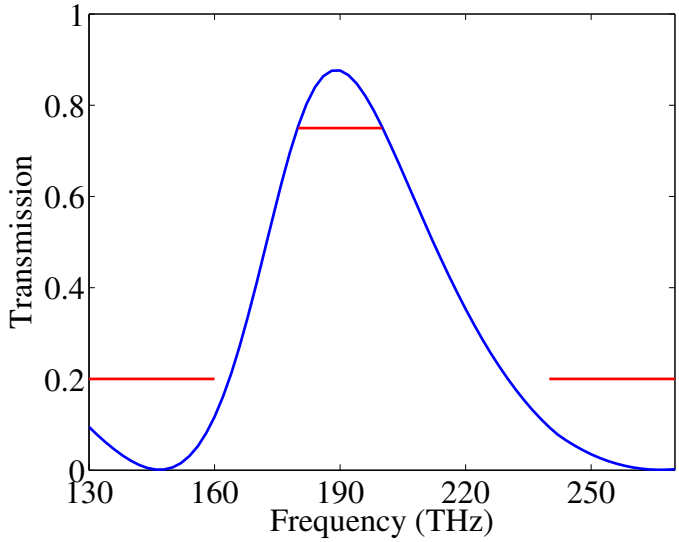

Figure 3.4: Transmission response $T_{\mathrm{FDFD}}(\bar{L}_1, \bar{L}_2)$ of the structure of Figure 3.1 calculated with FDFD for the parameters $\bar{L}_1 = 180$ nm and $\bar{L}_2 = 351$ nm obtained by the space mapping algorithm.

$T_{\mathrm{TL}}(L_{\mathrm{TL1}}, L_{\mathrm{TL2}})$ of the structure of Figure 3.1 can be calculated as (Appendix B) [74, 73]

$$T_{\mathrm{TL}}(L_{\mathrm{TL1}}, L_{\mathrm{TL2}}) = \left| 1 + \frac{1}{2} \left[\tanh(\gamma L_{\mathrm{TL1}}) + \tanh(\gamma L_{\mathrm{TL2}}) \right] \right|^{-2}. \tag{3.20}$$

The transmission line model is computationally efficient with a required computation time which is negligible compared to a full-wave FDFD simulation of the device. However, the accuracy of this model is limited. The accuracy limitations of the transmission line model for circuits of MDM plasmonic waveguides have been described in detail elsewhere [75]. As an example, the transmission line model introduces errors in the phase of the reflection coefficient at the two interfaces of a side-coupled MDM stub resonator [76, 77].

We use the coarse transmission line model of the structure (without space mapping) in combination with a genetic global optimization algorithm [78, 48] to find the stub lengths L_{TL1} and L_{TL2} such that the transmission line model response $T_{\mathrm{TL}}(L_{\mathrm{TL1}}, L_{\mathrm{TL2}})$ satisfies the design specifications. During the optimization process the transmission line model response is calculated at a discrete set of frequencies in the passband (180 THz $< f <$ 200 THz) and stopbands (130 THz $< f <$ 160 THz and 240 THz $< f <$ 270 THz) for each structure. The objective is to maximize the transmission T_{TL} in the passband, and minimize it in the stopbands. The optimal transmission line model stub lengths found using this approach are $L^*_{\mathrm{TL1}} = 210$ nm and $L^*_{\mathrm{TL2}} = 384$ nm. As shown in Figure 3.3, the transmission line model response for the optimized device $T_{\mathrm{TL}}(L^*_{\mathrm{TL1}}, L^*_{\mathrm{TL2}})$ (dashed blue line) meets all the design specifications (Eq. 3.18).

We first investigate whether optimizing the transmission line model of the structure is enough to obtain a device which satisfies all the design specifications. We therefore perform a full-wave FDFD simulation of the device setting the stub lengths L_1, L_2 equal to the optimal transmission line model stub lengths, and obtain the device response $T_{\mathrm{FDFD}}(L_1 = L^*_{\mathrm{TL1}}, L_2 = L^*_{\mathrm{TL2}})$. We observe that the transmission response of the device obtained with this approach $T_{\mathrm{FDFD}}(L_1 = L^*_{\mathrm{TL1}}, L_2 = L^*_{\mathrm{TL2}})$ (black solid line) is substantially different

from the transmission line model response $T_{\mathrm{TL}}(L^*_{\mathrm{TL1}}, L^*_{\mathrm{TL2}})$ (dashed blue line), and does not meet all the desired specifications (Figure 3.3). This is due to the limited accuracy of the transmission line model which was discussed above. Thus, simply optimizing the transmission line model of the device is not enough to obtain a device which satisfies all the required design specifications.

To obtain such a device which will satisfy all the design specifications, we now use the space mapping algorithm, described in Section 3.2. We found that the space mapping algorithm converges fast to the design $\bar{L}_1 = 180$ nm and $\bar{L}_2 = 351$ nm with device response $T_{\mathrm{FDFD}}(\bar{L}_1, \bar{L}_2)$, which meets all the specifications (Figure 3.4). The initial point for the algorithm is the optimal solution of the coarse transmission line model (Eq. 3.8)

$$[L_1^{(1)} \quad L_2^{(1)}]^T = [L^*_{\mathrm{TL1}} \quad L^*_{\mathrm{TL2}}]^T = [210 \text{ nm} \quad 384 \text{ nm}]^{\mathrm{T}}. \tag{3.21}$$

We then follow the iterative process described in Section 3.2.1. At each step of the algorithm the next approximation to the solution is found using Equations 3.9 and 3.10. The design parameters $L_1^{(j)}$, $L_2^{(j)}$ found after the jth iteration of the algorithm are shown in Table 3.1. Figure 3.3 shows the transmission response of the device $T_{\mathrm{FDFD}}(L_1^{(j)}, L_2^{(j)})$ after the jth iteration calculated with the fine FDFD model. The device response from the initial step of the algorithm $T_{\mathrm{FDFD}}(L_1^{(1)}, L_2^{(1)})$, which as mentioned above is obtained from the optimal solution of the coarse transmission line model, does not meet the desired specifications. The device response obtained after the second iteration $T_{\mathrm{FDFD}}(L_1^{(2)}, L_2^{(2)})$ satisfies the specifications in almost the entire frequency range (Figure 3.4). Finally, after the third iteration the transmission response of the device $T_{\mathrm{FDFD}}(L_1^{(3)}, L_2^{(3)})$ calculated with the fine FDFD model satisfies the specifications in the entire frequency range (Figure 3.4). Thus, in this example the space mapping algorithm results in a device which satisfies all the design specifications after only 3 iterations (Figure 3.5). In other words, full-wave FDFD simulations of only 3 candidate structures are required before the iterative process

is terminated. Use of the space mapping algorithm therefore results in large reductions in the required computation time when compared to any direct optimization method of the fine FDFD model.

Table 3.1: The design parameters $L_1^{(j)}$, $L_2^{(j)}$ found after jth iteration of the space mapping algorithm for the structure of Figure 3.1.

	$j = 1$	$j = 2$	$j = 3$
$L_1^{(j)}$ (nm)	210	182	180
$L_2^{(j)}$ (nm)	384	349	351

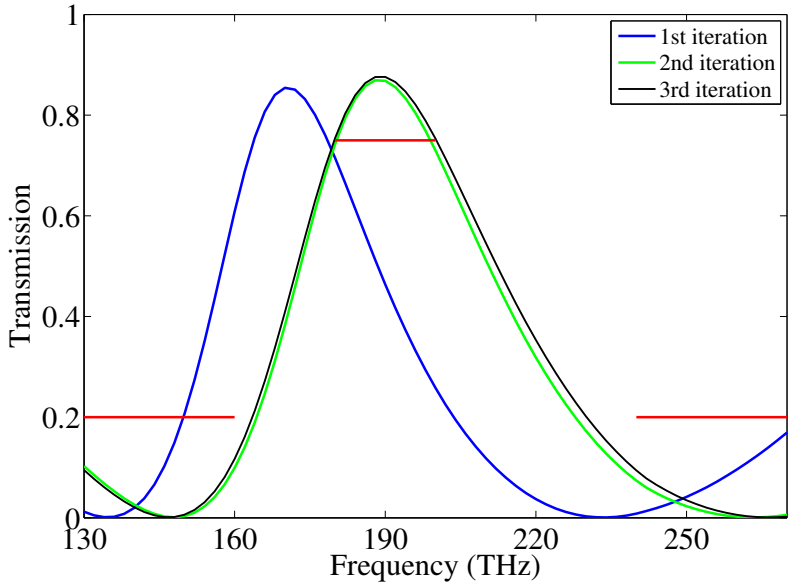

Figure 3.5: Transmission response $T_{\text{FDFD}}(L_1^{(j)}, L_2^{(j)})$ of the structure of Figure 3.1 calculated with FDFD for parameters obtained after the jth iteration of the space mapping algorithm. $L_1^{(j)}, L_2^{(j)}$ for $j = 1, 2, 3$ are given in Table 3.1. All other parameters are as in Figure 3.3.

At each iteration of the space mapping algorithm, we use the parameter extraction procedure described in Subsection 3.2.2 to obtain the mapping which corresponds to the optimum match between the coarse transmission line and fine FDFD model responses. The objective function H to be minimized during the parameter extraction (Eq. 3.15) is based on the model responses at 15 frequency points from 130 THz to 270 THz with a step of 10 THz. In Figure 3.6 we show the device response from the initial step of the algorithm

$T_{\text{FDFD}}(L_1^{(1)}, L_2^{(1)})$ (solid line). Using the parameter extraction procedure, we obtain the mapping $[L_{\text{TL1}}^{(1)} \quad L_{\text{TL2}}^{(1)}]^T = \mathbf{P}([L_1^{(1)} \quad L_2^{(1)}]^T) = [238 \text{ nm} \quad 419 \text{ nm}]^T$. In Figure 3.6 we also show the corresponding coarse transmission line model response $T_{\text{TL}}(L_{\text{TL1}}^{(1)}, L_{\text{TL2}}^{(1)})$ (circles). We observe that there is very good agreement between the device response $T_{\text{FDFD}}(L_1^{(1)}, L_2^{(1)})$ and the transmission line model response $T_{\text{TL}}(L_{\text{TL1}}^{(1)}, L_{\text{TL2}}^{(1)})$ obtained through the parameter extraction procedure in the entire frequency range. This demonstrates that a mapping $\mathbf{P}$ that relates the fine FDFD and the coarse transmission line model parameters through $\mathbf{L}_{\text{TL}} = \mathbf{P}(\mathbf{L})$ can indeed be established such that $T_{\text{TL}}(\mathbf{P}(\mathbf{L})) \simeq T_{\text{FDFD}}(\mathbf{L})$ in the frequency range of interest. It is the existence of such a one-to-one mapping that enables the space mapping algorithm to converge to a desired design after a few iterations. If a one-to-one mapping between the fine and coarse models cannot be established, the algorithm may fail to converge [65].

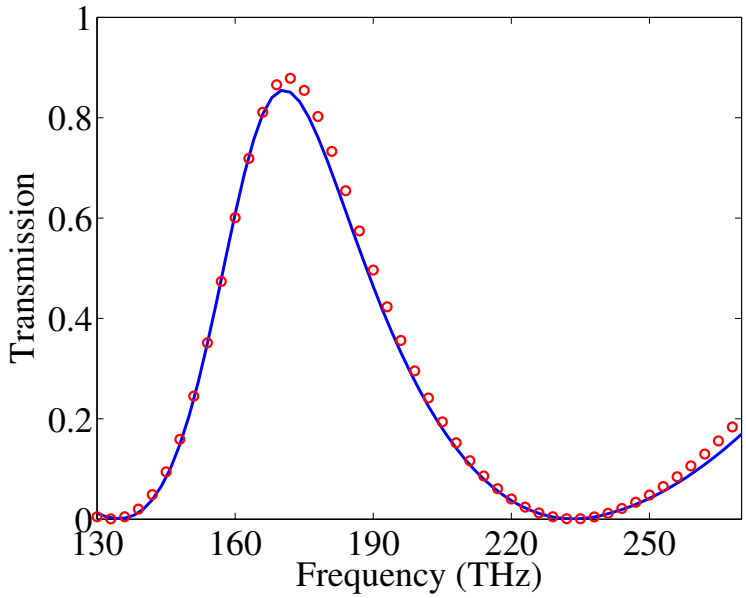

Figure 3.6: Transmission response $T_{\text{FDFD}}(L_1^{(1)}, L_2^{(1)})$ of the structure of Figure 3.1 calculated with FDFD (solid line) for parameters obtained after the first iteration of the space mapping algorithm. We also show the coarse transmission line model response $T_{\text{TL}}(L_{\text{TL1}}^{(1)}, L_{\text{TL2}}^{(1)})$ (circles), where $L_{\text{TL1}}^{(1)}$, $L_{\text{TL2}}^{(1)}$ are obtained through the parameter extraction procedure described in Subsection 3.2.2.

3.3.2 MDM waveguide side-coupled to two arrays of MDM stub resonators

We next consider an example in which space mapping is applied to the design of a multicomponent nanoplasmonic device. The structure consists of a MDM plasmonic waveguide side-coupled to two arrays of MDM stub resonators [79] (Figure 3.7). The fundamental TM mode of the MDM waveguide is incident from the left.

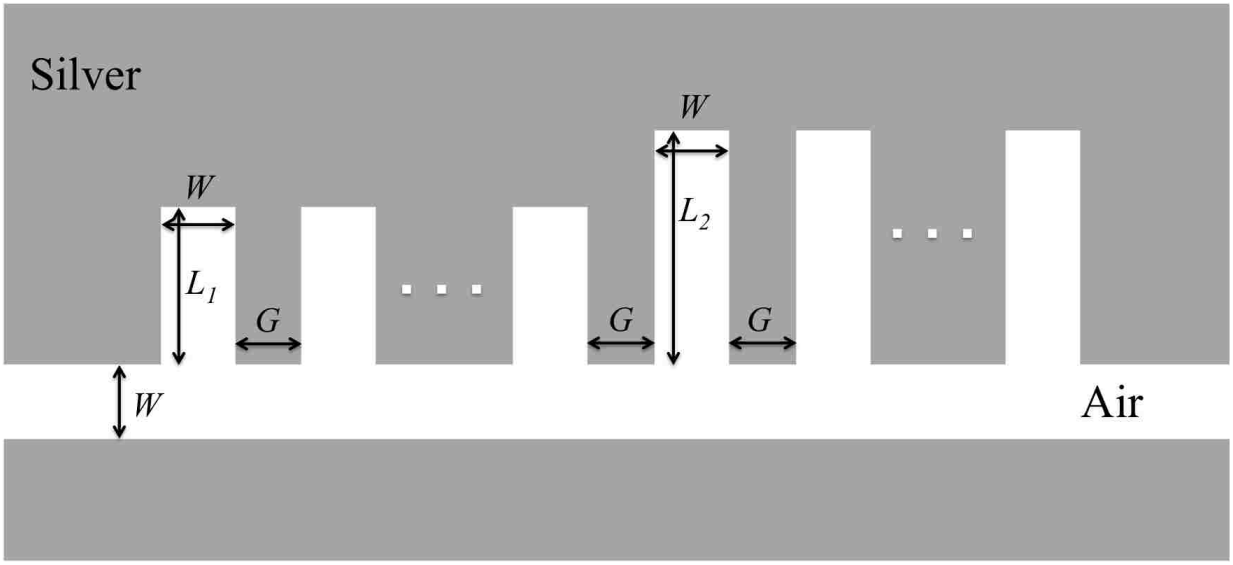

Figure 3.7: Schematic of a MDM plasmonic waveguide side-coupled to two arrays of MDM stub resonators.

As in the previous example, we wish to design a structure with a bandpass filter response. In the waveguide device geometry of Figure 3.7 the use of multiple stubs can reduce the transmission in the stopbands. In addition, the use of two stub arrays with different stub lengths can result in narrower bandwidth of the passband [79]. In this case, the design specifications imposed on the transmission response T of the structure (indicated in Figures 3.9 and 3.10 with solid red lines) are:

$$T > 0.5 \quad \text{for} \quad 190 \text{ THz} < f < 200 \text{ THz}, \tag{3.22a}$$

$$T < 0.03 \quad \text{for} \quad 110 \text{ THz} < f < 160 \text{ THz} \quad \text{and} \quad 230 \text{ THz} < f < 290 \text{ THz}. \tag{3.22b}$$

Here the design parameters are the lengths of the stub resonators in the two arrays L_1 and L_2, as well as the distance L_3 between two adjacent stubs. The width w of all waveguide sections is fixed at $w = 50$ nm. The first and second array consist of 3 and 4 stubs, respectively.

Based on transmission line theory, the transmission line model of this structure consists of a transmission line with propagation constant γ and characteristic impedance Z loaded with two arrays of short-circuited transmission line stub resonators of lengths L_{TL1} and L_{TL2} with the same propagation constant γ and characteristic impedance Z (Figure 3.8). The distance between two adjacent transmission line stub resonators is L_{TL3}. The characteristic impedance Z is given by Eq. 3.19. To obtain the transmission line model response of the structure $T_{\text{TL}}(L_{\text{TL1}}, L_{\text{TL2}}, L_{\text{TL3}})$, each of the MDM waveguide sections of the multicomponent device is modeled using a 2×2 transfer matrix [80, 75]. The overall transfer matrix is obtained by multiplying the transfer matrices of the individual components (Appendix B) [75].

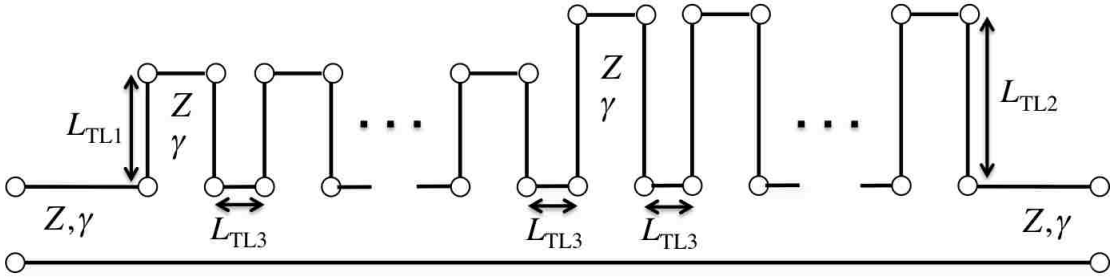

Figure 3.8: Schematic of the transmission line model for the structure of Figure 3.7. Here $Z(\omega)$ and $\gamma(\omega)$ are the characteristic impedance and complex propagation constant of the fundamental TM mode of a silver-air-silver plasmonic waveguide with width w.

As in the previous example, the transmission line model of this structure is computationally efficient but its accuracy is limited. We use the coarse transmission line model of the structure (without space mapping) in combination with the genetic global optimization algorithm to find the transmission line model parameters L_{TL1}, L_{TL2}, and L_{TL3} such that the transmission line model response $T_{\text{TL}}(L_{\text{TL1}}, L_{\text{TL2}}, L_{\text{TL3}})$ satisfies the design specifications. The optimal transmission line model parameters found using this approach are $L^*_{\text{TL1}} = 183$ nm, $L^*_{\text{TL2}} = 466$ nm, and $L^*_{\text{TL3}} = 229$ nm. As shown in Figure 3.9, the transmission line model response for the optimized device $T_{\text{TL}}(L^*_{\text{TL1}}, L^*_{\text{TL2}}, L^*_{\text{TL3}})$ (dashed blue line) meets all the design specifications (Eq. 3.22).

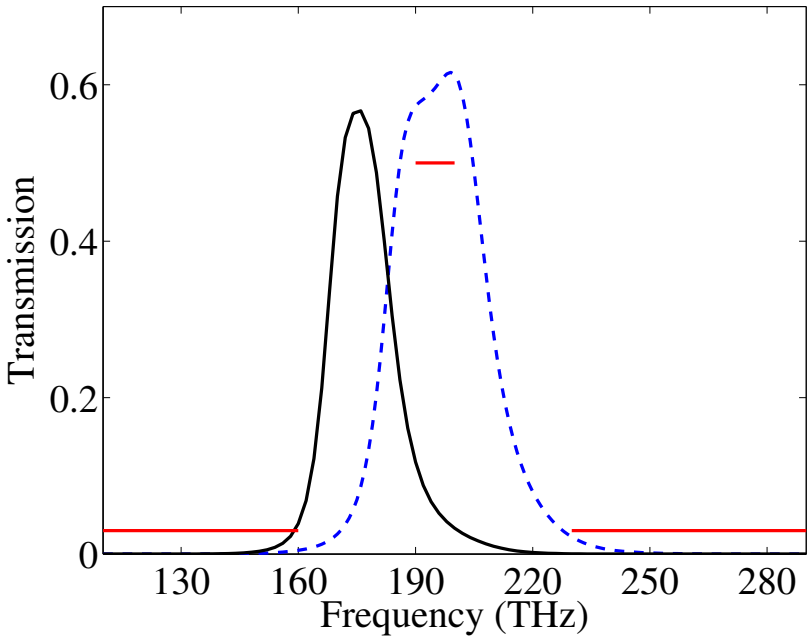

Figure 3.9: Transmission line model response $T_{\text{TL}}(L^*_{\text{TL1}}, L^*_{\text{TL2}}, L^*_{\text{TL3}})$ of the structure of Figure 3.7 for parameters $L^*_{\text{TL1}} = 183$ nm, $L^*_{\text{TL2}} = 466$ nm, and $L^*_{\text{TL3}} = 229$ nm obtained by optimizing the transmission line model of Figure 3.8 (dashed blue line). We also show the transmission response calculated using FDFD, $T_{\text{FDFD}}(L_1 = L^*_{\text{TL1}}, L_2 = L^*_{\text{TL2}}, L_3 = L^*_{\text{TL3}})$ for the same parameters (solid black line). Results are shown for $w = 50$ nm. The red lines are the design specifications imposed on the transmission response of this structure.

As in the previous example, we investigate whether optimizing the transmission line model of the structure is enough to obtain a device which satisfies all the design specifications. We therefore perform a full-wave FDFD simulation of the device setting the design parameters L_1, L_2, L_3 equal to the optimal transmission line model parameters, and obtain the device response $T_{\mathrm{FDFD}}(L_1 = L^*_{\mathrm{TL1}}, L_2 = L^*_{\mathrm{TL2}}, L_3 = L^*_{\mathrm{TL3}})$. We observe that the transmission response of the device obtained with this approach $T_{\mathrm{FDFD}}(L_1 = L^*_{\mathrm{TL1}}, L_2 = L^*_{\mathrm{TL2}}, L_3 = L^*_{\mathrm{TL3}})$ (black solid line) is substantially different from the transmission line model response $T_{\mathrm{TL}}(L^*_{\mathrm{TL1}}, L^*_{\mathrm{TL2}}, L^*_{\mathrm{TL3}})$ (dashed blue line), and does not meet all the desired specifications (Figure 3.9). This is due to the limited accuracy of the transmission line model which was discussed above. Thus, as in the previous example, simply optimizing the transmission line model of the device is not enough to obtain a device which satisfies all the required design specifications.

We therefore then use the space mapping algorithm (Section 3.2), to obtain a device which will satisfy all the design specifications. The objective function H to be minimized during the parameter extraction (Eq. 3.15) is based on the coarse transmission line and fine FDFD model responses at 21 frequency points from 100 THz to 300 THz with a step of 10 THz. The design parameters $L_1^{(j)}$, $L_2^{(j)}$, $L_3^{(j)}$ found after the jth iteration of the algorithm are shown in Table 3.2. In this example the space mapping algorithm results in the design $\bar{L}_1 = 159$ nm, $\bar{L}_2 = 439$ nm, $\bar{L}_3 = 196$ nm, which satisfies all the design specifications (Figure 3.10), after only 3 iterations. Thus, as in the previous example, the use of the space mapping algorithm results in large reductions in the required computation time when compared to any direct optimization method of the fine FDFD model.

3.3.3 Two nanorods juxtaposed in parallel in a waveguide

We also consider an example where space mapping is applied to the design of a nanoplasmonic device which includes deep subwavelength dielectric and metallic structures. Due to their deep subwavelength dimensions, these structures are modeled as lumped circuit

Table 3.2: The design parameters $L_1^{(j)}$, $L_2^{(j)}$, and $L_3^{(j)}$ found after jth iteration of the space mapping algorithm for the structure of Figure 3.7.

	$j = 1$	$j = 2$	$j = 3$
$L_1^{(j)}$ (nm)	183	156	159
$L_2^{(j)}$ (nm)	466	439	439
$L_3^{(j)}$ (nm)	229	196	196

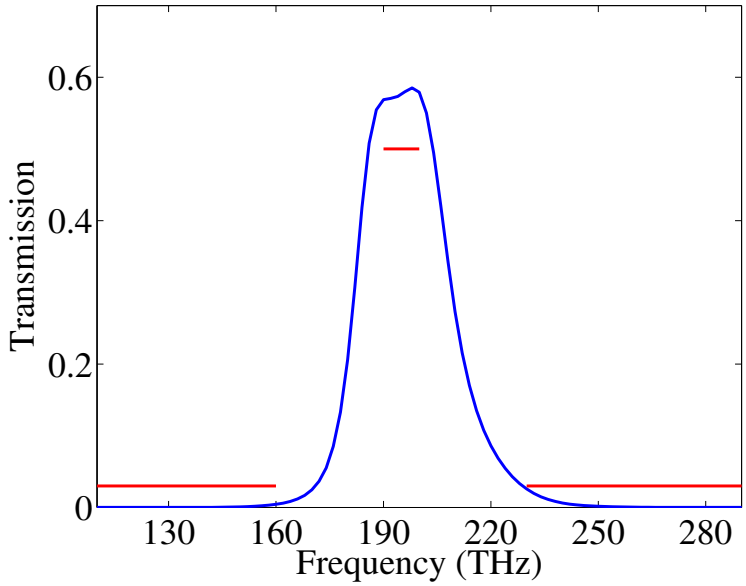

Figure 3.10: Transmission response $T_{\text{FDFD}}(\bar{L}_1, \bar{L}_2, \bar{L}_3)$ of the structure of Figure 3.7 calculated with FDFD for the parameters $\bar{L}_1 = 159$ nm, $\bar{L}_2 = 439$ nm, and $\bar{L}_3 = 196$ nm obtained by the space mapping algorithm.

elements rather than as transmission lines. In this example, the plasmonic device consists of a silicon ($\epsilon_r = 14.15$) and a silver nanorod juxtaposed in parallel in a waveguide [81, 82] (Figure 3.11). The parallel-plate waveguide is bounded on top and bottom by perfect electric conductors (PEC), which represent an impenetrable metal with sufficiently negative permittivity in the frequency range of interest [82]. The nanorods are connected to a PEC protrusion attached to the bottom of the waveguide (Figure 3.11). The fundamental TEM mode of the parallel-plate waveguide is incident from the left.

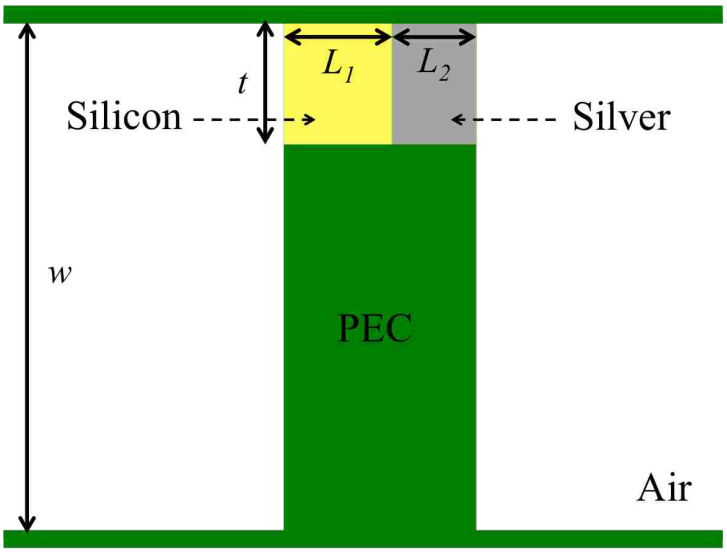

Figure 3.11: Schematic of a nanoplasmonic waveguide device consisting of a silicon and a silver nanorod juxtaposed in parallel in a waveguide. The parallel-plate waveguide is bounded on top and bottom by perfect electric conductors (PEC). The nanorods are connected to a PEC protrusion attached to the bottom of the waveguide.

Here we wish to use the plasmonic waveguide device of Figure 3.11, which is based on two optical lumped nanocircuit elements, to design a structure with a bandpass filter response. More specifically, the design specifications imposed on the transmission response T of the structure are

$$T > 0.36 \quad \text{for} \quad 330 \text{ THz} < f < 360 \text{ THz}, \tag{3.23a}$$

$$T < 0.18 \quad \text{for} \quad 120 \text{ THz} < f < 270 \text{ THz} \quad \text{and} \quad 420 \text{ THz} < f < 630 \text{ THz}. \tag{3.23b}$$

The specifications are indicated in Figures 3.13 and 3.14 with solid red lines. Here the design parameters are the lengths of the silicon and silver nanorods L_1 and L_2, while the width w of the waveguide and t of the nanorods are fixed at $w = 50$ nm and $t = 10$ nm, respectively.

As mentioned above, the nanorods can be modeled as lumped circuit elements [82]. More specifically, since the dielectric constant of silicon is real and positive, the silicon

nanorod is modeled as a lumped capacitor with a capacitance per unit length given by [82]

$$C = \epsilon_0 \epsilon_r \frac{L_1}{t}. \tag{3.24}$$

In addition, since the real part of the dielectric constant of silver is negative in the frequency range of interest, the silver nanorod is modeled as a lumped inductor in parallel to a lumped resistor. Here the resistor accounts for the material losses in the silver nanorod. The inductance and resistance per unit length are associated with the real and imaginary parts of the dielectric constant of silver, respectively, and are given by [82]

$$L = -\frac{t}{\omega^2 \mathrm{Re}(\epsilon_m) L_2}, \tag{3.25}$$

$$R = \frac{t}{\omega \mathrm{Im}(\epsilon_m) L_2}, \tag{3.26}$$

where ϵ_m is the dielectric permittivity of silver. Thus, overall the silicon and silver nanorods are equivalent to the parallel combination of a resistor, an inductor, and a capacitor. The transmission line model of the waveguide device of Figure 3.11 therefore consists of a shunt impedance Z_t coupled in parallel to a transmission line with characteristic impedance Z_0 (Figure 3.12). Here the shunt impedance is given by

$$Z_t = (Z_C^{-1} + R^{-1} + Z_L^{-1})^{-1} = [j\omega C + R^{-1} + (j\omega L)^{-1}]^{-1}, \tag{3.27}$$

while the characteristic impedance of the PEC parallel-plate waveguide is [73]

$$Z_0 = \sqrt{\frac{\mu_0}{\epsilon_0}} w. \tag{3.28}$$

Based on transmission line theory, the transmission line model response $T_{\mathrm{TL}}(L_{\mathrm{TL1}}, L_{\mathrm{TL2}})$ of the structure of Figure 3.11 can be calculated as (Appendix B) [73]

$$T_{\mathrm{TL}} = \left| \frac{2Z_t}{2Z_t + Z_0} \right|^2 . \tag{3.29}$$

As in the previous examples, we first use the coarse transmission line model of the structure (without space mapping) in combination with the genetic global optimization algorithm to find the nanorod lengths L_{TL1} and L_{TL2} such that the transmission line model response $T_{\mathrm{TL}}(L_{\mathrm{TL1}}, L_{\mathrm{TL2}})$ satisfies the design specifications. The optimal transmission line model nanorod lengths found using this approach are $L^*_{\mathrm{TL1}} = 20$ nm and $L^*_{\mathrm{TL2}} = 7$ nm. As shown in Figure 3.13, the transmission line model response for the optimized device $T_{\mathrm{TL}}(L^*_{\mathrm{TL1}}, L^*_{\mathrm{TL2}})$ (dashed blue line) meets all the design specifications (Eq. 3.23). As in previous examples, we then investigate whether optimizing the transmission line model of the structure is enough to obtain a device which satisfies all the design specifications. We therefore perform a full-wave FDFD simulation of the device setting the nanorod lengths L_1, L_2 equal to the optimal transmission line model nanorod lengths, and obtain the device response $T_{\mathrm{FDFD}}(L_1 = L^*_{\mathrm{TL1}}, L_2 = L^*_{\mathrm{TL2}})$. We observe that the transmission response of the device obtained with this approach $T_{\mathrm{FDFD}}(L_1 = L^*_{\mathrm{TL1}}, L_2 = L^*_{\mathrm{TL2}})$ (black solid line) is different from the transmission line model response $T_{\mathrm{TL}}(L^*_{\mathrm{TL1}}, L^*_{\mathrm{TL2}})$ (dashed blue line), and does not meet all the desired specifications (Figure 3.13). This is due to the limited

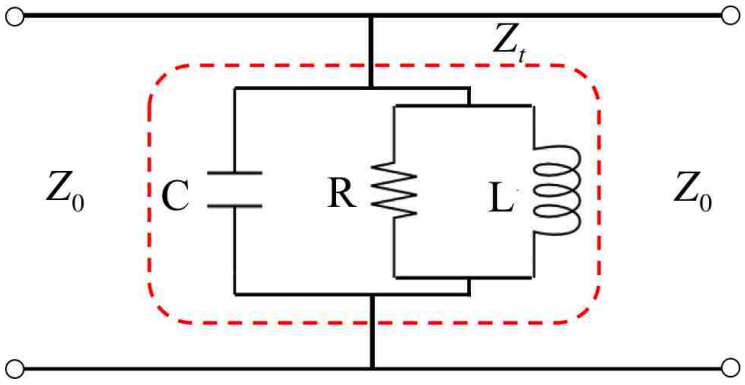

Figure 3.12: Schematic of the transmission line model for the structure of Figure 3.11. Here Z_0 is the characteristic impedance of the PEC parallel-plate waveguide. The shunt impedance Z_t consists of the parallel combination of a capacitor, a resistor, and an inductor.

accuracy of the transmission line model. Thus, similarly to the previous examples, simply optimizing the transmission line model of the device is not enough to obtain a device which satisfies all the required design specifications.

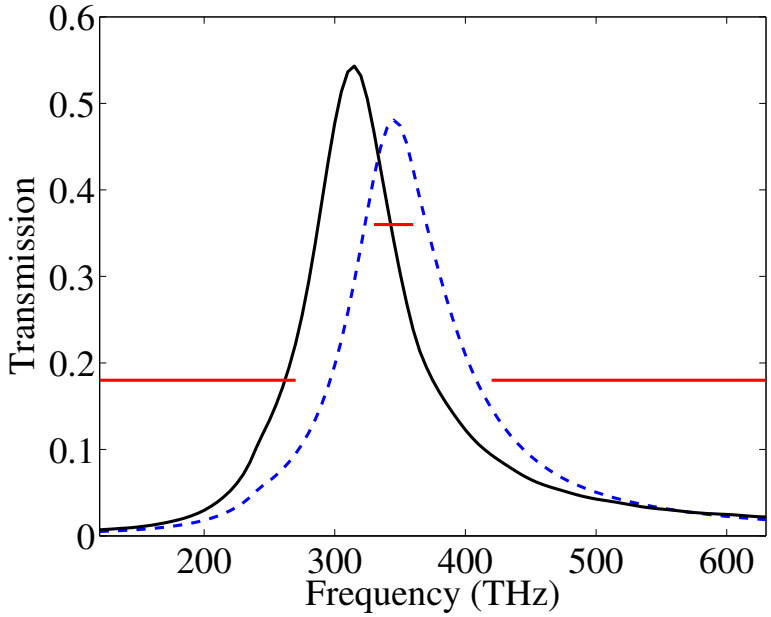

Figure 3.13: Transmission line model response $T_{\mathrm{TL}}(L^*_{\mathrm{TL1}}, L^*_{\mathrm{TL2}})$ of the structure of Figure 3.11 for parameters $L^*_{\mathrm{TL1}} = 20$ nm and $L^*_{\mathrm{TL2}} = 7$ nm obtained by optimizing the transmission line model of Figure 3.12 (dashed blue line). We also show the transmission response calculated using FDFD, $T_{\mathrm{FDFD}}(L_1 = L^*_{\mathrm{TL1}}, L_2 = L^*_{\mathrm{TL2}})$ for the same parameters (solid black line). Results are shown for $w = 50$ nm and $t = 10$ nm. The red lines are the design specifications imposed on the transmission response of this structure.

We therefore use the space mapping algorithm (Section 3.2), to obtain a device which will satisfy all the design specifications. As in the previous examples, the space mapping algorithm converges fast to the design $\bar{L}_1 = 20$ nm and $\bar{L}_2 = 9$ nm, which meets all the specifications (Figure 3.14). In this case, the objective function H to be minimized during the parameter extraction (Eq. 3.15) is based on the coarse transmission line and fine FDFD model responses at 18 frequency points from 120 THz to 630 THz with a frequency step of 30 THz. The design parameters $L_1^{(j)}$ and $L_2^{(j)}$ found after the jth iteration of the algorithm are shown in Table 3.3. In this case, only 2 iterations were required for the algorithm to converge to a design satisfying all the specifications. Thus, as in the previous examples, the

use of the space mapping algorithm results in large reductions in the required computation time when compared to any direct optimization method of the fine FDFD model.

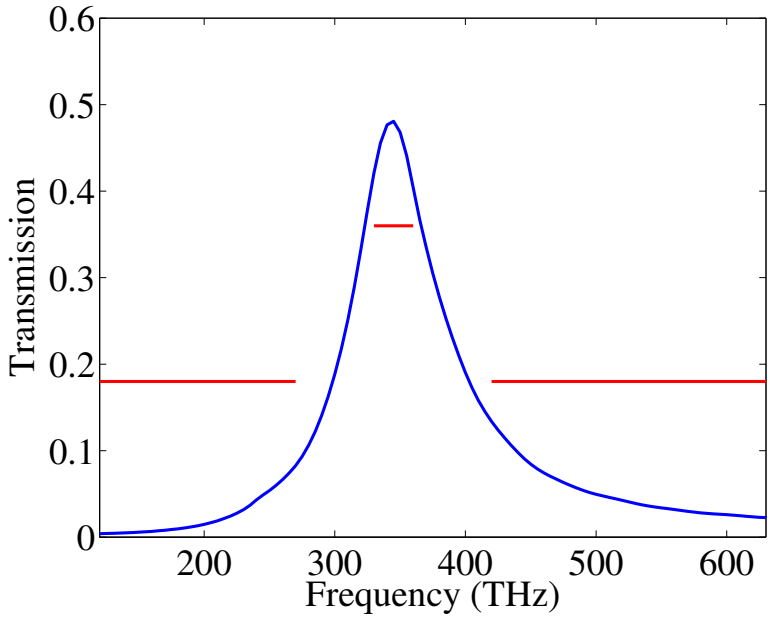

Figure 3.14: Transmission response $T_{\mathrm{FDFD}}(\bar{L}_1, \bar{L}_2)$ of the structure of Figure 3.11 calculated with FDFD for the parameters $\bar{L}_1 = 20$ nm and $\bar{L}_2 = 9$ nm obtained by the space mapping algorithm.

Table 3.3: The design parameters $L_1^{(j)}$, $L_2^{(j)}$ found after jth iteration of the space mapping algorithm for the structure of Figure 3.11.

	$j = 1$	$j = 2$
$L_1^{(j)}$ (nm)	20	20
$L_2^{(j)}$ (nm)	7	9

3.3.4 Emulation of 2D MDM plasmonic waveguide devices with 3D coaxial waveguide devices

Looking at the transmission spectra of a 3D plasmonic coaxial waveguide [83] side-coupled to two open-circuited coaxial stub resonators (Figure 3.15) one can see that they are very similar to that of a 2D MDM waveguide side-coupled to two MDM stub resonators [84]. Here we show that, by applying the space mapping algorithm and with proper choice of their design parameters, a 3D plasmonic coaxial waveguide-cavity device and a 2D MDM waveguide-cavity device can have nearly identical transmission spectra. Figure 3.16 shows

the top view schematic at $z = 0$ of the structure and Figure 3.17 shows the cross section of the coaxial waveguide used in the 3D device.

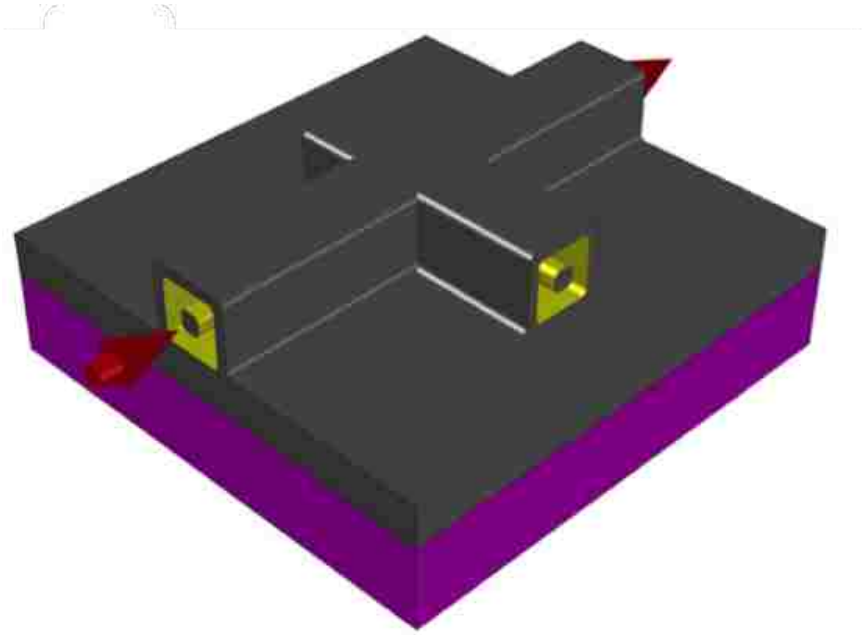

Figure 3.15: Schematic of a plasmonic coaxial waveguide side-coupled to two open-circuit coaxial stub resonators. The propagation direction of light is indicated by red arrows.

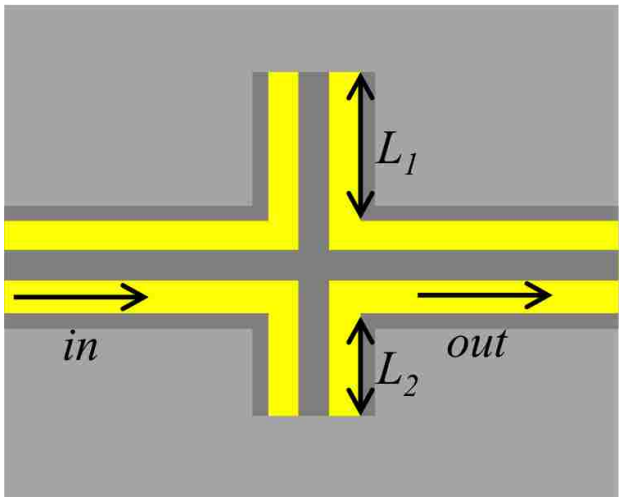

Figure 3.16: Top view schematic at $z = 0$ (Figure 3.17) of a plasmonic coaxial waveguide side-coupled to two open-circuit coaxial stub resonators.

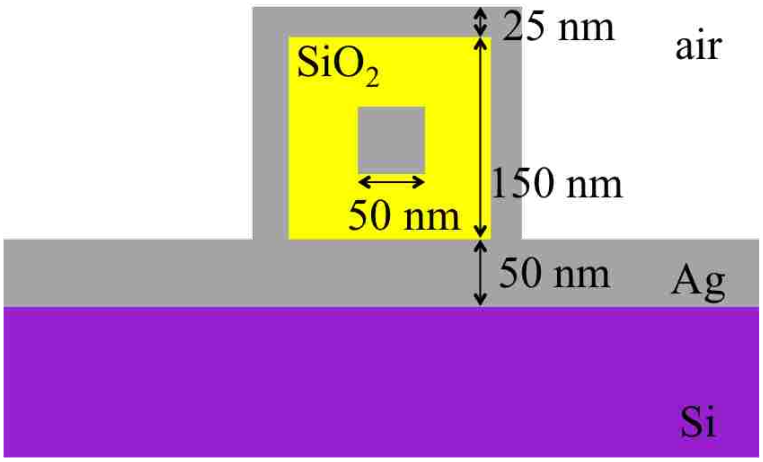

Figure 3.17: Cross section of the reference plasmonic coaxial waveguide.

More specifically, we consider a 2D silver-air-silver MDM plasmonic waveguide side-coupled to two short-circuited MDM stub resonators (Figure 3.18). The transmission spectra of the 3D plasmonic coaxial waveguide side-coupled to two open-circuited coaxial stub resonators are shown in Figure 3.19 (solid line). We use the space mapping algorithm to find the optimum match between the responses of the 2D (Figure 3.18) and 3D (Figure 3.15) plasmonic waveguide devices.

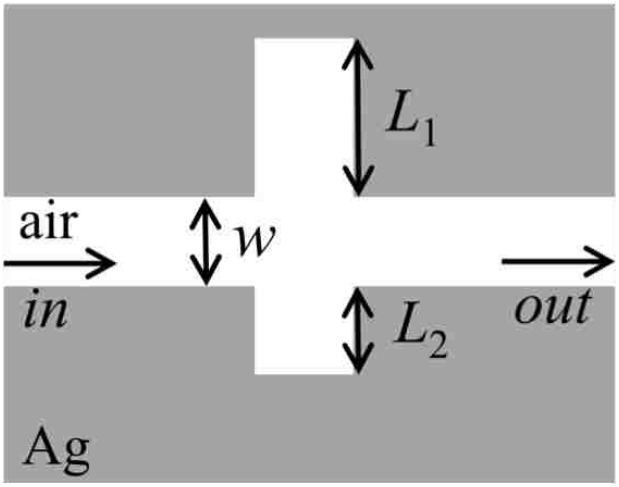

Figure 3.18: Schematic of a two-dimensional silver-air-silver MDM plasmonic waveguide side-coupled to two short-circuited MDM stub resonators.

Thus, the design specifications in this case are the transmission spectra of the 3D plasmonic coaxial waveguide side-coupled to two open-circuited coaxial stub resonators, and the design parameters are the stub lengths L_1, L_2. The width w of all waveguide sections is fixed at $w = 50$ nm. The objective function H to be minimized during the parameter extraction (Eq. 3.15) is based on the coarse transmission line and fine FDFD model responses at 13 frequency points from 100 THz to 340 THz with a step of 20 THz. In this example, only 3 iterations are required for the algorithm to satisfy the specifications.

Using this approach, we find that, when the stub lengths L_1 and L_2 of the 2D MDM device (Figure 3.18) are optimized, its transmission spectra almost exactly match the spectra of the 3D device (Figure 3.19).

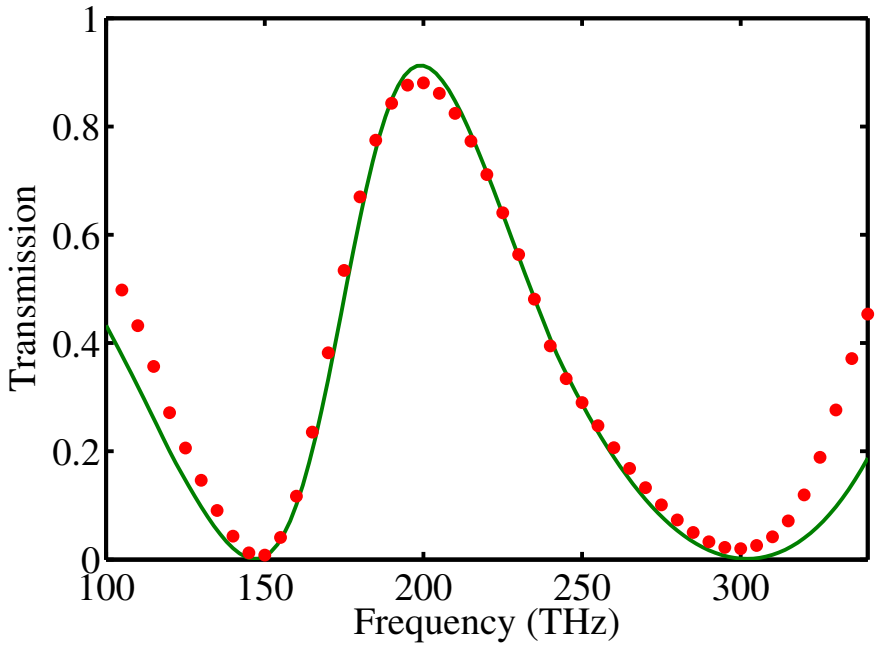

Figure 3.19: Transmission spectra for the two-dimensional structure of Figure 3.18 calculated using FDFD for $w = 50$ nm, $L_1 = 354$ nm, and $L_2 = 154$ nm (solid green line). Also shown are the transmission spectra for the three-dimensional structure of Figure 3.16 calculated using FDFD for $L_1 = 160$ nm and $L_2 = 42$ nm (red dots).

While here we found a 2D structure which matches the response of a 3D structure, the opposite process is also possible: we can use the space mapping algorithm to find a

3D structure with nearly identical response to that of a 2D structure. This is particularly useful for the practical implementation of plasmonic waveguide-cavity devices. Most of the theoretical investigations of plasmonic waveguide-cavity systems have focused on 2D structures [42, 72, 74, 85, 86, 87, 88, 89, 90, 91, 92, 93, 94]. This is due to the smaller computational cost of full-wave electromagnetic simulations in 2D compared to 3D, as well as the simplicity of visualizing and understanding the underlying optical physics in 2D [95]. However, practical realization of these waveguide-cavity systems requires the use of 3D structures. Since with proper choice of design parameters 3D plasmonic coaxial waveguide-cavity devices can have nearly identical transmission spectra to that of 2D MDM devices, the 2D designs can be translated into 3D designs suitable for experimental realization. Thus, 3D plasmonic coaxial waveguides offer a platform for practical implementation of 2D MDM devices.

Chapter 4
Sensitivity Analysis of Active Nanophotonic Devices

4.1 Introduction

It has been shown that plasmonic devices enable manipulating and guiding light at deep subwavelength scales using surface plasmons propagating at metal-dielectric interfaces. As was discussed in Chapter 1, in addition to developing passive nanooptical devices, it is also important to introduce devices which can actively control the flow of light at the nanoscale. In fact, active control of optical signals in plasmonic devices is one of the main challenges when designing efficient active devices such as switches, modulators or sensors. Recently, substantial progress in the development of active plasmonic devices has been achieved.

There are several different approaches to optimize photonic structures and devices [96]. If an optimization method uses local gradients, the adjoint method may be used to efficiently compute these [97]. In order to design an active optical device, it is important to calculate the effect of a small change of the refractive index of the active material on the device response function. For example, the device response function can be one of the eigenmodes of the system or the power transmission coefficient.

The adjoint variable method is one of the most efficient methods to calculate the sensitivity of a response function with respect to any design parameter. In the optimization process of a photonic device, in order to find the gradient of the response function with respect to all design parameters, it is usually required to perform an additional number of simulations, which is equal to the number of parameters. Fortunately, if the target function is specified in advance, using the adjoint variable method, one can calculate the gradient with respect to all device parameters with only one additional device simulation.

In general, the adjoint variable method utilizes the main simulation of the device along with an extra one called the adjoint simulation whose excitation is based on the response function. In a way, the adjoint solution enables us to calculate the effect of any parameter variation on the device response function, and using this solution one can avoid solving the main problem for each parameter variation. Interestingly, in some specific cases it is possible to reduce the required number of simulations from two to one by finding analytically a mapping between the solutions of the main and adjoint problems. This approach is called self adjoint variable method in which the sensitivities of the response function with respect to all design parameters are calculated without any extra simulations.

Although the adjoint variable method is not widely used in nanophotonic design, it is a well-known approach which has been implemented for various applications since the 1970s. For instance, it has been used in control theory as early as 1971 [98], and also in error estimation or propagation [99, 100], and fluid mechanics [101]. It was also utilized in performing aerodynamic shape optimizations [102, 103, 104, 105, 106], and structural design [107]. Electrical engineers have used it in the microwave regime first [108, 109, 110, 111], and recently the approach has been used in the optical wavelength range by a few groups [50, 112, 113, 114, 115, 116].

Here we present an analytical adjoint sensitivity method for the power transmission coefficient of nano-optical devices which is directly derived from Maxwell's equations and does not assume any discretization. Moreover, by deriving a formula which relates the fields of the adjoint problem and forward problem in symmetric devices, we could obtain the sensitivities with only one numerical simulation. In the second part of this chapter, we apply the derived formula to calculate the sensitivity of the power transmission coefficient with respect to the real and imaginary parts of the dielectric permittivity of the active material for two-dimensional and three-dimensional plasmonic devices. We also compare the results with the ones obtained by directly calculating the sensitivity. We find that there

is excellent agreement between the results obtained with the two methods. This is evidence that the derived formula gives accurate results for the plasmonic devices of interest.

4.2 Derivation of the analytical sensitivity formula

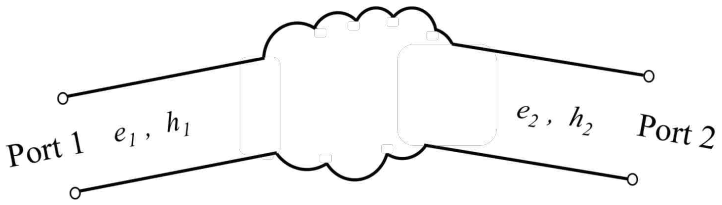

Figure 4.1: An arbitrary two-port device.

We consider a lossless two-port structure, and assume that a single (fundamental) mode is propagating in each port (Figure 4.1). The real modal vectors of electric $\mathbf{e}_i$ and magnetic $\mathbf{h}_i$ fields in the i^{th} port, which are biorthonormal [73, 117], can be normalized over the terminal plane of the port as:

$$\iint_{S_i} (\mathbf{e}_i \times \mathbf{h}_i) \cdot d\mathbf{s} = 1; \quad i = 1, 2, \tag{4.1}$$

where:

$$d\mathbf{s} = \mathbf{a}_n ds, \tag{4.2}$$

and $\mathbf{a}_n$ is the port unit normal vector, which in our case coincides with the direction of propagation. S_i is the cross section of the i^{th} port. $\mathbf{E}_i$ is the electric field resulting from exciting the i^{th} port, and $\mathbf{E}_i^{\text{inc}}$ is the incident field at the i^{th} port. A_i^{inc} is defined as the modal magnitude of the incident wave at the i^{th} port, and A_{ki} is defined as the modal magnitude of the wave at port k, when the structure is excited from the i^{th} port

$$A_i^{\text{inc}} \equiv \iint_{S_i} \left(\mathbf{E}_i^{\text{inc}} \times \mathbf{h}_i\right) \cdot d\mathbf{s}; \quad i = 1, 2, \tag{4.3}$$

$$A_{ki} \equiv \iint_{S_k} (\mathbf{E}_i \times \mathbf{h}_k) \cdot d\mathbf{s}; \quad i,k = 1,2. \tag{4.4}$$

The power transmission coefficient T at port 2 when the system is excited from port 1 is defined as:

$$T \equiv \frac{P_{\text{out}}}{P_{\text{in}}} = \frac{P_2}{P_0}, \tag{4.5}$$

in which $P_{\text{in}} = P_0$ represents the incident power at the input (port 1) and $P_{\text{out}} = P_2$ represents the output power at port 2. The output power can be written as:

$$P_{\text{out}} = \iint_{S_2} \frac{1}{2}\text{Re}\left(\mathbf{E}_1 \times \mathbf{H}_1^*\right) \cdot d\mathbf{s} = \iint_{S_2} \frac{1}{2}\text{Re}\left[(A_{21}\mathbf{e}_2) \times (A_{21}\mathbf{h}_2)^*\right] \cdot d\mathbf{s}. \tag{4.6}$$

Since the modal fields $\mathbf{e}_i$ and $\mathbf{h}_i$ are real, the power transmission coefficient (Eq. 4.5) can be rewritten as:

$$T = \frac{P_{\text{out}}}{P_{\text{in}}} = \frac{\iint_{S_2} \frac{1}{2}|A_{21}|^2(\mathbf{e}_2 \times \mathbf{h}_2) \cdot d\mathbf{s}}{P_0} = \frac{\iint_{S_2} \frac{1}{2}\left(A_{21}A_{21}^*\right)(\mathbf{e}_2 \times \mathbf{h}_2) \cdot d\mathbf{s}}{P_0}. \tag{4.7}$$

The sensitivity of the transmission T with respect to an optimizable parameter p is the derivative of T with respect to that parameter and can be calculated as:

$$\frac{dT}{dp} = \frac{1}{2P_0}\left\{\iint_{S_2}\left[\left(\frac{dA_{21}}{dp}\mathbf{e}_2\right) \times (A_{21}^*\mathbf{h}_2)\right] \cdot d\mathbf{s} + \iint_{S_2}\left[(A_{21}\mathbf{e}_2) \times \left(\frac{dA_{21}^*}{dp}\mathbf{h}_2\right)\right] \cdot d\mathbf{s}\right\}$$

$$= \frac{1}{2P_0}\iint_{S_2}\left[\left(\frac{dA_{21}}{dp}\mathbf{e}_2\right) \times (A_{21}^*\mathbf{h}_2)\right] \cdot d\mathbf{s} + \frac{1}{2P_0}\left\{\iint_{S_2}\left[\left(\frac{dA_{21}}{dp}\mathbf{e}_2\right) \times (A_{21}^*\mathbf{h}_2)\right] \cdot d\mathbf{s}\right\}^*$$

$$= \frac{1}{P_0}\text{Re}\left\{\iint_{S_2}\left[\left(\frac{dA_{21}}{dp}\mathbf{e}_2\right) \times (A_{21}^*\mathbf{h}_2)\right] \cdot d\mathbf{s}\right\} = \frac{1}{P_0}\text{Re}\left(C\right), \tag{4.8}$$

where C is defined as:

$$C \equiv \iint_{S_2} \left[\left(\frac{dA_{21}}{dp} \mathbf{e}_2 \right) \times (A_{21}^* \mathbf{h}_2) \right] \cdot d\mathbf{s} = \iint_{S_2} \left\{ [(A_{21}^* \mathbf{h}_2) \times \mathbf{a}_n] \cdot \left(\frac{dA_{21}}{dp} \mathbf{e}_2 \right) \right\} ds$$

$$= \iint_{S_2} \left\{ [(A_{21}^* \mathbf{h}_2) \times \mathbf{a}_n] \cdot \frac{d\mathbf{E}_1}{dp} \right\} ds. \tag{4.9}$$

The source free Maxwell's equations are:

$$\nabla \times \mathbf{H} - j\omega\epsilon \cdot \mathbf{E} = 0, \tag{4.10}$$

$$\nabla \times \mathbf{E} + j\omega\mu \cdot \mathbf{H} = 0. \tag{4.11}$$

The differentiation of them with respect to p gives:

$$\nabla \times \frac{d\mathbf{H}}{dp} - j\omega \frac{d\epsilon}{dp} \cdot \mathbf{E} - j\omega\epsilon \cdot \frac{d\mathbf{E}}{dp} = 0, \tag{4.12}$$

$$\nabla \times \frac{d\mathbf{E}}{dp} + j\omega \frac{d\mu}{dp} \cdot \mathbf{H} + j\omega\mu \cdot \frac{d\mathbf{H}}{dp} = 0. \tag{4.13}$$

We then introduce the adjoint fields which satisfy Maxwell's equations with the medium dielectric permittivity and magnetic permeability tensors being the transpose of those in the original problem [118]:

$$\nabla \times \hat{\mathbf{H}} - j\omega\epsilon^T \cdot \hat{\mathbf{E}} = 0, \tag{4.14}$$

$$\nabla \times \hat{\mathbf{E}} + j\omega\mu^T \cdot \hat{\mathbf{H}} = 0. \tag{4.15}$$

The adjoint fields also satisfy the same boundary conditions as the original fields. By mathematically manipulating Equations 4.12-4.15, we obtain the following equation [118]:

$$\nabla \cdot \left(\hat{\mathbf{E}} \times \frac{d\mathbf{H}}{dp} - \frac{d\mathbf{E}}{dp} \times \hat{\mathbf{H}} \right) = j\omega \left[\left(\frac{d\mu}{dp} \cdot \mathbf{H} \right) \cdot \hat{\mathbf{H}} - \left(\frac{d\epsilon}{dp} \cdot \mathbf{E} \right) \cdot \hat{\mathbf{E}} \right]. \tag{4.16}$$

Integrating Eq. 4.16 over the volume of the structure V_S and applying the divergence theorem leads to:

$$I_S \equiv \oiint_S \left(\hat{\mathbf{E}} \times \frac{d\mathbf{H}}{dp} - \frac{d\mathbf{E}}{dp} \times \hat{\mathbf{H}} \right) \cdot d\mathbf{s} = j\omega \iiint_{V_S} \left[\left(\frac{d\mu}{dp} \cdot \mathbf{H} \right) \cdot \hat{\mathbf{H}} - \left(\frac{d\epsilon}{dp} \cdot \mathbf{E} \right) \cdot \hat{\mathbf{E}} \right] dv. \tag{4.17}$$

From this point on, we assume that the medium is reciprocal and its constitutive tensors are symmetric:

$$\epsilon = \epsilon^T, \qquad \mu = \mu^T. \tag{4.18}$$

It can be shown that the parts of the surface integral I_S (Eq. 4.17) corresponding to perfect electric conductors (PEC), perfect magnetic conductors (PMC), and radiation/absorbing boundaries, which can be considered as radiation or reflection-free boundary conditions (RBC) vanish and the integral therefore reduces to the surfaces of the ports (Appendix C):

$$I_S = \sum_i \iint_{S_i} \left(\hat{\mathbf{E}} \times \frac{d\mathbf{H}}{dp} - \frac{d\mathbf{E}}{dp} \times \hat{\mathbf{H}} \right) \cdot d\mathbf{s}. \tag{4.19}$$

Using Maxwell's equations for the original (Eq. 4.11) and adjoint (Eq. 4.15) fields, and also their derivatives with respect to p we obtain:

$$\mathbf{H} = -\left(j\omega\mu\right)^{-1} \nabla \times \mathbf{E}, \tag{4.20}$$

$$\frac{d\mathbf{H}}{dp} = -\left(j\omega\mu\right)^{-1}\nabla\times\frac{d\mathbf{E}}{dp} - \mu^{-1}\frac{d\mu}{dp}\mathbf{H}, \tag{4.21}$$

$$\hat{\mathbf{H}} = -\left(j\omega\mu\right)^{-1}\nabla\times\hat{\mathbf{E}}, \tag{4.22}$$

$$\frac{d\hat{\mathbf{H}}}{dp} = -\left(j\omega\mu\right)^{-1}\nabla\times\frac{d\hat{\mathbf{E}}}{dp} - \mu^{-1}\frac{d\mu}{dp}\hat{\mathbf{H}}, \tag{4.23}$$

and substituting them in Eq. 4.19, the surface integral I_S can be rewritten as:

$$I_S = \sum_i \iint_{S_i} -\left(j\omega\mu\right)^{-1}\left[\hat{\mathbf{E}}\times\left(\nabla\times\frac{d\mathbf{E}}{dp}\right) - \frac{d\mathbf{E}}{dp}\times\left(\nabla\times\hat{\mathbf{E}}\right)\right]\cdot d\mathbf{s}. \tag{4.24}$$

Also, it is assumed that the ports are not affected by the change of parameter p ($\frac{d\mu}{dp} = 0$ at S_i). The following boundary conditions apply at the i^{th} port (see appendix D):

$$\mathbf{a}_n\times\left(\nabla\times\mathbf{E}\right) = \mathbf{U}_i^{\text{inc}} - P\left(\mathbf{E}\right), \quad i = 1, 2, \tag{4.25}$$

$$\mathbf{a}_n\times\left(\nabla\times\hat{\mathbf{E}}\right) = \hat{\mathbf{U}}_i^{\text{inc}} - P\left(\hat{\mathbf{E}}\right), \quad i = 1, 2, \tag{4.26}$$

in which P is a linear vector operator depending on the boundary condition. $\mathbf{U}_i^{\text{inc}}$ and $\hat{\mathbf{U}}_i^{\text{inc}}$ are the original and adjoint excitations at port i. Using these boundary conditions and applying the triple product to Eq. 4.24 give us:

$$I_S = \sum_i \iint_{S_i} \left(j\omega\mu\right)^{-1}\left\{\hat{\mathbf{E}}\cdot\left[\mathbf{a}_n\times\left(\nabla\times\frac{d\mathbf{E}}{dp}\right)\right] - \frac{d\mathbf{E}}{dp}\cdot\left[\mathbf{a}_n\times\left(\nabla\times\hat{\mathbf{E}}\right)\right]\right\} ds$$

$$= \sum_i \iint_{S_i} \left(j\omega\mu\right)^{-1}\left\{\hat{\mathbf{E}}\cdot\left[\frac{d\mathbf{U}_i^{\text{inc}}}{dp} - P\left(\frac{d\mathbf{E}}{dp}\right)\right] - \frac{d\mathbf{E}}{dp}\cdot\left[\hat{\mathbf{U}}_i^{\text{inc}} - P\left(\hat{\mathbf{E}}\right)\right]\right\} ds$$

$$= \sum_i \left\{ \iint_{S_i} (j\omega\mu)^{-1} \left[-\hat{\mathbf{E}} \cdot P\left(\frac{d\mathbf{E}}{dp}\right) + \frac{d\mathbf{E}}{dp} \cdot P\left(\hat{\mathbf{E}}\right) \right] ds \right.$$
$$\left. + \iint_{S_i} (j\omega\mu)^{-1} \hat{\mathbf{E}} \cdot \frac{d\mathbf{U}_i^{\text{inc}}}{dp} ds - \iint_{S_i} (j\omega\mu)^{-1} \frac{d\mathbf{E}}{dp} \cdot \hat{\mathbf{U}}_i^{\text{inc}} ds \right\}. \quad (4.27)$$

It can be shown that [119]:

$$\iint_{S_i} \hat{\mathbf{E}} \cdot P\left(\frac{d\mathbf{E}}{dp}\right) ds = \iint_{S_i} \frac{d\mathbf{E}}{dp} \cdot P\left(\hat{\mathbf{E}}\right) ds. \quad (4.28)$$

Considering that the ports are not affected by the change of the parameter p, we have $\frac{d\mathbf{U}_i^{\text{inc}}}{dp} = 0$. By applying this into Eq. 4.27, and using Eq. 4.28 I_S simplifies to:

$$I_S = -\sum_i \iint_{S_i} \frac{d\mathbf{E}}{dp} \cdot (j\omega\mu)^{-1} \cdot \hat{\mathbf{U}}_i^{\text{inc}} ds. \quad (4.29)$$

It is obvious that, if the adjoint source is set to be :

$$\begin{cases} \hat{\mathbf{U}}_1^{\text{inc}} = 0, \\ \hat{\mathbf{U}}_2^{\text{inc}} = -j\omega A_{21}^* \mu \cdot (\mathbf{h}_2 \times \mathbf{a}_n), \end{cases} \quad (4.30)$$

then inserting Eq. 4.30 into Eq. 4.29, and using Eq. 4.9 we obtain:

$$I_S = C. \quad (4.31)$$

Finally, using Eq. 4.17 we get:

$$I_S = C = j\omega \iiint_{V_S} \left[\left(\frac{d\mu}{dp} \cdot \mathbf{H}_1 \right) \cdot \hat{\mathbf{H}}_2 - \left(\frac{d\epsilon}{dp} \cdot \mathbf{E}_1 \right) \cdot \hat{\mathbf{E}}_2 \right] dv, \quad (4.32)$$

and the formula for the sensitivity of transmission (Eq. 4.8) can be written as:

$$\frac{dT}{dp} = \frac{1}{P_0}\mathrm{Re}\left(j\omega \iiint_{V_S}\left[\left(\frac{d\mu}{dp}\cdot\mathbf{H}_1\right)\cdot\hat{\mathbf{H}}_2 - \left(\frac{d\epsilon}{dp}\cdot\mathbf{E}_1\right)\cdot\hat{\mathbf{E}}_2\right]dv\right). \tag{4.33}$$

Since the modal vector $\mathbf{h}_2$ at the second port describes a propagating mode, it satisfies the boundary condition (Appendix D):

$$\mathbf{a}_n \times (j\omega\mu\cdot\mathbf{h}_2) = P(\mathbf{e}_2). \tag{4.34}$$

Substituting Eq. 4.34 into Eq. 4.30 we obtain:

$$\hat{\mathbf{U}}_2^{\mathrm{inc}} = A_{21}^* P(\mathbf{e}_2). \tag{4.35}$$

In the original simulation, if the second port is excited, we have:

$$\mathbf{U}_2^{\mathrm{inc}} = 2P\left(\mathbf{E}_2^{\mathrm{inc}}\right) = 2P\left(A_2^{\mathrm{inc}}\mathbf{e}_2\right) = 2A_2^{\mathrm{inc}}P(\mathbf{e}_2), \tag{4.36}$$

where we used the fact that P is a linear operator. Eq. 4.36 can also be written as:

$$P(\mathbf{e}_2) = \frac{\mathbf{U}_2^{\mathrm{inc}}}{2A_2^{\mathrm{inc}}}. \tag{4.37}$$

Inserting Eq. 4.37 into Eq. 4.35, we get:

$$\hat{\mathbf{U}}_2^{\mathrm{inc}} = A_{21}^* \frac{1}{2A_2^{\mathrm{inc}}}\mathbf{U}_2^{\mathrm{inc}}. \tag{4.38}$$

Considering the fact that the adjoint fields satisfy the same Maxwell's equations and the same boundary conditions as the original fields and with the assumption of having reciprocal media, we can calculate the fields of the adjoint problem by the forward problem fields:

$$\hat{\mathbf{E}}_2 = A_{21}^* \frac{1}{2A_2^{\mathrm{inc}}}\mathbf{E}_2. \tag{4.39}$$

Now, if we want to calculate the sensitivity of the transmission with respect to the relative dielectric permittivity of a part of the device, such as the cavity of a switch which is filled by active material, the volume integral of Eq. 4.32 reduces to the volume V_C, where $\frac{d\epsilon}{dp}$ is nonzero, and applying $p = \epsilon_r$ leads to:

$$I_S = C = j\omega \iiint_{V_C} -\epsilon_0 \mathbf{E}_1 \cdot \hat{\mathbf{E}}_2 dv =$$

$$= \frac{-j\omega\epsilon_0 A_{21}^*}{2A_2^{\text{inc}}} \iiint_{V_C} \mathbf{E}_1 \cdot \mathbf{E}_2 dv. \tag{4.40}$$

Consequently, only the fields in the volume where the dielectric permittivity is perturbed contribute to the calculation of the sensitivity, and the sensitivity of the transmission of the structure with respect to the relative dielectric permittivity is:

$$\frac{dT}{d\epsilon_r} = \frac{1}{P_0}\text{Re}\left(C\right) = -\frac{\omega\epsilon_0}{2P_0}\text{Re}\left(\frac{jA_{21}^*}{A_2^{\text{inc}}} \iiint_{V_C} \mathbf{E}_1 \cdot \mathbf{E}_2 dv\right), \tag{4.41}$$

requiring the field solutions $\mathbf{E}_1$ and $\mathbf{E}_2$ due to the excitations at ports 1 and 2, respectively. These field solutions can be obtained by any simulator which has the ability to export all field components in any part of the analyzed volume. Most commercial EM simulators include this feature. In addition, if the structure is symmetric with respect to the $z = 0$ plane (Figure 4.2), we can directly obtain $\mathbf{E}_2$ from $\mathbf{E}_1$. More specifically, let us assume that the structure is symmetric with respect to a vertical mirror plane which bisects the cavity (red dashed line in Figure 4.2). Then, if we excite the structure from port 1 with the same excitation which we used for $\mathbf{E}_2$, we have:

$$A_2^{\text{inc}} = A_1^{\text{inc}}, \tag{4.42}$$

and the "flipped" electric field inside the cavity $\mathbf{E}_1^f$ will be equal to the electric field when the structure is excited from port 2 $\mathbf{E}_2$ and vice versa:

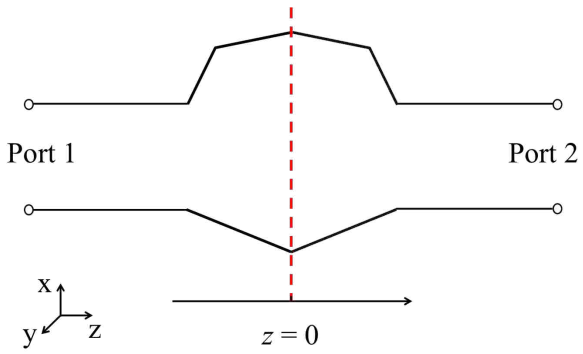

Figure 4.2: A symmetric two-port device.

$$\mathbf{E}_2 = \mathbf{E}_1^f. \tag{4.43}$$

More specifically, if $z = 0$ is the mirror plane bisecting the cavity (and the overall structure), then the "flipped" electric field will be:

$$E_{1x}^f(z) = E_{1x}(-z), \tag{4.44}$$

$$E_{1y}^f(z) = E_{1y}(-z), \tag{4.45}$$

$$E_{1z}^f(z) = -E_{1z}(-z). \tag{4.46}$$

Therefore, the sensitivity can be obtained by just a single simulation as:

$$\frac{dT}{d\epsilon_r} = \frac{1}{P_0}\mathrm{Re}(C) = -\frac{\omega\epsilon_0}{2P_0}\mathrm{Re}\left(\frac{jA_{21}^*}{A_1^{\mathrm{inc}}}\iiint_{V_C}\mathbf{E}_1\cdot\mathbf{E}_1^f dv\right). \tag{4.47}$$

If we assume that ϵ_r is a complex number, then we can find the sensitivity of the transmission with respect to the real or imaginary part of ϵ_r by substituting:

$$\frac{d\epsilon}{d\mathrm{Re}(\epsilon_r)} = \epsilon_0, \tag{4.48}$$

$$\frac{d\epsilon}{d\mathrm{Im}\left(\epsilon_r\right)} = j\epsilon_0, \tag{4.49}$$

into Eq. 4.33, respectively. This leads to the following two sensitivity formulas:

$$\frac{dT}{d\mathrm{Re}\left(\epsilon_r\right)} = -\frac{\omega\epsilon_0}{2P_0}\mathrm{Re}\left(\frac{jA_{21}^*}{A_1^{\mathrm{inc}}}\iiint_{V_C}\mathbf{E}_1\cdot\mathbf{E}_1^f dv\right), \tag{4.50}$$

$$\frac{dT}{d\mathrm{Im}\left(\epsilon_r\right)} = \frac{\omega\epsilon_0}{2P_0}\mathrm{Re}\left(\frac{A_{21}^*}{A_1^{\mathrm{inc}}}\iiint_{V_C}\mathbf{E}_1\cdot\mathbf{E}_1^f dv\right). \tag{4.51}$$

4.3 Numerical implementation

In this section, we present some examples of the application of the proposed method to find the sensitivity of the transmission with respect to the dielectric permittivity of the active material of the structure. To confirm the results obtained by the proposed formula, we have compared them with the results obtained using the direct approach. The numerical method which we use is a full-wave finite-difference frequency-domain (FDFD) simulation of the device [70, 50]. This method allows us to directly use experimental data for the frequency-dependent dielectric constant of metals such as silver [44], including both the real and imaginary parts, with no approximation. Perfectly matched layer (PML) absorbing boundary conditions are used at all boundaries of the simulation domain [45, 71].

4.3.1 2D example

The first example which is being considered here is a 2D plasmonic switch consisting of a multisection cavity between two resonators (two MDM stubs). The structure is symmetric with respect to a vertical mirror plane which bisects the middle section of the cavity (Figure 4.3). The waveguide and resonators are filled with an active material with relative dielectric permitivity of $\epsilon_c = \epsilon_{cr} + j\epsilon_{ci}$, which can be a complex number. For the direct approach the

on state of the switch corresponds to $\epsilon_c = 4.804$. If we want to find the sensitivity with respect to the real part of ϵ_c we will change it to $\epsilon_c = 4.904$ in the cavity region for the *on* state. If we want to find the sensitivity with respect to the imaginary part of ϵ_c, we will change it to $\epsilon_c = 4.804 + i0.01$ in the cavity region for the *off* state.

For a fixed structure with:

$$d_s = 172 \text{ nm},$$

$$d_c = 150 \text{ nm},$$

we have investigated the sensitivity of the transmission on the dielectric permittivity of the active material inside the cavity using both the proposed equations (Eq. 4.50 and Eq. 4.51), as well as the Direct Approach (DA) for different wavelengths. We first consider a lossless structure. In other words, the metal is assumed to be lossless in these simulations.

Since the dielectric permittivity is complex, the sensitivity is calculated for two different cases. First, we assume that the dielectric permittivity of the active material for both the *on* and *off* states is a real number (no loss in the cavity). We first use the proposed sensitivity formula to find the sensitivity of the transmission with respect to the real part of the relative dielectric permittivity inside the cavity:

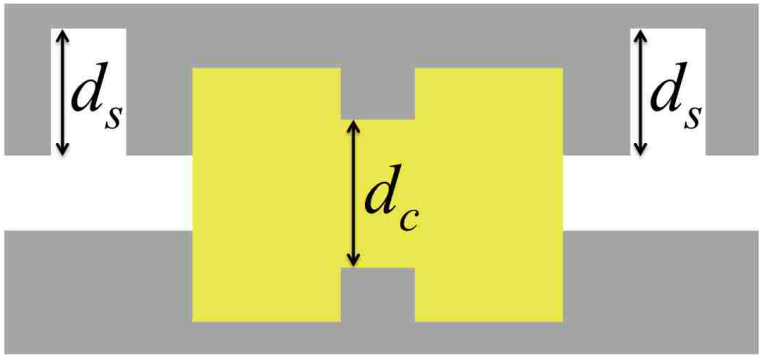

Figure 4.3: Schematic of an absorption switch consisting of a MDM plasmonic waveguide coupled to a resonator. The resonator is formed by a cavity comprising of multiple sections of varying widths sandwiched between two MDM stubs.

$$\frac{dT}{d\mathrm{Re}\left(\epsilon_r\right)} = -\frac{\omega\epsilon_0}{2P_0}\mathrm{Re}\left(\frac{jA_{21}^*}{A_1^{\mathrm{inc}}}\iiint_{V_C}\mathbf{E}_1\cdot\mathbf{E}_1^f dv\right), \tag{4.52}$$

and then we compare it with the direct approach results (Figure 4.4). In the direct approach, we directly calculate the sensitivity by approximating the derivative with a finite difference:

$$D_c = \frac{dT}{d\mathrm{Re}\left(\epsilon_c\right)} \simeq \frac{\Delta T}{\Delta\mathrm{Re}\left(\epsilon_c\right)} = \frac{T\left(\epsilon_c = \epsilon_{cr} + \Delta\epsilon_{cr} + j\epsilon_{ci}\right) - T\left(\epsilon_c = \epsilon_{cr} + j\epsilon_{ci}\right)}{\Delta\epsilon_{cr}}. \tag{4.53}$$

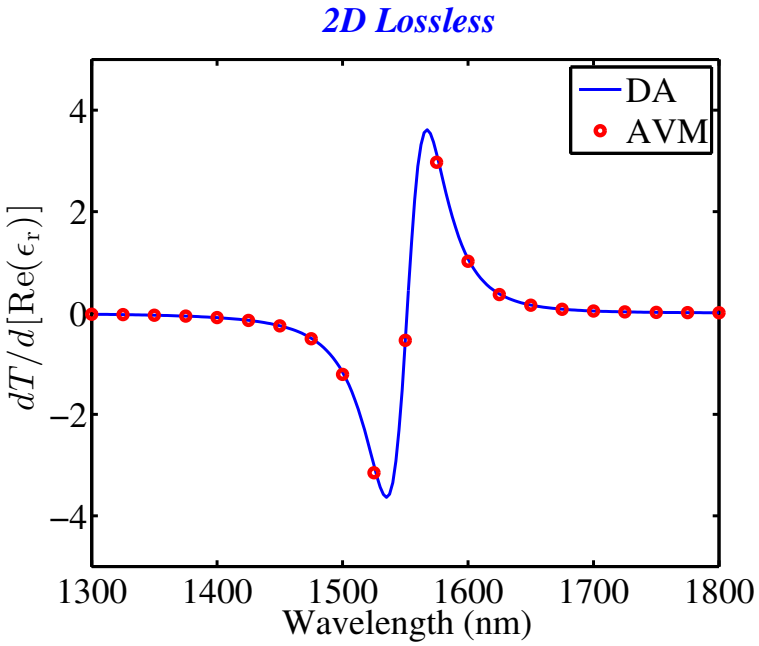

Figure 4.4: Sensitivity of the transmission with respect to the real part of the relative dielectric permittivity inside the cavity of the structure shown in Figure 4.3 in the absence of loss in the metal. Results are calculated using the direct approach (DA) (Eq. 4.53), and the adjoint variable method (AVM) (Eq. 4.52).

We also find the sensitivity of the transmission with respect to the imaginary part of the relative dielectric permittivity inside the cavity (Figure 4.5). The proposed sensitivity formula for this case is:

$$\frac{dT}{d\mathrm{Im}\left(\epsilon_r\right)} = \frac{\omega\epsilon_0}{2P_0}\mathrm{Re}\left(\frac{A_{21}^*}{A_1^{\mathrm{inc}}}\iiint_{V_C}\mathbf{E}_1\cdot\mathbf{E}_1^f dv\right). \tag{4.54}$$

As before, in direct approach we directly calculate the sensitivity by approximating the derivative with a finite difference:

$$D_c = \frac{dT}{d\mathrm{Im}\left(\epsilon_c\right)} \simeq \frac{\Delta T}{\Delta\mathrm{Im}\left(\epsilon_c\right)} = \frac{T\left[\epsilon_c = \epsilon_{cr} + j\left(\epsilon_{ci} + \Delta\epsilon_{ci}\right)\right] - T\left(\epsilon_c = \epsilon_{cr} + j\epsilon_{ci}\right)}{\Delta\epsilon_{ci}}. \tag{4.55}$$

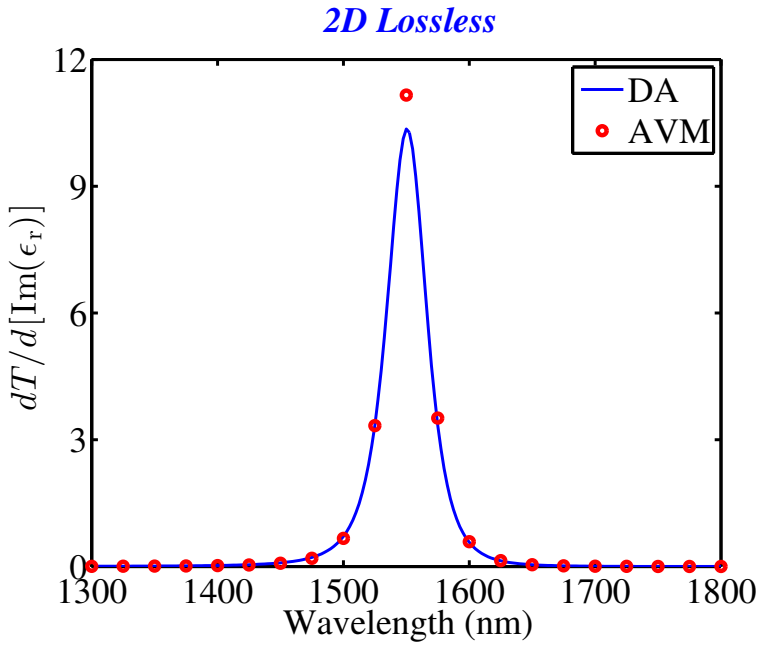

Figure 4.5: Sensitivity of the transmission with respect to the imaginary part of the relative dielectric permittivity inside the cavity of the structure shown in Figure 4.3 in the absence of loss in the metal. Results are calculated using the direct approach (DA) (Eq. 4.55), and the adjoint variable method (AVM) (Eq. 4.54).

These calculations are repeated for a lossy structure (including the material loss in the metal in the simulations) and the results are shown in Figures 4.6 and 4.7.

The sensitivities obtained by the proposed formula are in excellent agreement with the ones obtained by the direct approach. The small differences between the two sets of results

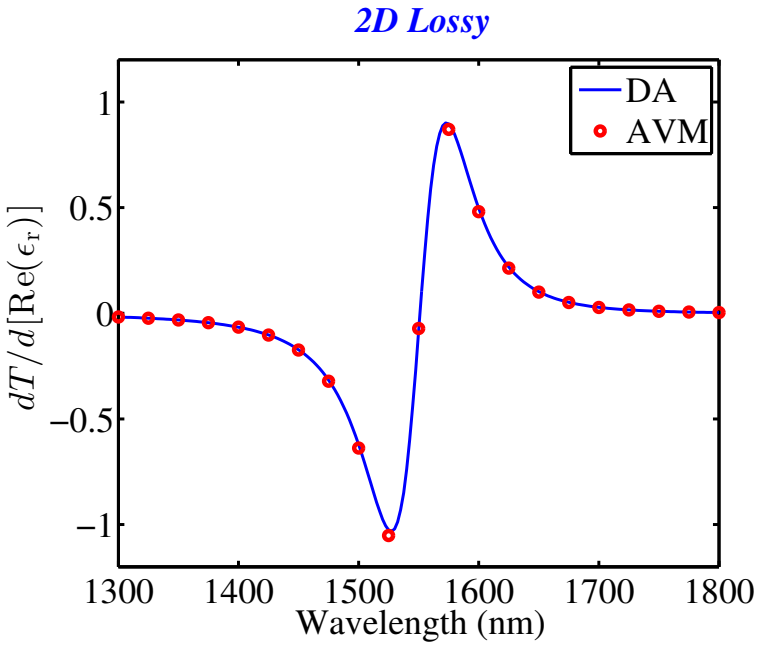

Figure 4.6: Sensitivity of the transmission with respect to the real part of the relative dielectric permittivity inside the cavity of the structure shown in Figure 4.3. Results are calculated using the direct approach (DA) (Eq. 4.53), and the adjoint variable method (AVM) (Eq. 4.52).

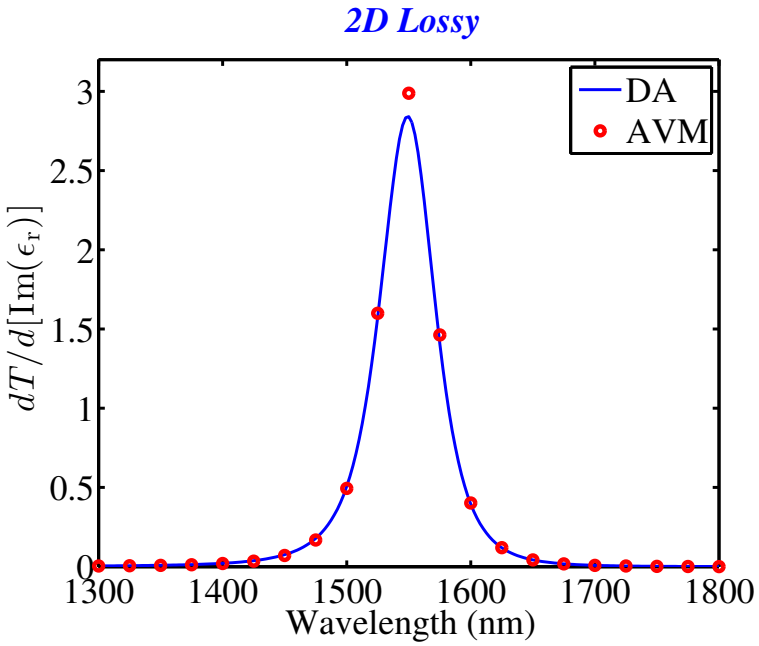

Figure 4.7: Sensitivity of the transmission with respect to the imaginary part of the relative dielectric permittivity inside the cavity of the structure shown in Figure 4.3. Results are calculated using the direct approach (DA) (Eq. 4.55), and the adjoint variable method (AVM) (Eq. 4.54).

can be attributed to errors in the numerical integration. We observe that at $\lambda = 1550$ nm, which is the resonance wavelength of the considered structure, the sensitivity of the transmission with respect to the real part of the relative dielectric permittivity is almost zero. This will be investigated in more detail below.

In addition, the sensitivity of the transmission with respect to the real and imaginary parts of the relative dielectric permittivity, when the width of the middle section of the cavity d_c is varied for a fixed wavelength $\lambda = 1550$ nm, are calculated and shown in Figures 4.8 and 4.9. As before, we observe excellent agreement with the ones obtained by the direct approach.

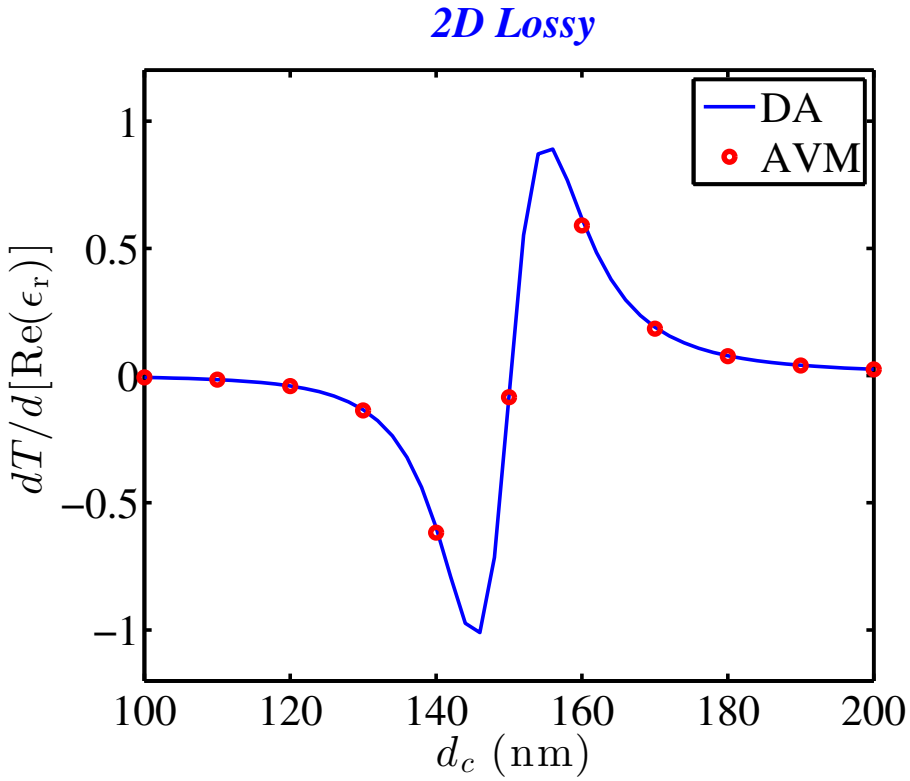

Figure 4.8: Sensitivity of the transmission with respect to the real part of the relative dielectric permittivity inside the cavity of the structure shown in Figure 4.3. Results are calculated using the direct approach (DA) (Eq. 4.53), and the adjoint variable method (AVM) (Eq. 4.52).

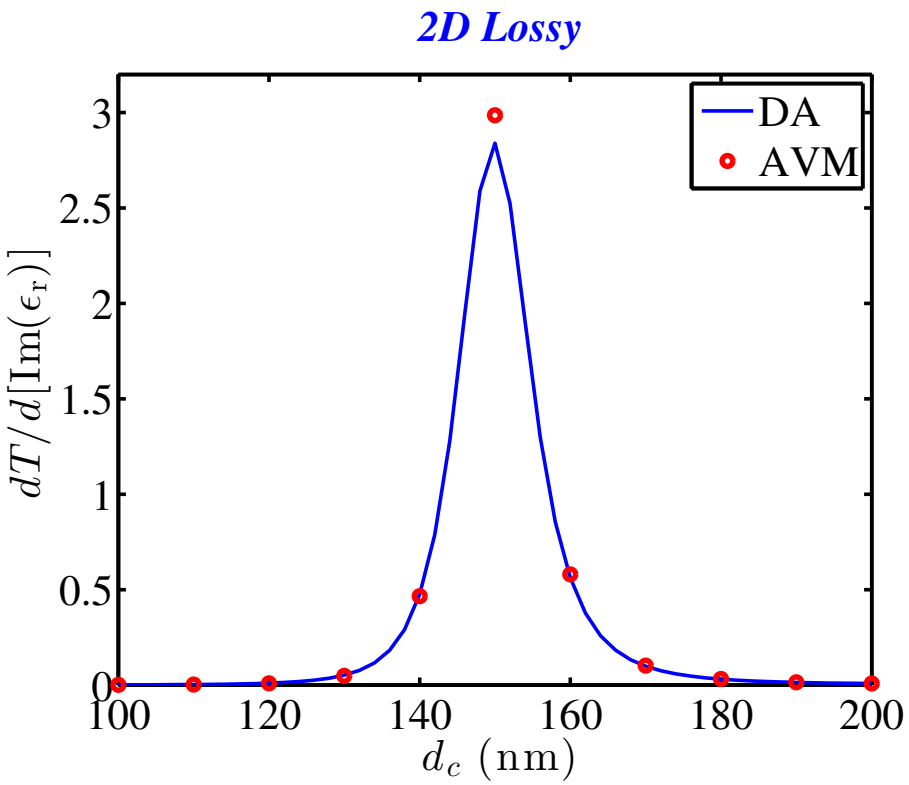

Figure 4.9: Sensitivity of the transmission with respect to the imaginary part of the relative dielectric permittivity inside the cavity of the structure shown in Figure 4.3. Results are calculated using the direct approach (DA) (Eq. 4.55), and the adjoint variable method (AVM) (Eq. 4.54).

4.3.2 Sensitivity at resonance

The two-port device shown in Figure 4.10 is assumed to be lossless and symmetric. The propagation direction is z and the lines at $z = z_1$ and $z = z_4$ correspond to the input and output ports respectively. We then have:

$$\arg\left[E_1^{\mathrm{inc}}(x, y, z = z_1)\right] = \arg\left[E_1^{\mathrm{inc}}(x, y, z = z_2)\right] + \beta l, \tag{4.56}$$

$$\arg\left[E_1(x, y, z = z_4)\right] = \arg\left[E_1(x, y, z = z_3)\right] - \beta l, \tag{4.57}$$

where β is the propagation constant of the propagating mode in the input and output waveguides, and l is the distance between the input port $z = z_1$ and the beginning of the

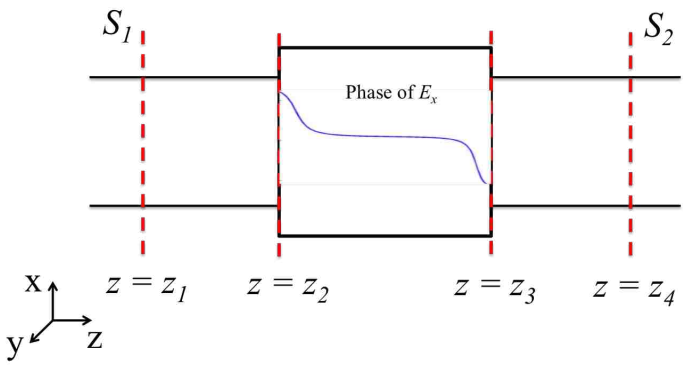

Figure 4.10: A symmetric two-port device. The blue curve shows the changes of the phase of E_x inside the cavity of Figure 4.3.

structure $z = z_2$, which is equal to the distance between the end of the structure $z = z_3$ and the output port $z = z_4$, because of the symmetry of the device. The proposed formula for the sensitivity with respect to the real part of the dielectric permittivity inside the cavity is:

$$\frac{dT}{d\mathrm{Re}\left(\epsilon_r\right)} = -\frac{\omega\epsilon_0}{2P_0}\mathrm{Re}\left(\frac{jA_{21}^*}{A_1^{\mathrm{inc}}}\iiint_{V_C}\mathbf{E}_1\cdot\mathbf{E}_1^f dv\right). \tag{4.58}$$

The phase of the term inside the real function can be written as the summation of three phases:

$$\arg\left(\frac{jA_{21}^*}{A_1^{\mathrm{inc}}}\iiint_{V_C}\mathbf{E}_1\cdot\mathbf{E}_1^f dv\right) = \arg\left(j\right) + \arg\left(\frac{jA_{21}^*}{A_1^{\mathrm{inc}}}\right) + \arg\left(\iiint_{V_S}\mathbf{E}_1\cdot\mathbf{E}_1^f dv\right)$$

$$= \arg\left(j\right) + \arg\left[\frac{jE_{x1}^*\left(x,y,z=z_4\right)}{E_{x1}^{\mathrm{inc}}\left(x,y,z=z_1\right)}\right] + \arg\left(\iiint_{V_S}\mathbf{E}_1\cdot\mathbf{E}_1^f dv\right). \tag{4.59}$$

The second term can be written as:

$$\arg\left[\frac{E_{x1}^*\left(x,y,z=z_4\right)}{E_{x1}^{\mathrm{inc}}\left(x,y,z=z_1\right)}\right] = -\arg\left[E_{x1}\left(x,y,z=z_4\right)\right] - \arg\left[E_{x1}^{\mathrm{inc}}\left(x,y,z=z_1\right)\right]. \tag{4.60}$$

Using Eq. 4.56 and Eq. 4.57 and the fact that at resonance there is almost no reflection we have:

$$\arg\left[\frac{E_{x1}^{*}\left(x,y,z=z_4\right)}{E_{x1}^{\text{inc}}\left(x,y,z=z_1\right)}\right]=-\arg\left[E_{x1}\left(x,y,z=z_3\right)\right]-\arg\left[E_{x1}\left(x,y,z=z_2\right)\right]. \qquad (4.61)$$

Before calculating the phase of the integral (third term), for the structure of Figure 4.3 we show the phase of electric field components E_x and E_z on resonance at three different lines $x = x_1 = 125$ nm, $x = x_2 = 175$ nm, and $x = x_3 = 225$ nm inside the cavity where the integral is being calculated (Figure 4.11). Also on each line we show the phases of $E_z E_z^f$ and $E_x E_x^f$ in Figures 4.14, 4.18, 4.22, and Figures 4.15, 4.19, 4.23, respectively.

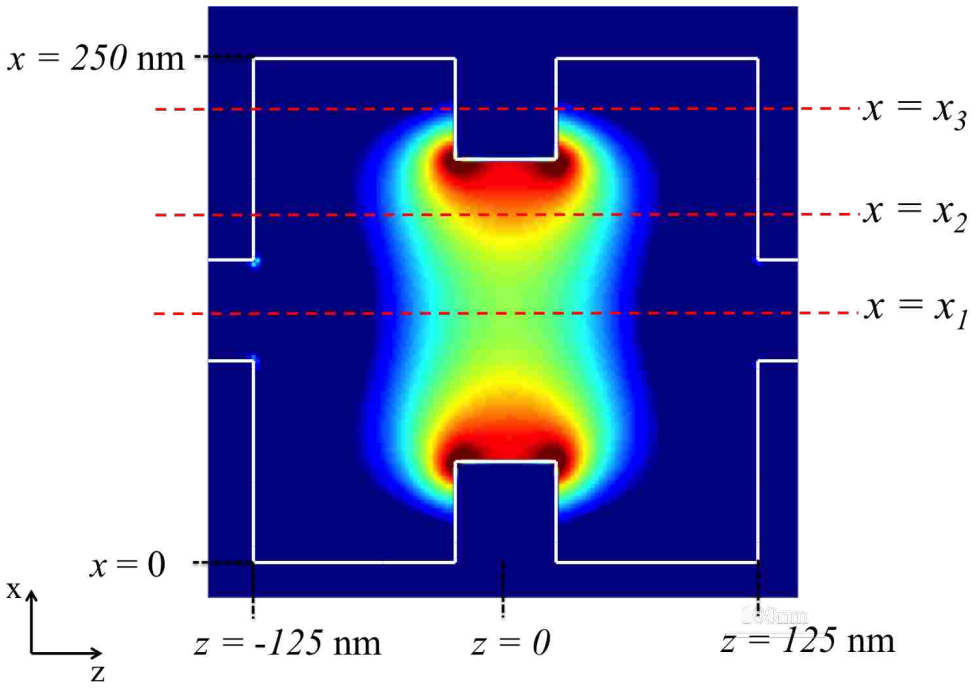

Figure 4.11: Profile of the electric field amplitude inside the cavity of the proposed switch of Figure 4.3 at the resonance wavelength of $\lambda_0 = 1.55$ μm.

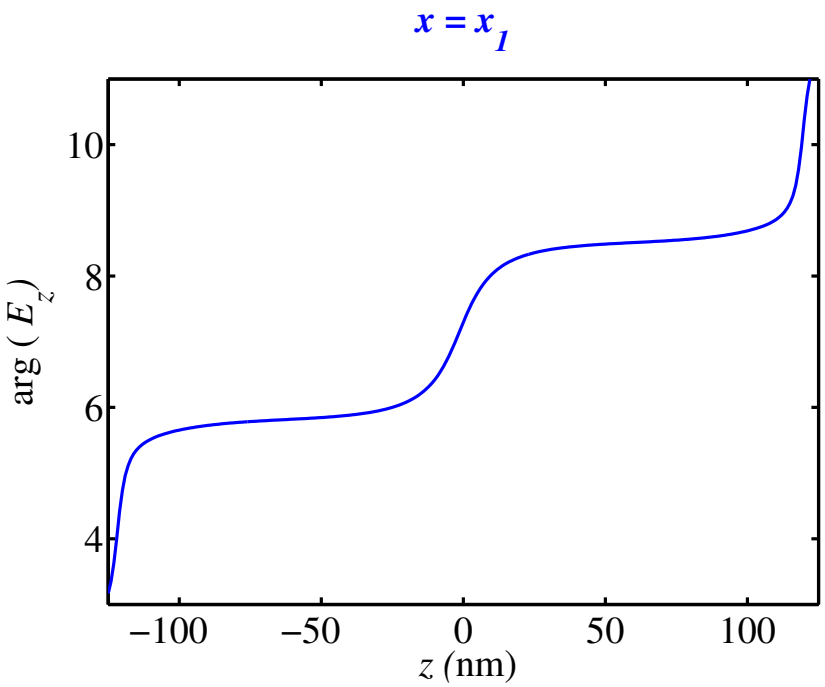

Figure 4.12: Phase of E_z inside the cavity at $x = x_1$ (Figure 4.11).

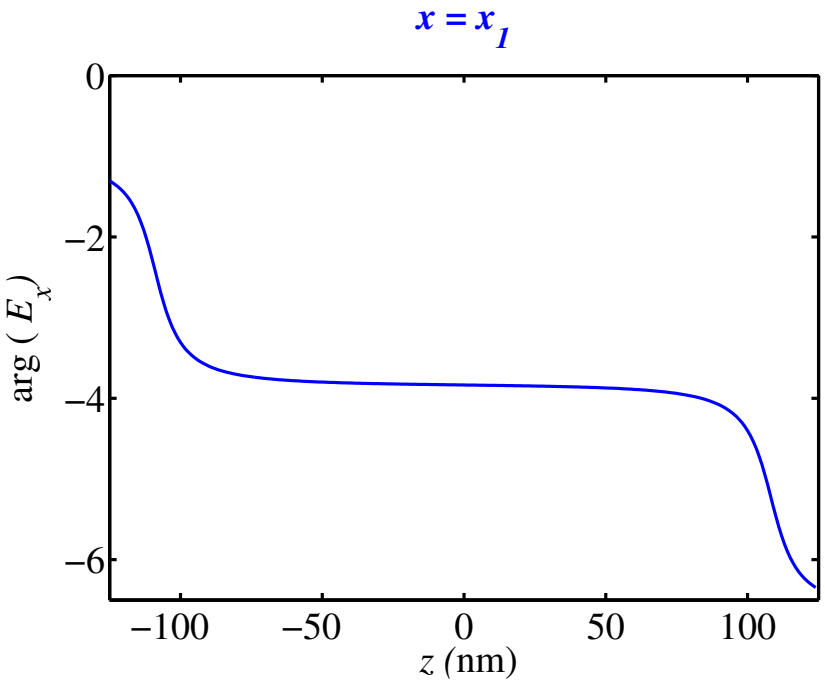

Figure 4.13: Phase of E_x inside the cavity at $x = x_1$ (Figure 4.11).

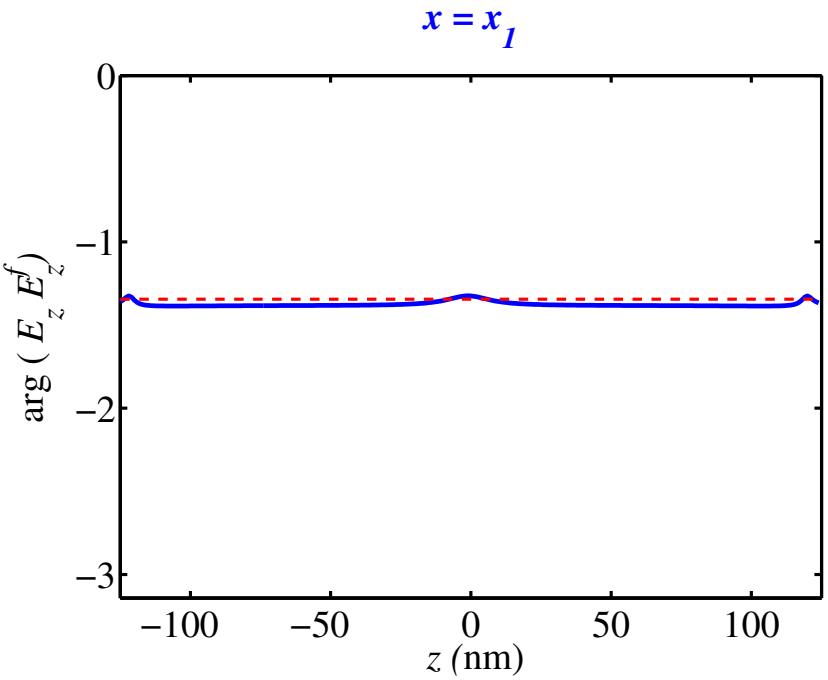

Figure 4.14: Phase of $E_z E_z^f$ inside the cavity at $x = x_1$ (Figure 4.11). The dashed red line is showing $\arg\left[E_{x1}\left(z = z_3\right)\right] + \arg\left[E_{x1}\left(z = z_2\right)\right]$.

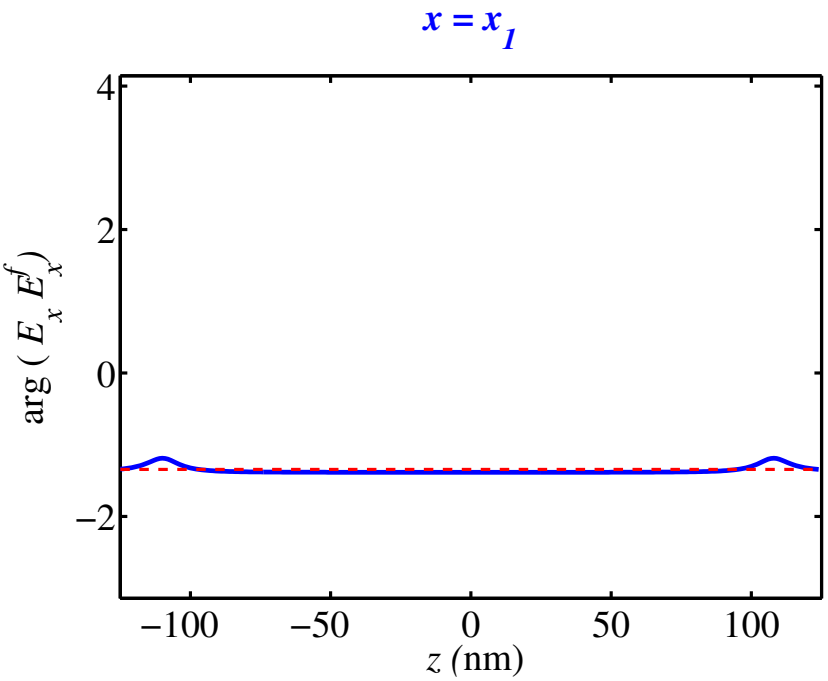

Figure 4.15: Phase of $E_x E_x^f$ inside the cavity at $x = x_1$ (Figure 4.11). The dashed red line is showing $\arg\left[E_{x1}\left(z = z_3\right)\right] + \arg\left[E_{x1}\left(z = z_2\right)\right]$.

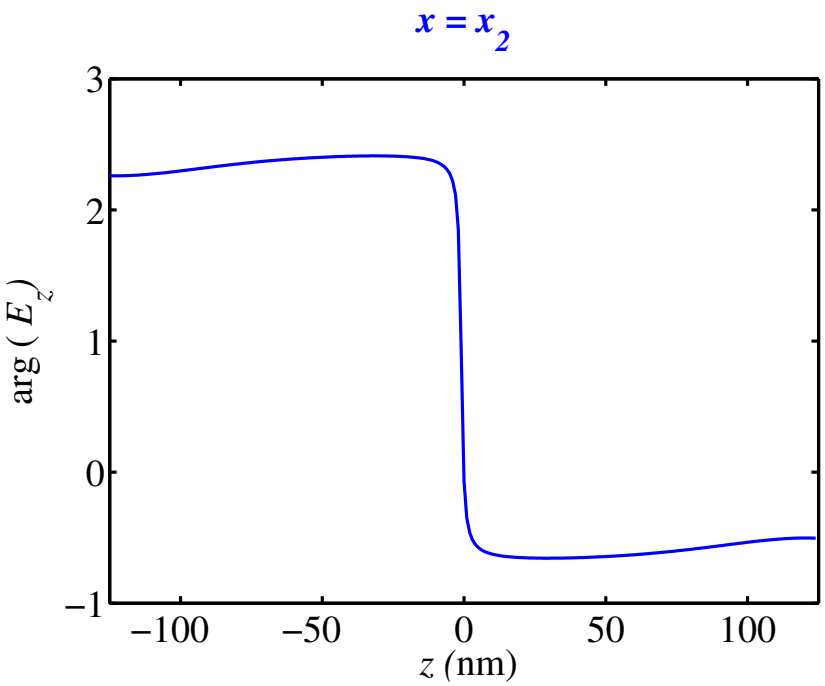

Figure 4.16: Phase of E_z inside the cavity at $x = x_2$ (Figure 4.11).

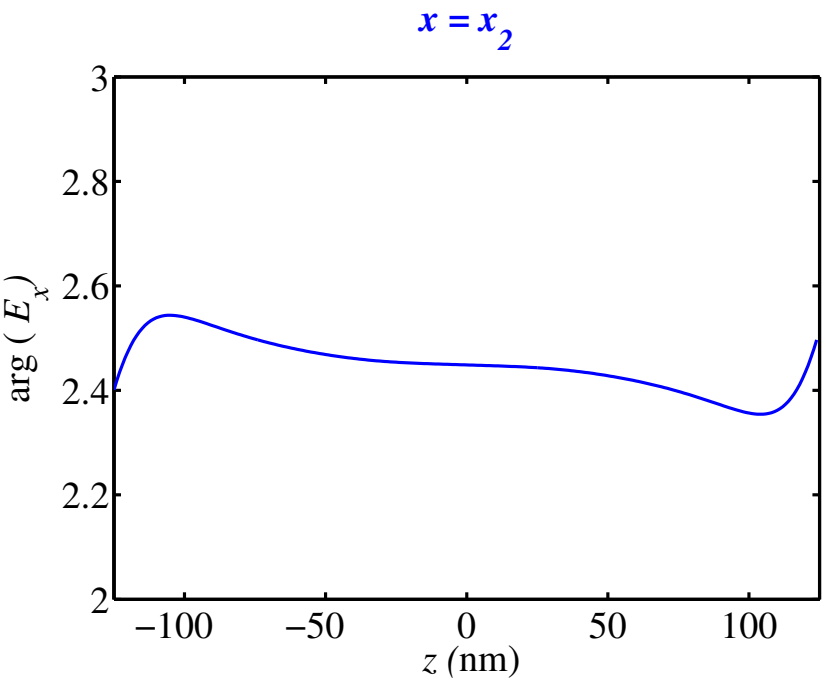

Figure 4.17: Phase of E_x inside the cavity at $x = x_2$ (Figure 4.11).

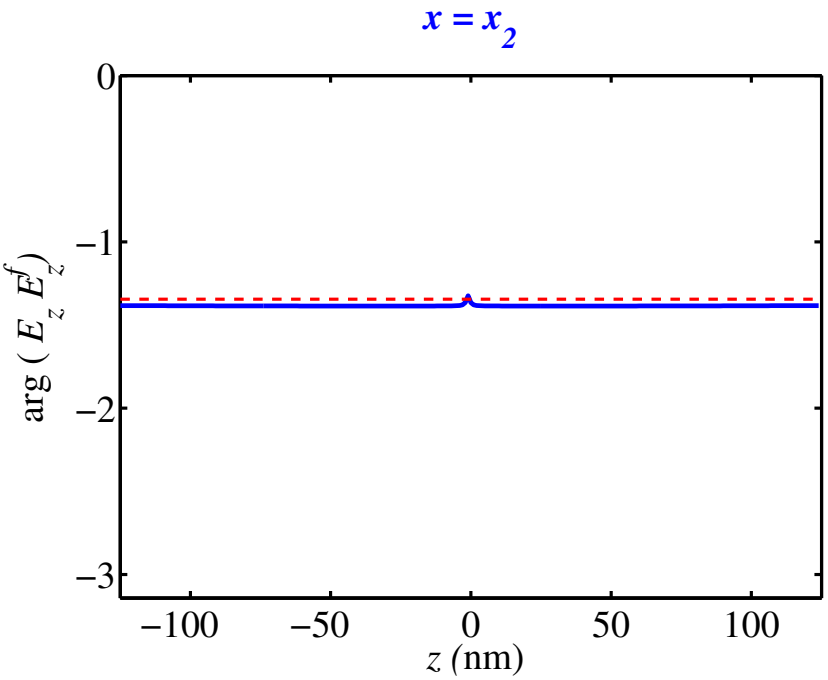

Figure 4.18: Phase of $E_z E_z^f$ inside the cavity at $x = x_2$ (Figure 4.11). The dashed red line is showing $\arg\left[E_{x1}\left(z = z_3\right)\right] + \arg\left[E_{x1}\left(z = z_2\right)\right]$.

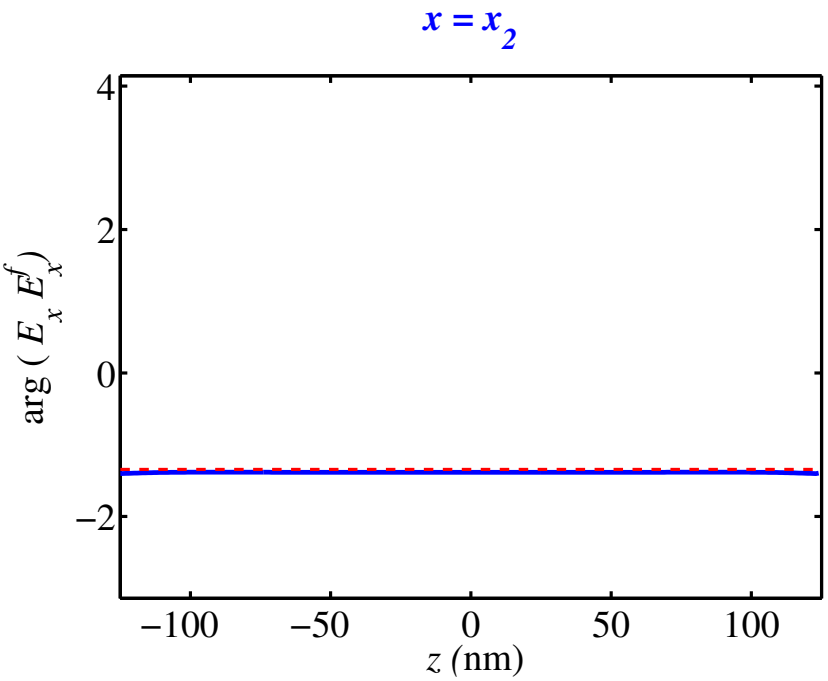

Figure 4.19: Phase of $E_x E_x^f$ inside the cavity at $x = x_2$ (Figure 4.11). The dashed red line is showing $\arg\left[E_{x1}\left(z = z_3\right)\right] + \arg\left[E_{x1}\left(z = z_2\right)\right]$.

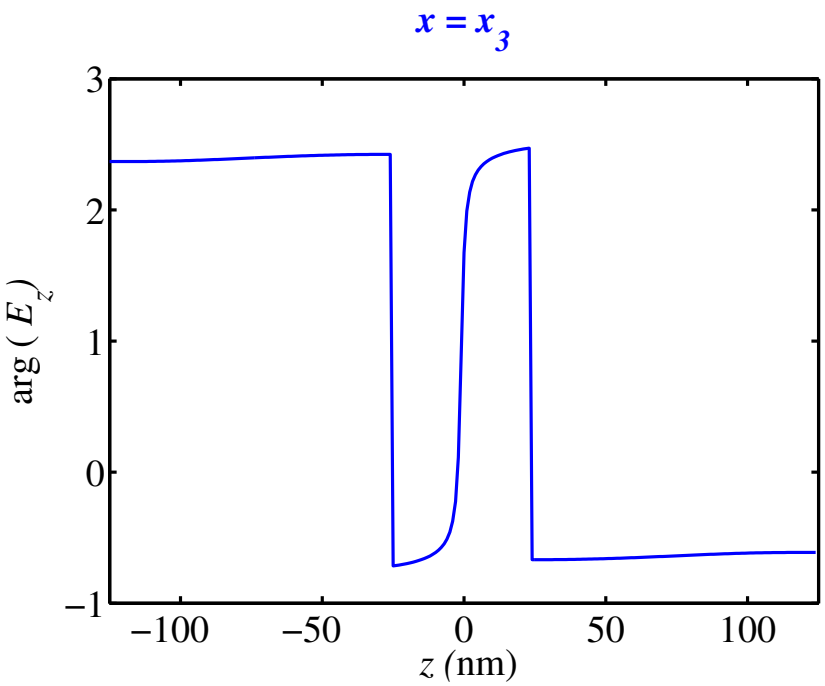

Figure 4.20: Phase of E_z inside the cavity at $x = x_3$ (Figure 4.11).

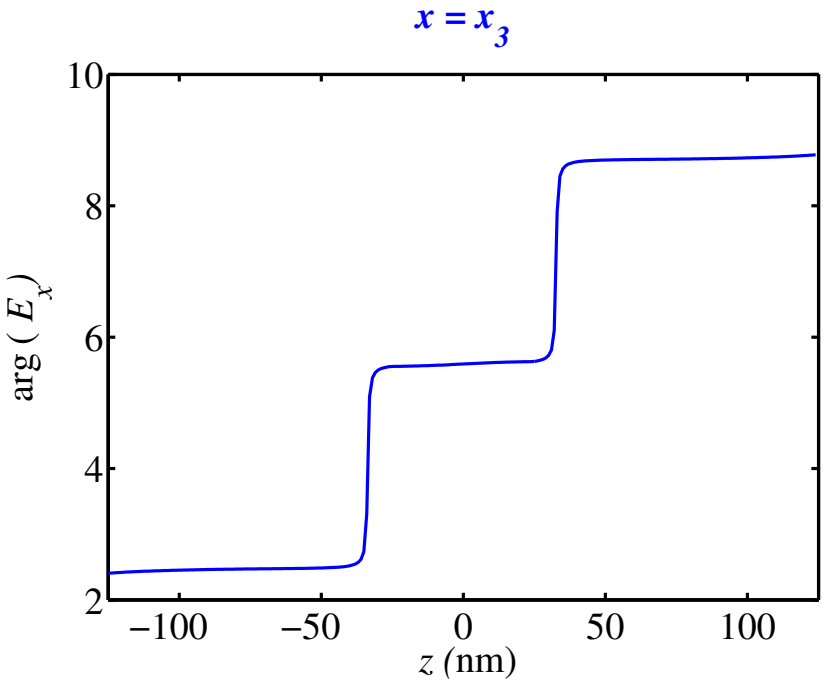

Figure 4.21: Phase of E_x inside the cavity at $x = x_3$ (Figure 4.11).

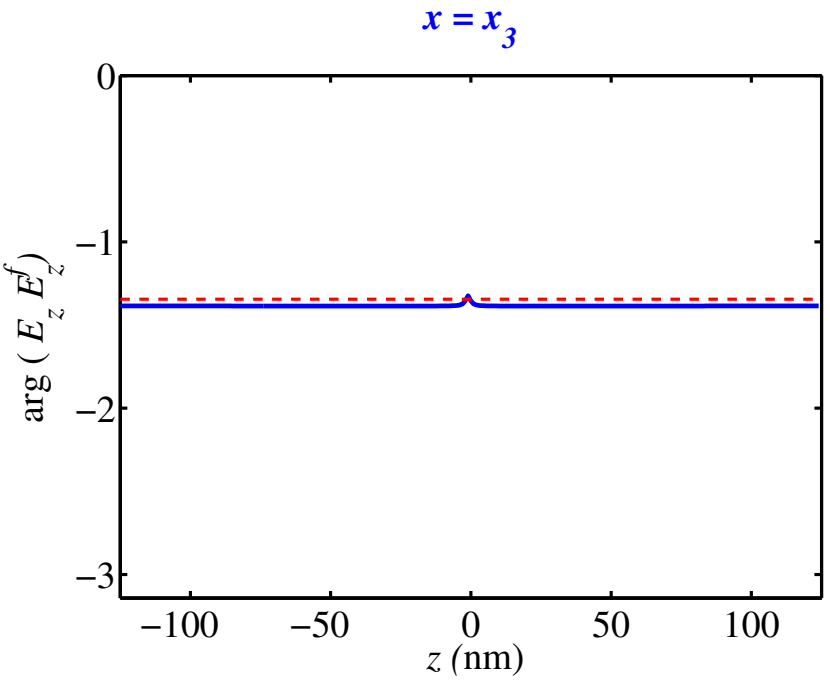

Figure 4.22: Phase of $E_z E_z^f$ inside the cavity at $x = x_3$ (Figure 4.11). The dashed red line is showing $\arg\left[E_{x1}\left(z = z_3\right)\right] + \arg\left[E_{x1}\left(z = z_2\right)\right]$.

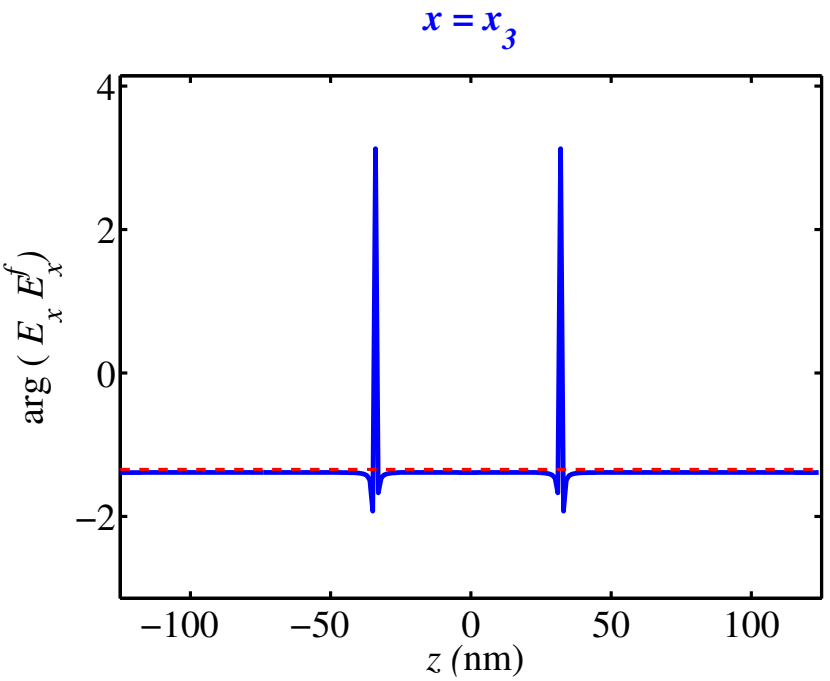

Figure 4.23: Phase of $E_x E_x^f$ inside the cavity at $x = x_3$ (Figure 4.11). The dashed red line is showing $\arg\left[E_{x1}\left(z = z_3\right)\right] + \arg\left[E_{x1}\left(z = z_2\right)\right]$.

We observe that, because of the symmetry of the structure, the changes of phase of the electric field components are almost the same as we move away from each side of the cavity towards the middle of it. This leads to a constant phase for the product of the electric field and its "flipped" field. This constant ϕ_0 is equal to:

$$\phi_0 = 2 \arg \left[E_{x1} \left(z = 0 \right) \right]. \tag{4.62}$$

Thus, the phase of the third term of Eq. 4.59, which is the integral of $E_x E_x^f$ and $E_z E_z^f$ over the cavity, would be:

$$\arg \left(\iiint_{V_S} \mathbf{E}_1 \cdot \mathbf{E}_1^f dv \right) \approx 2 \arg \left[E_{x1} \left(z = 0 \right) \right]. \tag{4.63}$$

In Figures 4.14, 4.15, 4.18, 4.19, 4.22, and 4.23 the dashed red line is showing $\{\arg \left[E_{x1} \left(z = z_3 \right) \right] + \arg \left[E_{x1} \left(z = z_2 \right) \right]\}$. Also because of the symmetry we have:

$$\arg \left(E_{x1} \left(x, y, z = z_3 \right) \right) + \arg \left(E_{x1} \left(x, y, z = z_2 \right) \right) = 2 \arg \left[E_{x1} \left(z = 0 \right) \right]. \tag{4.64}$$

Thus, from Eq. 4.61 and Eq. 4.63 we can conclude that:

$$\arg \left(\frac{A_{21}^*}{A_1^{\text{inc}}} \right) \approx - \arg \left(\iiint_{V_S} \mathbf{E}_1 \cdot \mathbf{E}_1^f dv \right). \tag{4.65}$$

At the end what remains as the phase of the argument of the real function in the sensitivity formula is only $\pi/2$:

$$\arg \left(\frac{j A_{21}^*}{A_1^{\text{inc}}} \iiint_{V_C} \mathbf{E}_1 \cdot \mathbf{E}_1^f dv \right) \approx \arg \left(j \right) = \pi/2, \tag{4.66}$$

meaning the whole argument is an imaginary number, so the real part of it would be zero, and correspondingly the sensitivity of the transmission with respect to the real part of the dielectric permittivity inside the cavity would be zero on resonance.

4.3.3 3D example

The next example which is being considered is a Fabry-Perot absorption switch based on a coaxial plasmonic waveguide (Figure 4.24). Figure 4.25 shows the top view schematic at $z = 0$ of the structure and Figure 4.26 shows the cross section of the proposed coaxial waveguide used for the switch.

Two stub resonators are used as the mirrors at the two sides of the cavity. The metal used is silver, and the space between the metallic parts is filled with silica. The structures are placed on top of a silicon substrate. The waveguide and resonators are filled with an active material with refractive index $n = 1.5$. If the inner and outer metals at the end of the stubs are connected (Figures 4.27 and 4.28), the stub is short-circuited. Otherwise, it is open-circuited (Figures 4.29 and 4.30).

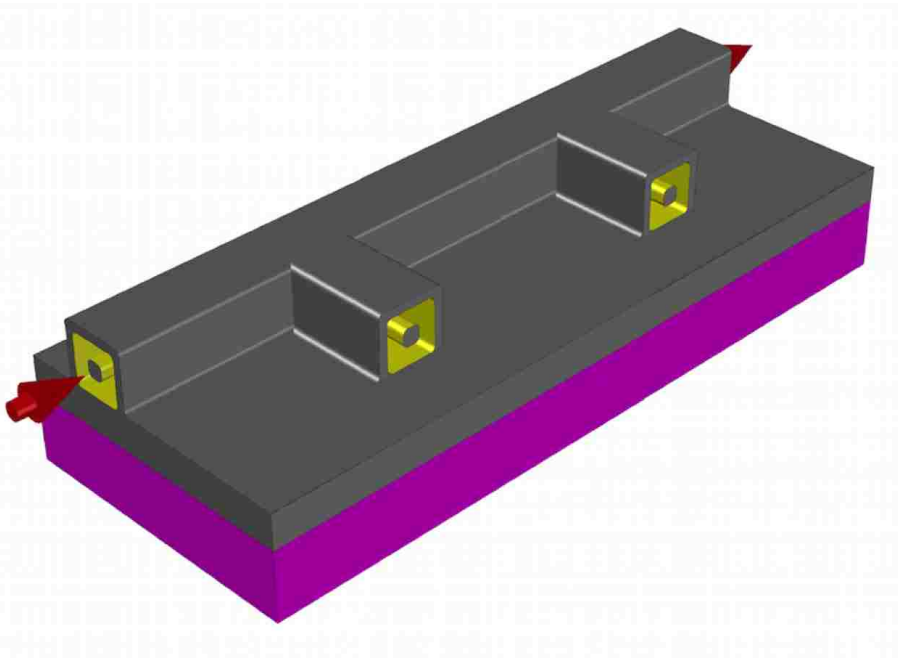

Figure 4.24: Schematic of a Fabry-Perot absorption switch based on coaxial plasmonic waveguide.

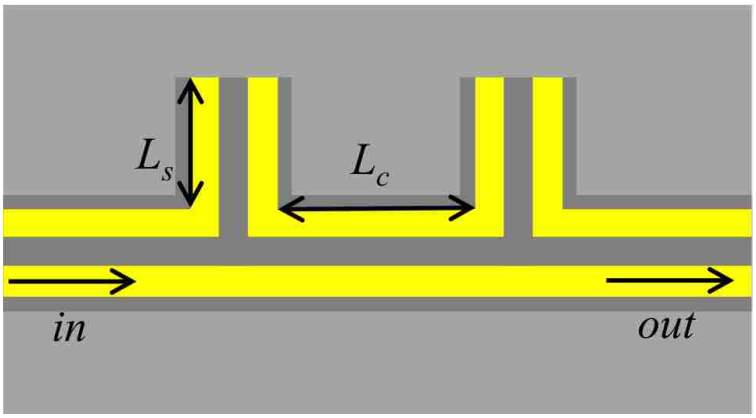

Figure 4.25: Top view schematic at $z = 0$ of a Fabry-Perot absorption switch based on coaxial plasmonic waveguide.

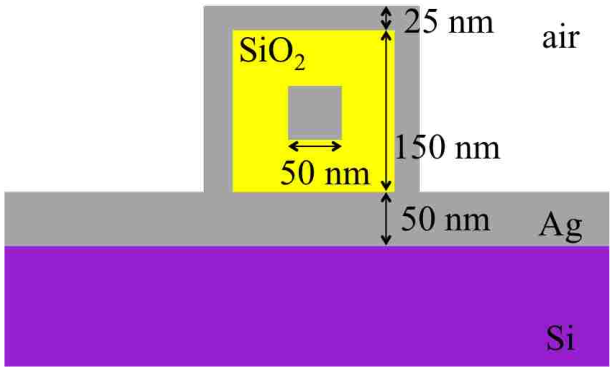

Figure 4.26: Cross section of the reference plasmonic coaxial waveguide.

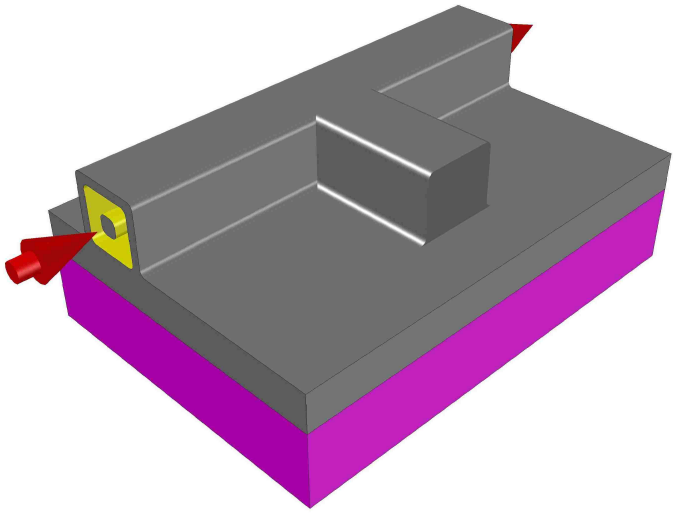

Figure 4.27: Schematic of a plasmonic coaxial waveguide side-coupled to a short-circuit coaxial stub resonator. The propagation direction of light is indicated by red arrows.

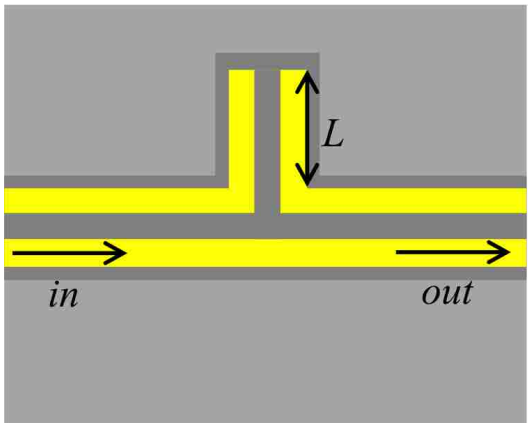

Figure 4.28: Top view schematic at $z = 0$ of a plasmonic coaxial waveguide side-coupled to a short-circuit coaxial stub resonator.

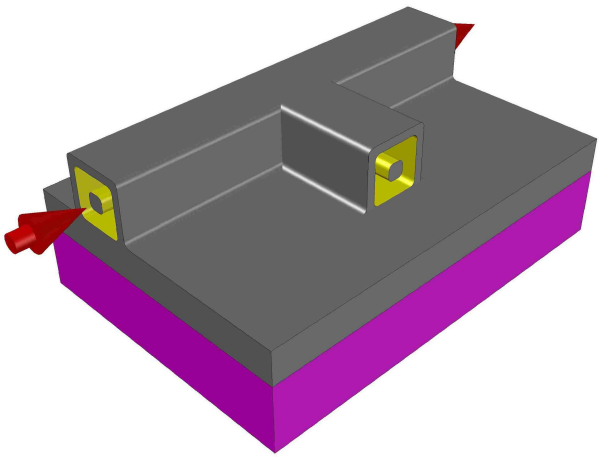

Figure 4.29: Schematic of a plasmonic coaxial waveguide side-coupled to an open-circuit coaxial stub resonator. The propagation direction of light is indicated by red arrows.

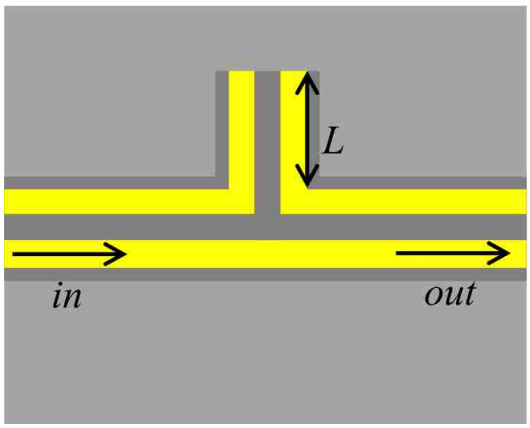

Figure 4.30: Top view schematic at $z = 0$ of a plasmonic coaxial waveguide side-coupled to an open-circuit coaxial stub resonator.

As we know, for a Fabry-Perot absorption switch most interaction between light and matter occurs when the two stubs are close to their resonance and act as mirrors. To find the approximate length for the stubs, we have first simulated a coaxial plasmonic waveguide coupled to a stub resonator using FD3D. Simulation was done twice for both short-circuited stubs (Figure 4.31) and open-circuited stubs (Figure 4.32).

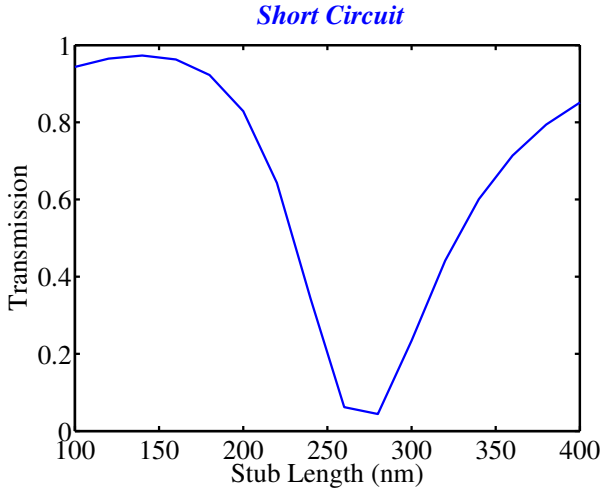

Figure 4.31: Transmission of a single short-circuit coaxial stub resonator as a function of the stub length L_s at $\lambda_0 = 1550$ nm. The other geometrical parameters of the structure are as shown in Figure 4.26.

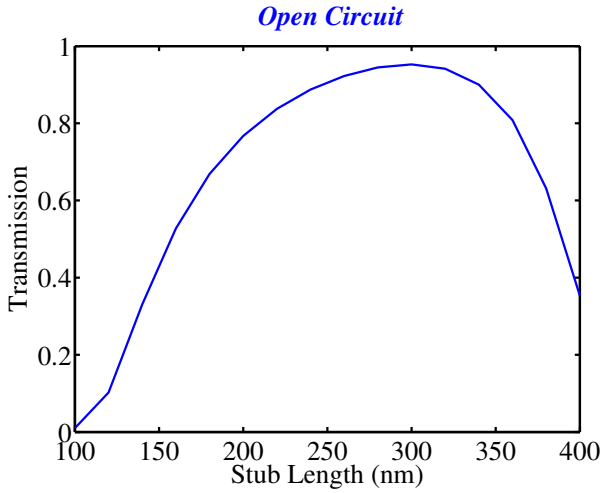

Figure 4.32: Transmission of a single open-circuit coaxial stub resonator as a function of the stub length L_s at $\lambda_0 = 1550$ nm. The other geometrical parameters of the structure are as shown in Figure 4.26.

As we expected the first resonant length is smaller for the open-circuit stub [84]. Thus in our proposed Fabry-Perot absorption switch two open-circuited stub resonators are used as mirrors at the two sides of the cavity. The waveguide and resonators are filled with an active material with refractive index $n = 1.5$. The refractive index of the cavity, between the two mirrors (stub resonators), is changed to $n = 1.5 + i0.05$ for the *off* state. The Modulation Depth is also calculated as before:

$$MD = \frac{T\,(on) - T\,(off)}{T\,(on)}. \tag{4.67}$$

Varying L_s and L_c we have found the transmission for both *on* state (Figure 4.33) and *off* state (Figure 4.34) and also modulation depth (Figure 4.35):

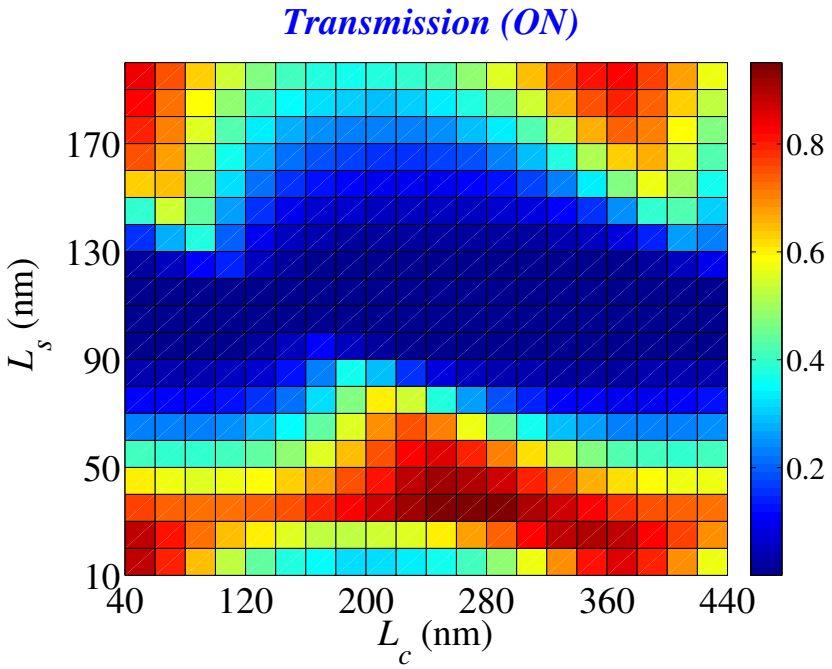

Figure 4.33: Transmission intensities of *on* state of the proposed Fabry-Perot absorption switch with two open-circuit stub resonators as functions of stub length L_s and the length of the cavity L_c at $\lambda_0 = 1550$ nm.

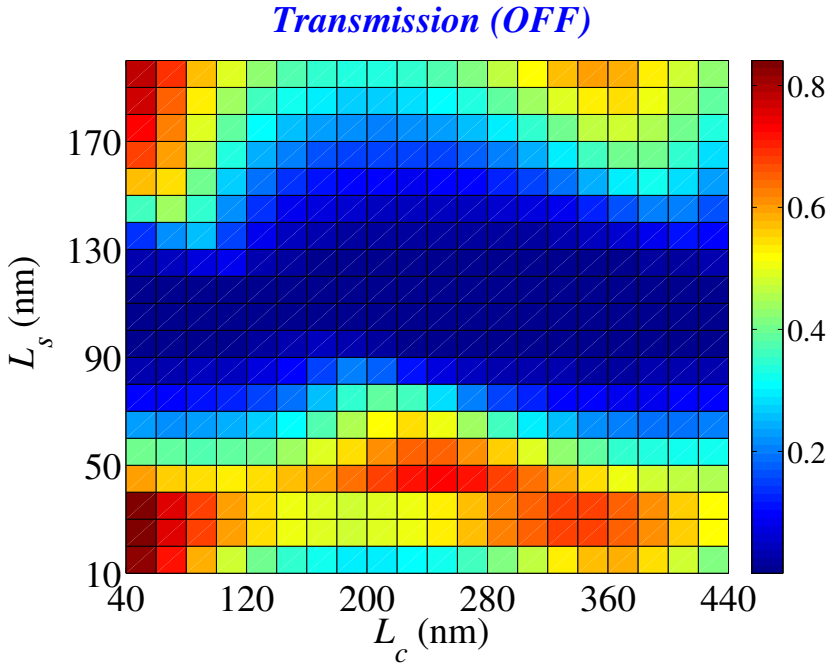

Figure 4.34: Transmission intensities of *off* state of the proposed Fabry-Perot absorption switch with two open-circuit stub resonators as functions of stub length L_s and the length of the cavity L_c at $\lambda_0 = 1550$ nm.

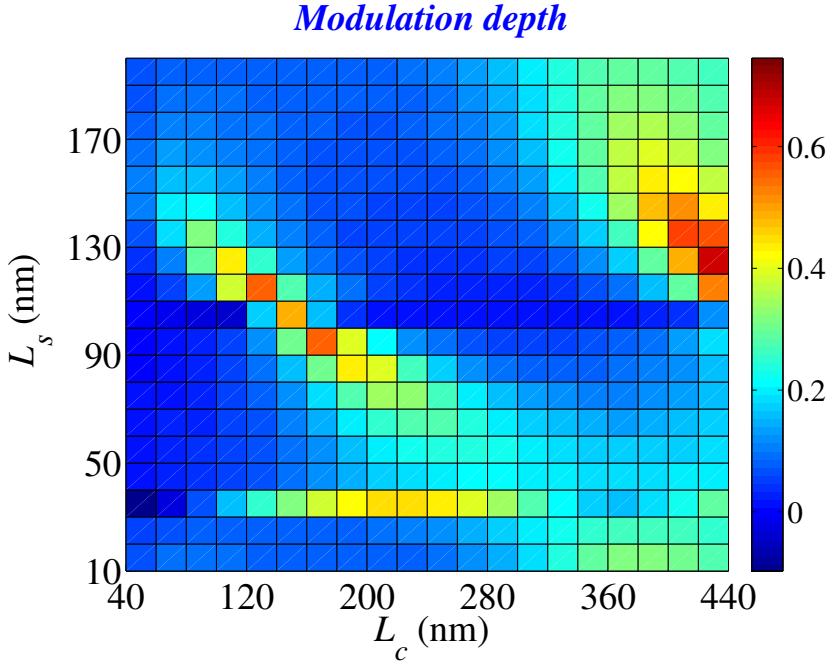

Figure 4.35: Modulation depth of the proposed Fabry-Perot absorption switch with two open-circuit stub resonators as functions of stub length L_s and the length of the cavity L_c at $\lambda_0 = 1550$ nm.

Considering transmission in the *on* state of more than 50% the maximum modulation depth MD is found for:

$$L_s = 150 \text{ nm},$$

$$L_c = 380 \text{ nm},$$

to be:

$$MD = 0.44.$$

The transmission spectra for both *on* and *off* states for the optimized switch are shown in Figures 4.36 and 4.37, while the modulation depth is shown in Figure 4.38 (solid lines). Also shown are the transmission and modulation depth spectra if the metal is lossless (dashed lines).

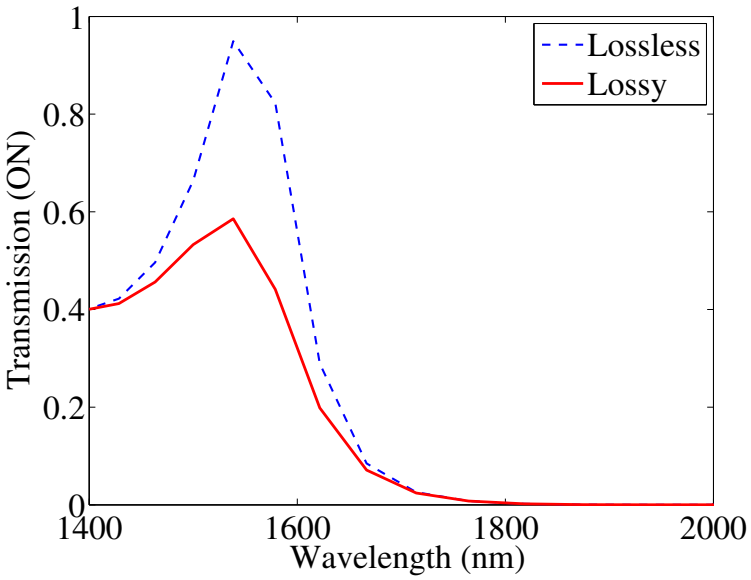

Figure 4.36: Transmission spectra T for the optimized proposed Fabry-Perot absorption switch of Figure 4.24 in the *on* state (solid line). Also shown are the transmission spectra if the metal is lossless (dashed line). Results are shown for $L_s = 150$ nm, $L_c = 380$ nm.

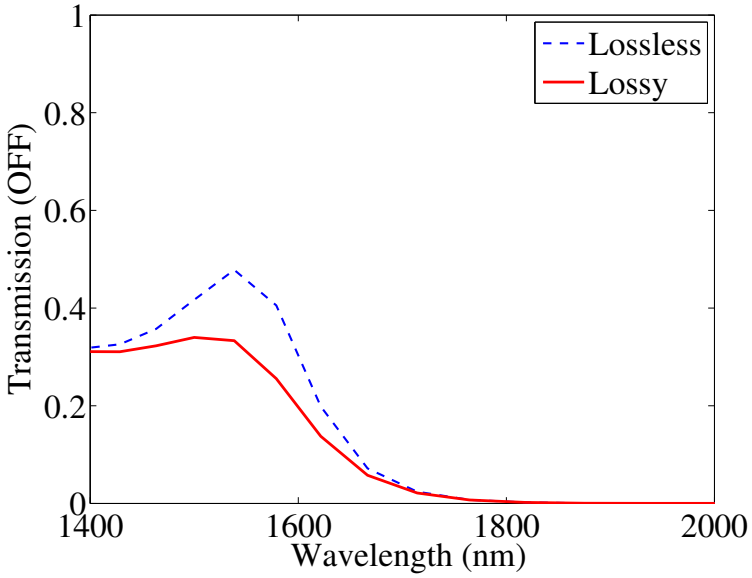

Figure 4.37: Transmission spectra T for the optimized proposed Fabry-Perot absorption switch of Figure 4.24 in the *off* state (solid line). Also shown are the transmission spectra if the metal is lossless (dashed line). Results are shown for $L_s = 150$ nm, $L_c = 380$ nm.

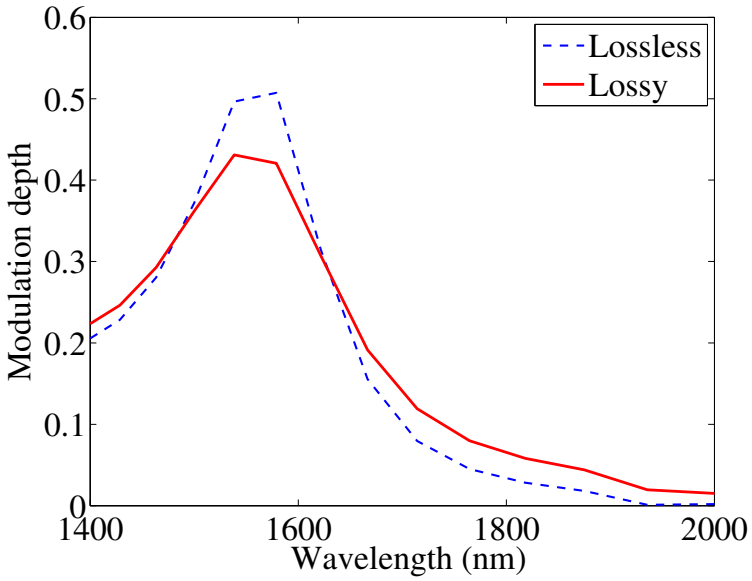

Figure 4.38: Modulation depth spectra MD for the optimized proposed Fabry-Perot absorption switch of Figure 4.24 (solid line).Also shown are the modulation depth spectra if the metal is lossless (dashed line). Results are shown for $L_s = 150$ nm, $L_c = 380$ nm.

The dominant electric and magnetic fields of the selected structure are shown in Figures 4.39 and 4.40, respectively.

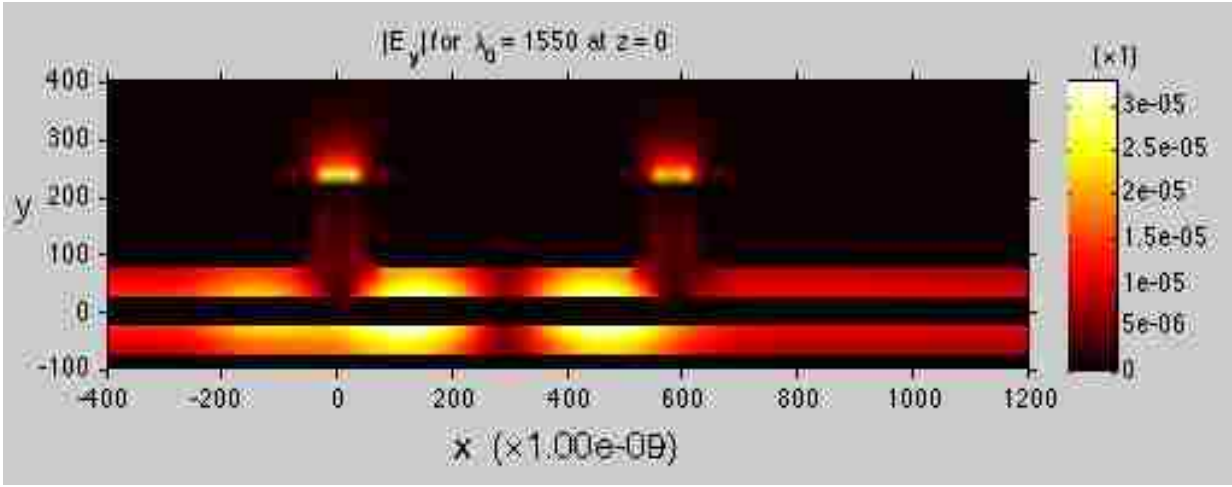

Figure 4.39: Amplitude of E_y of the optimized structure of Figure 4.24 (L_s = 150 nm, L_c = 380 nm) at $z = 0$ and $\lambda = 1550$ nm.

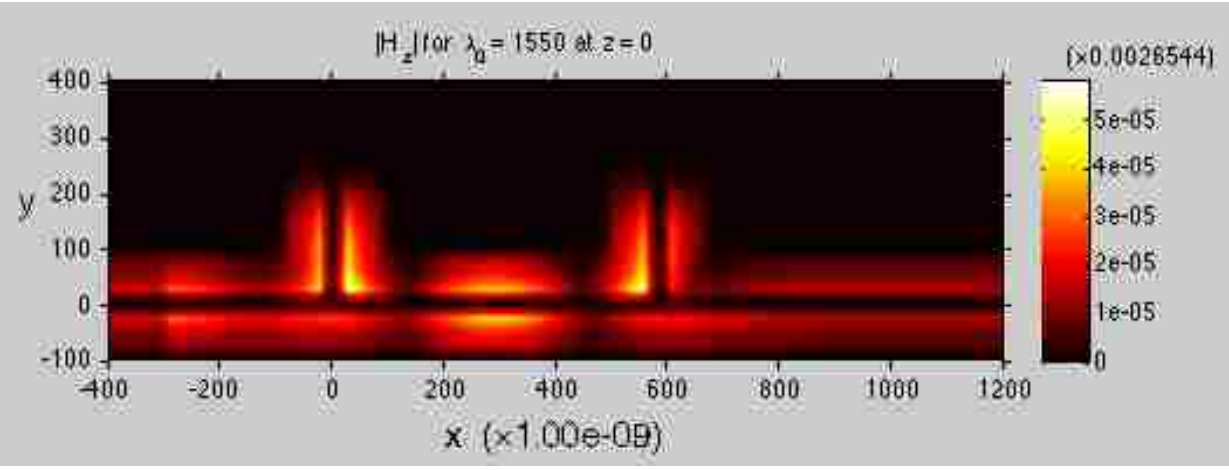

Figure 4.40: Amplitude of H_z of the optimized structure of Figure 4.24 (L_s = 150 nm, L_c = 380 nm) at $z = 0$ and $\lambda = 1550$ nm.

As we mentioned before the modulation depth of the absorption switches is associated with the sensitivity of their transmission to the imaginary part of the dielectric constant of the active material, which is in turn directly related to the electric field energy in the cavity

region [50, 51, 52, 53]. The sensitivity can be calculated through the proposed sensitivity formula:

$$\frac{dT}{d\epsilon_r} = -\frac{\omega\epsilon_0}{2P_0}\mathrm{Re}\left(\frac{jA_{21}^*}{A_1^{\mathrm{inc}}}\iiint_{V_C}\mathbf{E}_1\cdot\mathbf{E}_1^f dv\right). \tag{4.68}$$

We have calculated the sensitivity of the transmission with respect to the real and imaginary parts of the permitivity of the active material in the cavity (between the stubs), when varying the length of the cavity. The length of the stubs is fixed at $L_s = 150$ nm. The results are obtained by the AVM method and compared with the ones of the direct approach. As it is shown, the AVM results are in excellent agreement with the direct approach ones (Figures 4.41 and 4.42).

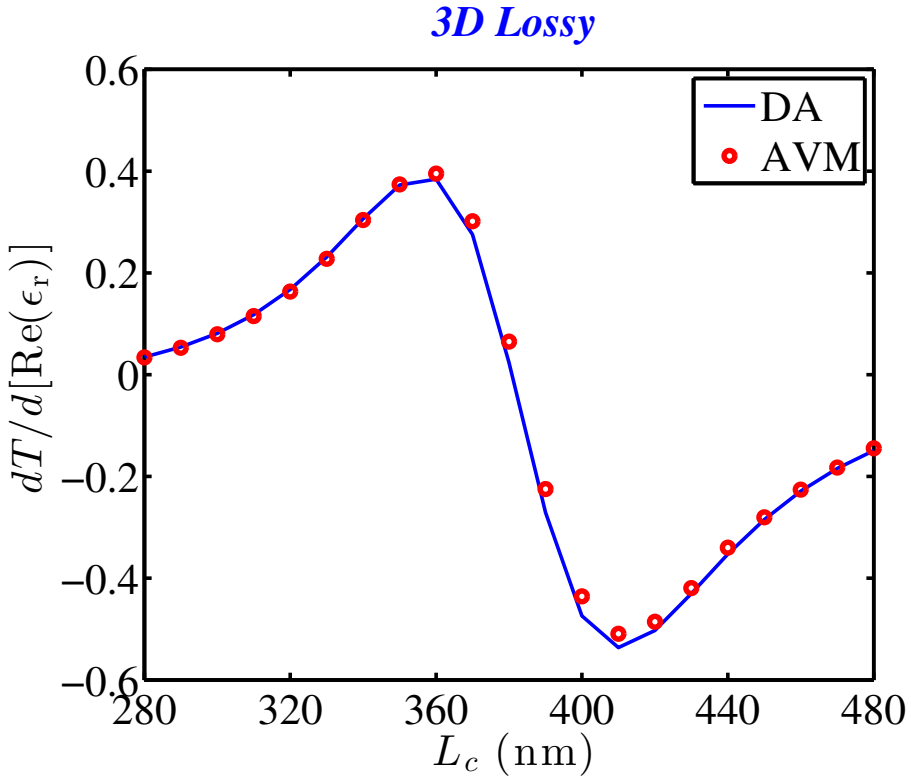

Figure 4.41: Sensitivity of the transmission with respect to the real part of the relative dielectric permittivity inside the cavity of the structure shown in Figure 4.24. Results are calculated using the direct approach (DA) (Eq. 4.53), and the adjoint variable method (AVM) (Eq. 4.52).

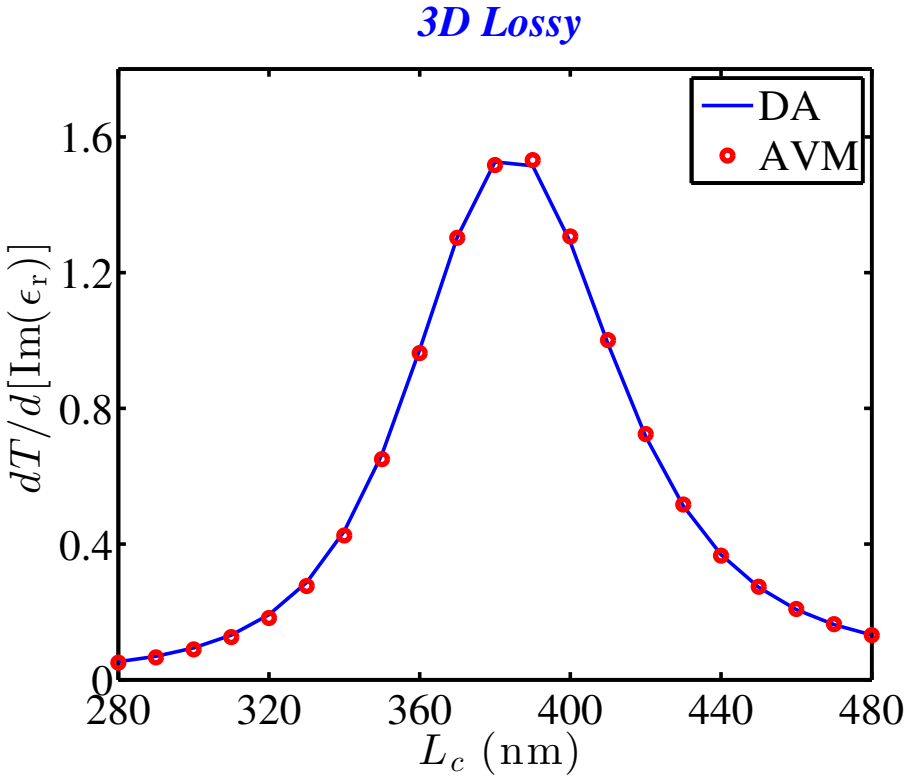

Figure 4.42: Sensitivity of the transmission with respect to the imaginary part of the relative dielectric permittivity inside the cavity of the structure shown in Figure 4.24. Results are calculated using the direct approach (DA) (Eq. 4.55), and the adjoint variable method (AVM) (Eq. 4.54).

Chapter 5
Concluding Remarks and Recommended Future Work

5.1 Conclusions

We first briefly described the history of nanophotonic devices and the need to develop compact active nanophotonic devices, besides the widely investigated passive nanoscale devices. We then considered an absorption switch consisting of a MDM plasmonic waveguide coupled to a conventional Fabry-Perot cavity. Taking advantage of the subwavelength modal size of MDM waveguides to enhance the interaction between light and active material inside the cavity can lead to a compact optical switch. However, the modulation depth of such a switch when optimized is relatively low. We therefore introduced a compact absorption switch consisting of a multisection cavity. The optimized multisection cavity switch led to greatly enhanced modulation depth compared to the optimized Fabry-Perot cavity switch.

We then showed that the space mapping algorithm, originally developed for microwave circuit optimization, can enable the efficient design of nanoplasmonic devices which satisfy a set of desired specifications. Space mapping utilizes a physics-based coarse model to approximate a fine model accurately describing a device.

More specifically, we demonstrated the use of the space mapping algorithm for the design of MDM plasmonic waveguide devices. A set of desired specifications are imposed on the transmission response of the device. The goal is to find the design parameters of the device so that its transmission response satisfies all the specifications. In our case, the fine model was a full-wave FDFD simulation of the device, while the coarse model was based on transmission line theory. We used the aggressive space mapping implementation of the algorithm, which incorporates a quasi-Newton iteration. At each iteration of the

space mapping algorithm we used a parameter extraction procedure to obtain the mapping which corresponds to the optimum match between the coarse and fine model responses. The iterative procedure was terminated when the fine model response satisfied the set of desired specifications.

We considered several examples of the application of the space mapping algorithm for the design of nanoplasmonic waveguide devices. In the first example, we considered a plasmonic MDM waveguide side-coupled to two MDM stub resonators. The transmission line model of this structure consists of two short-circuited transmission line resonators, which are connected in series to a transmission line. In the second example, space mapping was applied to the design of a multicomponent nanoplasmonic device consisting of a MDM plasmonic waveguide side-coupled to two arrays of MDM stub resonators. The transmission line model in this case consists of a transmission line loaded with two arrays of short-circuited transmission line stub resonators. The model was implemented using the transfer matrix of each waveguide section. In the next example, space mapping was applied to the design of a nanoplasmonic waveguide device consisting of deep subwavelength dielectric and metallic structures. These structures were modeled as lumped circuit elements rather than as transmission lines. Finally, in the fourth example we showed that the space mapping algorithm can be efficiently used for the emulation of 2D MDM plasmonic waveguide devices with 3D coaxial waveguide devices. We showed that by applying this algorithm and finding the proper choice of their design parameters, 3D plasmonic coaxial waveguide-cavity devices and 2D MDM devices could have nearly identical transmission spectra. More specifically, we used the space mapping algorithm to find the optimum match between the responses of a 2D and a 3D device, and found that, using this approach, the transmission spectra of the 2D device almost exactly match the spectra of the 3D device.

Through these examples, we showed that simply optimizing the transmission line model of the device is not enough to obtain a device which satisfies all the required design specifications. On the other hand, we found that, when the iterative space mapping algorithm was

used, it converged fast to a design which met all the specifications. In addition, full-wave FDFD simulations of only a few candidate structures were required before the iterative process was terminated. Use of the space mapping algorithm therefore resulted in large reductions in the required computation time when compared to any direct optimization method of the fine FDFD model.

We also presented an analytical adjoint sensitivity method for the power transmission coefficient of nano-optical devices which is directly derived from Maxwell's equations and does not assume any discretization. The adjoint variable method utilizes the main simulation of the device along with an extra one called the adjoint simulation whose excitation is based on the response function. Moreover, by finding analytically a mapping between the solutions of the main and adjoint problems in symmetric devices, we could derive a formula which relates the fields of the adjoint problem and forward problem. Thus, we could obtain the sensitivities with only one numerical simulation. The derived formula was applied to calculate the sensitivity of the power transmission coefficient with respect to the real and imaginary parts of the dielectric permittivity of the active material for two-dimensional and three-dimensional plasmonic devices. We also compared the results with the ones obtained by directly calculating the sensitivity and found that there is excellent agreement between the results obtained with the two methods. This is evidence that the derived formula gives accurate results for the plasmonic devices of interest.

5.2 Recommended future work

The use of more detailed transmission line models for nanoplasmonic waveguides [120, 121] in the space mapping algorithm could potentially further reduce the required number of full-wave simulations during the design process. In addition, the algorithm has already been successfully applied to design a variety of three-dimensional microwave waveguide devices [65, 66]. Based on this, the space mapping algorithm could be applied to design three-

dimensional nanoplasmonic waveguide devices, using as coarse models the transmission line models which have been developed for such waveguides [83].

In addition, plasmon-enhanced photovoltaic solar cells have been extensively investigated in recent years. In general, there are three main ways of using nanoplasmonic structures to enhance optical absorption in thin-film solar cells [122]. First, using metallic nanoparticles as scatterers to trap the light from the Sun. Second, using metallic nanoparticles as nanoantennas with enhanced near-field to increase the absorption of the semiconductor. Third, using corrugated metallic film on the back of the absorber to couple the incident light to the surface plasmon modes at the interface of the metal and semiconductor. All of these methods help to trap light in the smaller photovoltaic layer and to improve the optical absorption. A variety of analytical and semi-analytical models have been developed and suggested by different groups to investigate these devices [123]. However, these methods are typically of limited accuracy when compared to full-wave electromagnetic simulations. The space mapping algorithm could be used in combination with these models to efficiently design and optimize complicated plasmon-enhanced photovoltaic devices with enhanced absorption efficiency.

Space mapping could also be employed to design a variety of other nanoplasmonic structures and devices, such as arrays of holes in metallic films, metallic gratings, and metallic nanoparticle arrays, using the analytical or quasi-analytical physics-based models which have been developed for such structures.

References

[1] R. Kurzweil, *The Law of Accelerating Returns*. Springer, 2004.

[2] N. Kinsey, M. Ferrera, V. Shalaev, and A. Boltasseva, "Examining nanophotonics for integrated hybrid systems: a review of plasmonic interconnects and modulators using traditional and alternative materials [invited]," *Journal of the Optical Society of America B Optical Physics*, vol. 32, pp. 121–142, 2015.

[3] M. L. Brongersma and P. G. Kik, *Surface Plasmon Nanophotonics*. Springer, 2007.

[4] D. K. Gramotnev and S. I. Bozhevolnyi, "Plasmonics beyond the diffraction limit," *Nature Photonics*, vol. 4, no. 2, pp. 83–91, 2010.

[5] R. Soref, "The past, present, and future of silicon photonics," *IEEE Journal of Selected Topics in Quantum Electronics*, vol. 12, no. 6, pp. 1678–1687, 2006.

[6] H. Raether, *Surface Plasmons on Smooth Surfaces*. Springer, 1988.

[7] S. I. Bozhevolnyi, "Plasmonic nano-guides and circuits," in *Plasmonics and Metamaterials*, p. MWD3, Optical Society of America, 2008.

[8] S. A. Maier, *Plasmonics: Fundamentals and Applications*. Springer Science & Business Media, 2007.

[9] W. L. Barnes, A. Dereux, and T. W. Ebbesen, "Surface plasmon subwavelength optics," *Nature*, vol. 424, no. 6950, pp. 824–830, 2003.

[10] H. A. Atwater, "The promise of plasmonics," *Scientific American*, vol. 296, no. 4, pp. 56–62, 2007.

[11] E. Ozbay, "Plasmonics: merging photonics and electronics at nanoscale dimensions," *Science*, vol. 311, no. 5758, pp. 189–193, 2006.

[12] J. A. Schuller, E. S. Barnard, W. Cai, Y. C. Jun, J. S. White, and M. L. Brongersma, "Plasmonics for extreme light concentration and manipulation," *Nature Materials*, vol. 9, no. 3, pp. 193–204, 2010.

[13] S. Lal, S. Link, and N. J. Halas, "Nano-optics from sensing to waveguiding," *Nature Photonics*, vol. 1, no. 11, pp. 641–648, 2007.

[14] M. I. Stockman, "Nanoplasmonics: past, present, and glimpse into future," *Optics Express*, vol. 19, no. 22, pp. 22029–22106, 2011.

[15] V. J. Sorger, R. F. Oulton, R.-M. Ma, and X. Zhang, "Toward integrated plasmonic circuits," *MRS Bulletin*, vol. 37, no. 8, pp. 728–738, 2012.

[16] D. F. Welch, F. A. Kish, R. Nagarajan, C. H. Joyner, R. P. Schneider Jr, V. G. Dominic, M. L. Mitchell, S. G. Grubb, T.-K. Chiang, D. D. Perkins, and N. A. C, "The realization of large-scale photonic integrated circuits and the associated impact on fiber-optic communication systems," *Journal of Lightwave Technology*, vol. 24, no. 12, pp. 4674–4683, 2006.

[17] D. A. B. Miller, "Are optical transistors the logical next step?," *Nature Photonics*, vol. 4, no. 1, pp. 3–5, 2010.

[18] A. K. Okyay, A. J. Pethe, D. Kuzum, S. Latif, D. A. B. Miller, and K. C. Saraswat, "SiGe optoelectronic metal-oxide semiconductor field-effect transistor," *Optics Letters*, vol. 32, no. 14, pp. 2022–2024, 2007.

[19] K. Sasaki, S. Sasaki, and O. Furukawa, "All-optical switches and all-optical bistability by nonlinear optical materials," in *MRS Proceedings*, vol. 247, p. 141, Cambridge University Press, 1992.

[20] M. Hochberg, T. Baehr-Jones, G. Wang, M. Shearn, K. Harvard, J. Luo, B. Chen, Z. Shi, R. Lawson, P. Sullivan, *et al.*, "Terahertz all-optical modulation in a silicon–polymer hybrid system," *Nature Materials*, vol. 5, no. 9, pp. 703–709, 2006.

[21] G. T. Sincerbox and J. C. Gordon, "Small fast large-aperture light modulator using attenuated total reflection," *Applied Optics*, vol. 20, no. 8, pp. 1491–1496, 1981.

[22] J. S. Schildkraut, "Long-range surface plasmon electrooptic modulator," *Applied Optics*, vol. 27, no. 21, pp. 4587–4590, 1988.

[23] O. Solgaard, F. Ho, J. Thackara, and D. Bloom, "High frequency attenuated total internal reflection light modulator," *Applied Physics Letters*, vol. 61, no. 21, pp. 2500–2502, 1992.

[24] C. Jung, S. Yee, and K. Kuhn, "Electro-optic polymer light modulator based on surface plasmon resonance," *Applied Optics*, vol. 34, no. 6, pp. 946–949, 1995.

[25] A. Liu, R. Jones, L. Liao, D. Samara-Rubio, D. Rubin, O. Cohen, R. Nicolaescu, and M. Paniccia, "A high-speed silicon optical modulator based on a metal–oxide–semiconductor capacitor," *Nature*, vol. 427, no. 6975, pp. 615–618, 2004.

[26] J. A. Dionne, K. Diest, L. A. Sweatlock, and H. A. Atwater, "Plasmostor: a metal-oxide-si field effect plasmonic modulator," *Nano Letters*, vol. 9, no. 2, pp. 897–902, 2009.

[27] V. J. Sorger, N. D. Lanzillotti-Kimura, R.-M. Ma, and X. Zhang, "Ultra-compact silicon nanophotonic modulator with broadband response," *Nanophotonics*, vol. 1, no. 1, pp. 17–22, 2012.

[28] B. E. Saleh, M. C. Teich, and B. E. Saleh, *Fundamentals of Photonics*, vol. 22. Wiley New York, 1991.

[29] T. Nikolajsen, K. Leosson, and S. I. Bozhevolnyi, "Surface plasmon polariton based modulators and switches operating at telecom wavelengths," *Applied Physics Letters*, vol. 85, no. 24, pp. 5833–5835, 2004.

[30] J. Gosciniak, S. I. Bozhevolnyi, T. B. Andersen, V. S. Volkov, J. Kjelstrup-Hansen, L. Markey, and A. Dereux, "Thermo-optic control of dielectric-loaded plasmonic waveguide components," *Optics Express*, vol. 18, no. 2, pp. 1207–1216, 2010.

[31] M. Pu, N. Yao, C. Hu, X. Xin, Z. Zhao, C. Wang, and X. Luo, "Directional coupler and nonlinear mach-zehnder interferometer based on metal-insulator-metal plasmonic waveguide," *Optics Express*, vol. 18, no. 20, pp. 21030–21037, 2010.

[32] S. Zhu, G. Lo, and D. Kwong, "Theoretical investigation of silicon mos-type plasmonic slot waveguide based mzi modulators," *Optics Express*, vol. 18, no. 26, pp. 27802–27819, 2010.

[33] M. J. Dicken, L. A. Sweatlock, D. Pacifici, H. J. Lezec, K. Bhattacharya, and H. A. Atwater, "Electrooptic modulation in thin film barium titanate plasmonic interferometers," *Nano Letters*, vol. 8, no. 11, pp. 4048–4052, 2008.

[34] W. Dickson, G. A. Wurtz, P. R. Evans, R. J. Pollard, and A. V. Zayats, "Electronically controlled surface plasmon dispersion and optical transmission through metallic hole arrays using liquid crystal," *Nano Letters*, vol. 8, no. 1, pp. 281–286, 2008.

[35] G. A. Wurtz and A. V. Zayats, "Nonlinear surface plasmon polaritonic crystals," *Laser & Photonics Reviews*, vol. 2, no. 3, pp. 125–135, 2008.

[36] C. Min, P. Wang, C. Chen, Y. Deng, Y. Lu, H. Ming, T. Ning, Y. Zhou, and G. Yang, "All-optical switching in subwavelength metallic grating structure containing nonlinear optical materials," *Optics Letters*, vol. 33, no. 8, pp. 869–871, 2008.

[37] Z. Yu, G. Veronis, S. Fan, and M. L. Brongersma, "Gain-induced switching in metal-dielectric-metal plasmonic waveguides," *Applied Physics Letters*, vol. 92, no. 4, p. 041117, 2008.

[38] A. Lereu, A. Passian, J. Goudonnet, T. Thundat, and T. Ferrell, "Optical modulation processes in thin films based on thermal effects of surface plasmons," *Applied Physics Letters*, vol. 86, no. 15, p. 154101, 2005.

[39] A. V. Krasavin and N. Zheludev, "Active plasmonics: Controlling signals in au/ga waveguide using nanoscale structural transformations," *Applied Physics Letters*, vol. 84, no. 8, pp. 1416–1418, 2004.

[40] K. F. MacDonald, Z. L. Sámson, M. I. Stockman, and N. I. Zheludev, "Ultrafast active plasmonics," *Nature Photonics*, vol. 3, no. 1, pp. 55–58, 2009.

[41] G. Veronis and S. Fan, "Bends and splitters in metal-dielectric-metal subwavelength plasmonic waveguides," *Applied Physics Letters*, vol. 87, no. 13, p. 131102, 2005.

[42] C. Min and G. Veronis, "Absorption switches in metal-dielectric-metal plasmonic waveguides," *Optics Express*, vol. 17, no. 13, pp. 10757–10766, 2009.

[43] W. Cai, J. S. White, and M. L. Brongersma, "Compact, high-speed and power-efficient electrooptic plasmonic modulators," *Nano Letters*, vol. 9, no. 12, pp. 4403–4411, 2009.

[44] E. D. Palik, *Handbook of Optical Constants of Solids*, vol. 3. Academic Press, 1998.

[45] J.-M. Jin, *The Finite Element Method in Electromagnetics*. John Wiley & Sons, 2014.

[46] D. Pacifici, H. J. Lezec, and H. A. Atwater, "All-optical modulation by plasmonic excitation of cdse quantum dots," *Nature Photonics*, vol. 1, no. 7, pp. 402–406, 2007.

[47] D. Pacifici, H. J. Lezec, L. A. Sweatlock, C. de Ruiter, V. Ferry, and H. A. Atwater, "All–optical plasmonic modulators and interconnects," *Plasmonic Nanoguides and Circuits*, p. 189, 2009.

[48] G. Veronis and S. Fan, "Theoretical investigation of compact couplers between dielectric slab waveguides and two-dimensional metal-dielectric-metal plasmonic waveguides," *Optics Express*, vol. 15, no. 3, pp. 1211–1221, 2007.

[49] Y. Xu, Y. Li, R. K. Lee, and A. Yariv, "Scattering-theory analysis of waveguide-resonator coupling," *Physical Review E*, vol. 62, no. 5, p. 7389, 2000.

[50] G. Veronis, R. W. Dutton, and S. Fan, "Method for sensitivity analysis of photonic crystal devices," *Optics Letters*, vol. 29, no. 19, pp. 2288–2290, 2004.

[51] R. F. Harrington, *Time-Harmonic Electromagnetic Fields*. McGraw-Hill, 1961.

[52] A. Raman and S. Fan, "Perturbation theory for plasmonic modulation and sensing," *Physical Review B*, vol. 83, no. 20, p. 205131, 2011.

[53] P. Berini, "Bulk and surface sensitivities of surface plasmon waveguides," *New Journal of Physics*, vol. 10, no. 10, p. 105010, 2008.

[54] G. Veronis, Z. Yu, S. E. Kocabas, D. A. B. Miller, M. L. Brongersma, and S. Fan, "Metal-dielectric-metal plasmonic waveguide devices for manipulating light at the nanoscale," *Chinese Optics Letters*, vol. 7, no. 4, pp. 302–308, 2009.

[55] P. Dastmalchi and G. Veronis, "Efficient design of nanoplasmonic waveguide devices using the space mapping algorithm," *Optics Express*, vol. 21, no. 26, pp. 32160–32175, 2013.

[56] N. Hodgson and H. Weber, *Laser Resonators and Beam Propagation: Fundamentals, Advanced Concepts, Applications*, vol. 108. Springer, 2005.

[57] R. Zia, J. A. Schuller, A. Chandran, and M. L. Brongersma, "Plasmonics: the next chip-scale technology," *Materials Today*, vol. 9, no. 7, pp. 20–27, 2006.

[58] S. A. Maier and H. A. Atwater, "Plasmonics: Localization and guiding of electromagnetic energy in metal/dielectric structures," *Journal of Applied Physics*, vol. 98, no. 1, p. 011101, 2005.

[59] C. Min, L. Yang, and G. Veronis, "Microcavity enhanced optical absorption in subwavelength slits," *Optics Express*, vol. 19, no. 27, pp. 26850–26858, 2011.

[60] Y. Huang, C. Min, P. Dastmalchi, and G. Veronis, "Slow-light enhanced subwavelength plasmonic waveguide refractive index sensors," *Optics Express*, vol. 23, no. 11, pp. 14922–14936, 2015.

[61] T. Tanemura, K. C. Balram, D.-S. Ly-Gagnon, P. Wahl, J. S. White, M. L. Brongersma, and D. A. B. Miller, "Multiple-wavelength focusing of surface plasmons with a nonperiodic nanoslit coupler," *Nano Letters*, vol. 11, no. 7, pp. 2693–2698, 2011.

[62] R. M. Briggs, J. Grandidier, S. P. Burgos, E. Feigenbaum, and H. A. Atwater, "Efficient coupling between dielectric-loaded plasmonic and silicon photonic waveguides," *Nano Letters*, vol. 10, no. 12, pp. 4851–4857, 2010.

[63] C. Delacour, S. Blaize, P. Grosse, J. M. Fedeli, A. Bruyant, R. Salas-Montiel, G. Lerondel, and A. Chelnokov, "Efficient directional coupling between silicon and copper plasmonic nanoslot waveguides: toward metal-oxide-silicon nanophotonics," *Nano Letters*, vol. 10, no. 8, pp. 2922–2926, 2010.

[64] J. W. Bandler, R. M. Biernacki, S. H. Chen, R. H. Hemmers, and K. Madsen, "Electromagnetic optimization exploiting aggressive space mapping," *IEEE Transactions on Microwave Theory and Techniques*, vol. 43, no. 12, pp. 2874–2882, 1995.

[65] J. W. Bandler, Q. S. Cheng, S. Dakroury, A. S. Mohamed, M. H. Bakr, K. Madsen, J. Søndergaard, *et al.*, "Space mapping: the state of the art," *IEEE Transactions on Microwave Theory and Techniques*, vol. 52, no. 1, pp. 337–361, 2004.

[66] S. Koziel, Q. S. Cheng, and J. W. Bandler, "Space mapping," *IEEE Microwave Magazine*, vol. 9, no. 6, pp. 105–122, 2008.

[67] C. G. Broyden, "A class of methods for solving nonlinear simultaneous equations," *Mathematics of Computation*, pp. 577–593, 1965.

[68] P. J. Huber, *Robust Statistics*. Springer, 2011.

[69] J. W. Bandler, S. H. Chen, R. M. Biernacki, L. Gao, K. Madsen, and H. Yu, "Huber optimization of circuits: A robust approach," *IEEE Transactions on Microwave Theory and Techniques*, vol. 41, no. 12, pp. 2279–2287, 1993.

[70] S.-D. Wu and E. N. Glytsis, "Finite-number-of-periods holographic gratings with finite-width incident beams: analysis using the finite-difference frequency-domain method," *Journal of the Optical Society of America A*, vol. 19, no. 10, pp. 2018–2029, 2002.

[71] A. Taflove and S. C. Hagness, *Computational Electrodynamics*. Artech House, 2005.

[72] Y. Huang, C. Min, and G. Veronis, "Subwavelength slow-light waveguides based on a plasmonic analogue of electromagnetically induced transparency," *Applied Physics Letters*, vol. 99, no. 14, p. 143117, 2011.

[73] D. M. Pozar, *Microwave Engineering*. John Wiley & Sons, 2009.

[74] Y. Huang, C. Min, L. Yang, and G. Veronis, "Nanoscale plasmonic devices based on metal-dielectric-metal stub resonators," *International Journal of Optics*, vol. 2012, 2012.

[75] S. E. Kocabas, G. Veronis, D. A. B. Miller, and S. Fan, "Transmission line and equivalent circuit models for plasmonic waveguide components," *IEEE Journal of Selected Topics in Quantum Electronics*, vol. 14, no. 6, pp. 1462–1472, 2008.

[76] D. Pacifici, H. Lezec, H. A. Atwater, and J. Weiner, "Quantitative determination of optical transmission through subwavelength slit arrays in ag films: Role of surface wave interference and local coupling between adjacent slits," *Physical Review B*, vol. 77, no. 11, p. 115411, 2008.

[77] D. Pacifici, H. J. Lezec, L. A. Sweatlock, R. J. Walters, and H. A. Atwater, "Universal optical transmission features in periodic and quasiperiodic hole arrays," *Optics Express*, vol. 16, no. 12, pp. 9222–9238, 2008.

[78] K. Krishnakumar, "Micro-genetic algorithms for stationary and non-stationary function optimization," in *1989 Advances in Intelligent Robotics Systems Conference*, pp. 289–296, International Society for Optics and Photonics, 1990.

[79] J. Tao, X. G. Huang, X. Lin, Q. Zhang, and X. Jin, "A narrow-band subwavelength plasmonic waveguide filter with asymmetrical multiple-teeth-shaped structure," *Optics Express*, vol. 17, no. 16, pp. 13989–13994, 2009.

[80] R. E. Collin, *Foundations for Microwave Engineering*. John Wiley & Sons, 2007.

[81] N. Engheta, "Circuits with light at nanoscales: optical nanocircuits inspired by metamaterials," *Science*, vol. 317, no. 5845, pp. 1698–1702, 2007.

[82] A. Alù, M. E. Young, and N. Engheta, "Design of nanofilters for optical nanocircuits," *Physical Review B*, vol. 77, no. 14, p. 144107, 2008.

[83] W. Shin, W. Cai, P. B. Catrysse, G. Veronis, M. L. Brongersma, and S. Fan, "Broadband sharp 90-degree bends and t-splitters in plasmonic coaxial waveguides," *Nano Letters*, vol. 13, no. 10, pp. 4753–4758, 2013.

[84] A. Mahigir, P. Dastmalchi, W. Shin, S. Fan, and G. Veronis, "Plasmonic coaxial waveguide-cavity devices," *Optics Express*, vol. 23, no. 16, pp. 20549–20562, 2015.

[85] X.-S. Lin and X.-G. Huang, "Tooth-shaped plasmonic waveguide filters with nanometeric sizes," *Optics Letters*, vol. 33, no. 23, pp. 2874–2876, 2008.

[86] A. Hosseini and Y. Massoud, "Nanoscale surface plasmon based resonator using rectangular geometry," *Applied Physics Letters*, vol. 90, no. 18, p. 181102, 2007.

[87] I. Zand, A. Mahigir, T. Pakizeh, and M. S. Abrishamian, "Selective-mode optical nanofilters based on plasmonic complementary split-ring resonators," *Optics Express*, vol. 20, no. 7, pp. 7516–7525, 2012.

[88] L. Yang, C. Min, and G. Veronis, "Guided subwavelength slow-light mode supported by a plasmonic waveguide system," *Optics Letters*, vol. 35, no. 24, pp. 4184–4186, 2010.

[89] A. Pannipitiya, I. D. Rukhlenko, M. Premaratne, H. T. Hattori, and G. P. Agrawal, "Improved transmission model for metal-dielectric-metal plasmonic waveguides with stub structure," *Optics Express*, vol. 18, no. 6, pp. 6191–6204, 2010.

[90] Z.-J. Zhong, Y. Xu, S. Lan, Q.-F. Dai, and L.-J. Wu, "Sharp and asymmetric transmission response in metal-dielectric-metal plasmonic waveguides containing kerr nonlinear media," *Optics Express*, vol. 18, no. 1, pp. 79–86, 2010.

[91] J. Liu, G. Fang, H. Zhao, Y. Zhang, and S. Liu, "Surface plasmon reflector based on serial stub structure," *Optics Express*, vol. 17, no. 22, pp. 20134–20139, 2009.

[92] F. Hu, H. Yi, and Z. Zhou, "Wavelength demultiplexing structure based on arrayed plasmonic slot cavities," *Optics Letters*, vol. 36, no. 8, pp. 1500–1502, 2011.

[93] S. R. Mirnaziry, A. Setayesh, and M. S. Abrishamian, "Design and analysis of plasmonic filters based on stubs," *Journal of the Optical Society of America B*, vol. 28, no. 5, pp. 1300–1307, 2011.

[94] N. Nozhat and N. Granpayeh, "Analysis of the plasmonic power splitter and mux/demux suitable for photonic integrated circuits," *Optics Communications*, vol. 284, no. 13, pp. 3449–3455, 2011.

[95] M. Povinelli, S. G. Johnson, S. Fan, and J. Joannopoulos, "Emulation of two-dimensional photonic crystal defect modes in a photonic crystal with a three-dimensional photonic band gap," *Physical Review B*, vol. 64, no. 7, p. 075313, 2001.

[96] V. Liu, D. A. B. Miller, S. Fan, *et al.*, "Highly tailored computational electromagnetics methods for nanophotonic design and discovery.," *Proceedings of the IEEE*, vol. 101, no. 2, pp. 484–493, 2013.

[97] A. C. Niederberger, D. A. Fattal, N. R. Gauger, S. Fan, and R. G. Beausoleil, "Sensitivity analysis and optimization of sub-wavelength optical gratings using adjoints," *Optics Express*, vol. 22, no. 11, p. 12, 2014.

[98] J. L. Lions, *Optimal Control of Systems Governed by Partial Differential Equations*, vol. 170. Springer Verlag, 1971.

[99] D. Rumelhart, G. Hinton, and R. Williams, "Learning internal representations by error propagation, parallel distributed processing, explorations in the microstructure of cognition, vol. 1. 1986," 1986.

[100] R. Becker and R. Rannacher, "An optimal control approach to error control and mesh adaptation," *Acta Numerica*, vol. 10, pp. 1–102, 2001.

[101] O. Pironneau, "On optimum design in fluid mechanics," *Journal of Fluid Mechanics*, vol. 64, no. 01, pp. 97–110, 1974.

[102] A. Jameson, "Aerodynamic design via control theory," *Journal of Scientific Computing*, vol. 3, no. 3, pp. 233–260, 1988.

[103] A. Jameson, "Optimum aerodynamic design using cfd and control theory," *American Institute of Aeronautics and Astronautics*, vol. 1729, pp. 124–131, 1995.

[104] A. Jameson, L. Martinelli, and N. Pierce, "Optimum aerodynamic design using the navier-stokes equations," *Theoretical and Computational Fluid Dynamics*, vol. 10, no. 1-4, pp. 213–237, 1998.

[105] J. J. Reuther, A. Jameson, J. J. Alonso, M. J. Rimllnger, and D. Saunders, "Constrained multipoint aerodynamic shape optimization using an adjoint formulation and parallel computers, part 1," *Journal of Aircraft*, vol. 36, no. 1, pp. 51–60, 1999.

[106] J. J. Reuther, A. Jameson, J. J. Alonso, M. J. Rimllnger, and D. Saunders, "Constrained multipoint aerodynamic shape optimization using an adjoint formulation and parallel computers, part 2," *Journal of Aircraft*, vol. 36, no. 1, pp. 61–74, 1999.

[107] V. Komkov, K. K. Choi, and E. J. Haug, *Design Sensitivity Analysis of Structural Systems*, vol. 177. Academic Press, 1986.

[108] Y.-S. Chung, C. Cheon, I.-H. Park, and S.-Y. Hahn, "Optimal shape design of microwave device using fdtd and design sensitivity analysis," *IEEE Transactions on Microwave Theory and Techniques*, vol. 48, no. 12, pp. 2289–2296, 2000.

[109] N. K. Georgieva, S. Glavic, M. H. Bakr, and J. W. Bandler, "Feasible adjoint sensitivity technique for em design optimization," *IEEE Transactions on Microwave Theory and Techniques*, vol. 50, no. 12, pp. 2751–2758, 2002.

[110] N. K. Nikolova, H. W. Tam, and M. H. Bakr, "Sensitivity analysis with the fdtd method on structured grids," *IEEE Transactions on Microwave Theory and Techniques*, vol. 52, no. 4, pp. 1207–1216, 2004.

[111] N. K. Nikolova, Y. Li, Y. Li, and M. H. Bakr, "Sensitivity analysis of scattering parameters with electromagnetic time-domain simulators," *IEEE Transactions on Microwave Theory and Techniques*, vol. 54, no. 4, pp. 1598–1610, 2006.

[112] Y. Jiao, S. Fan, and D. A. B. Miller, "Photonic crystal device sensitivity analysis with wannier basis gradients," *Optics Letters*, vol. 30, no. 3, pp. 302–304, 2005.

[113] P. Seliger, M. Mahvash, C. Wang, and A. Levi, "Optimization of aperiodic dielectric structures," *Journal of Applied Physics*, vol. 100, no. 3, p. 034310, 2006.

[114] C. M. Lalau-Keraly, S. Bhargava, O. D. Miller, and E. Yablonovitch, "Adjoint shape optimization applied to electromagnetic design," *Optics Express*, vol. 21, no. 18, pp. 21693–21701, 2013.

[115] O. D. Miller, C. W. Hsu, M. Reid, W. Qiu, B. G. DeLacy, J. D. Joannopoulos, M. Soljačić, and S. G. Johnson, "Fundamental limits to extinction by metallic nanoparticles," *Physical Review Letters*, vol. 112, no. 12, p. 123903, 2014.

[116] P. Hansen and L. Hesselink, "Accurate adjoint design sensitivities for nano metal optics," *Optics Express*, vol. 23, no. 18, pp. 23899–23923, 2015.

[117] C. Vassallo, *Optical Waveguide Concepts*. Elsevier, 1991.

[118] M. S. Dadash, N. K. Nikolova, and J. W. Bandler, "Analytical adjoint sensitivity formula for the scattering parameters of metallic structures," *IEEE Transactions on Microwave Theory and Techniques*, vol. 60, no. 9, pp. 2713–2722, 2012.

[119] N. K. Nikolova, X. Zhu, Y. Song, A. Hasib, and M. H. Bakr, "S-parameter sensitivities for electromagnetic optimization based on volume field solutions," *IEEE Transactions on Microwave Theory and Techniques*, vol. 57, no. 6, pp. 1526–1538, 2009.

[120] H. Nejati and A. Beirami, "Theoretical analysis of the characteristic impedance in metal–insulator–metal plasmonic transmission lines," *Optics Letters*, vol. 37, no. 6, pp. 1050–1052, 2012.

[121] D. Li and E.-P. Li, "Impedance calculation and equivalent circuits for metal–insulator–metal plasmonic waveguide geometries," *Optics Letters*, vol. 38, no. 17, pp. 3384–3386, 2013.

[122] H. A. Atwater and A. Polman, "Plasmonics for improved photovoltaic devices," *Nature Materials*, vol. 9, no. 3, pp. 205–213, 2010.

[123] R. A. Pala, J. S. Liu, E. S. Barnard, D. Askarov, E. C. Garnett, S. Fan, and M. L. Brongersma, "Optimization of non-periodic plasmonic light-trapping layers for thin-film solar cells," *Nature Communications*, vol. 4, p. 2095, 2013.

Appendix A
Proof of Eq. 2.1

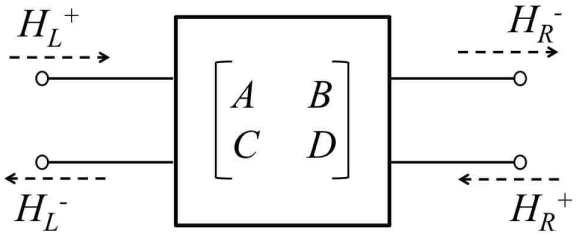

Figure A.1: Schematic diagram of modal propagation in a two-port device.

Considering a symmetric two-port device (Figure A.1) which is composed of reciprocal media (i.e., symmetric permittivity and permeability tensors) the amplitude and phases of the modes that arrive at (H^+) and propagate away from (H^-) the first port can be related to the amplitude and phases of the modes that arrive at and propagate away from the second port as:

$$\begin{bmatrix} A & B \\ C & D \end{bmatrix} \begin{bmatrix} H_L^+ \\ H_L^- \end{bmatrix} = \begin{bmatrix} H_R^- \\ H_R^+ \end{bmatrix}. \tag{A.1}$$

Assume that the incident wave is arriving at the first port and that it is normalized such that the mode has a unit magnitude at the input of the device (port 1). Then we have:

$$if \quad H_L^+ = 1 \Rightarrow \begin{cases} H_R^- = t \\ H_L^- = r \\ H_R^+ = 0 \end{cases}. \tag{A.2}$$

Here r is the complex magnetic field reflection coefficient and t is the transmission coefficient of the device. Substituting them in Eq. A.1 gives:

$$\Rightarrow \begin{bmatrix} A & B \\ C & D \end{bmatrix} \begin{bmatrix} 1 \\ r \end{bmatrix} = \begin{bmatrix} t \\ 0 \end{bmatrix} \Rightarrow \begin{cases} A + Br = t \\ C + Dr = 0 \end{cases} . \tag{A.3}$$

Now if we assume that the normalized incident wave arrives at the second port, because of the symmetry we have:

$$if \quad H_R^+ = 1 \Rightarrow \begin{cases} H_L^- = t \\ H_R^- = r \\ H_L^+ = 0 \end{cases} , \tag{A.4}$$

and again inserting them in Eq. A.1 gives:

$$\Rightarrow \begin{bmatrix} A & B \\ C & D \end{bmatrix} \begin{bmatrix} 0 \\ t \end{bmatrix} = \begin{bmatrix} r \\ 1 \end{bmatrix} \Rightarrow \begin{cases} Bt = r \\ Dt = 1 \end{cases} . \tag{A.5}$$

Combining equations (A.3) and (A.5) one can obtain:

$$\Rightarrow \begin{cases} A = t - \frac{r^2}{t} \\ B = \frac{r}{t} \\ C = -\frac{r}{t} \\ D = \frac{1}{t} \end{cases} , \tag{A.6}$$

or in matrix form:

$$\begin{bmatrix} A & B \\ C & D \end{bmatrix} = \frac{1}{t} \begin{bmatrix} t^2 - r^2 & r \\ -r & 1 \end{bmatrix} . \tag{A.7}$$

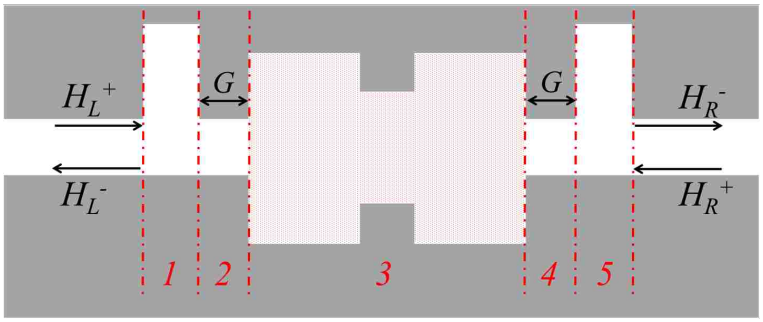

Figure A.2: Schematic of the optimized multisection cavity switch as an example of a multi-section device which consists of different separate components connected in a cascade form.

Considering a multi-section device such as the proposed absorption switch which consists of different separate components connected in a cascade form, the overall ABCD matrix can be calculated as the product of the individual matrices by keeping the order:

$$\begin{bmatrix} A & B \\ C & D \end{bmatrix} \begin{bmatrix} H_L^+ \\ H_L^- \end{bmatrix} = \begin{bmatrix} H_R^- \\ H_R^+ \end{bmatrix}, \tag{A.8}$$

$$\begin{bmatrix} A & B \\ C & D \end{bmatrix} = \begin{bmatrix} A_5 & B_5 \\ C_5 & D_5 \end{bmatrix} \begin{bmatrix} A_4 & B_4 \\ C_4 & D_4 \end{bmatrix} \begin{bmatrix} A_3 & B_3 \\ C_3 & D_3 \end{bmatrix} \begin{bmatrix} A_2 & B_2 \\ C_2 & D_2 \end{bmatrix} \begin{bmatrix} A_1 & B_1 \\ C_1 & D_1 \end{bmatrix}. \tag{A.9}$$

In the proposed structure the gaps between the stubs and the cavity are simple MDM waveguides with the complex propagation constant of γ and the length of G. Therefore the ABCD matrix for each of them can be obtained as:

$$\begin{bmatrix} A_2 & B_2 \\ C_2 & D_2 \end{bmatrix} = \begin{bmatrix} A_4 & B_4 \\ C_4 & D_4 \end{bmatrix} = \begin{bmatrix} e^{-\gamma G} & 0 \\ 0 & e^{\gamma G} \end{bmatrix}. \tag{A.10}$$

The stub resonators are also identical, therefore their transmission matrices are identical:

$$\begin{bmatrix} A_1 & B_1 \\ C_1 & D_1 \end{bmatrix} = \begin{bmatrix} A_5 & B_5 \\ C_5 & D_5 \end{bmatrix}. \tag{A.11}$$

By inserting Eq. A.10 and Eq. A.11 into Eq. A.9, each component of the overall ABCD matrix can be obtained as:

$$\Rightarrow \begin{cases} A = A_1^2 A_3 e^{-2\gamma G} + A_1 B_3 C_1 + A_1 B_1 C_3 + B_1 C_1 D_3 e^{2\gamma G} \\ B = A_1 A_3 B_1 e^{-2\gamma G} + A_1 B_3 D_1 + B_1^2 C_3 + B_1 D_1 D_3 e^{2\gamma G} \\ C = A_1 A_3 C_1 e^{-2\gamma G} + B_3 C_1^2 + A_1 C_3 D_1 + C_1 D_1 D_3 e^{2\gamma G} \\ D = A_3 B_1 C_1 e^{-2\gamma G} + B_3 C_1 D_1 + B_1 C_3 D_1 + D_1^2 D_3 e^{2\gamma G} \end{cases} . \tag{A.12}$$

By definition, the power transmission coefficient T is:

$$T = \left| \frac{H_R^-}{H_L^+}|_{H_R^+=0} \right|^2 = \left| \frac{1}{D} \right|^2 , \tag{A.13}$$

$$T = \left| \frac{1}{A_3 B_1 C_1 e^{-2\gamma G} + B_3 C_1 D_1 + B_1 C_3 D_1 + D_1^2 D_3 e^{2\gamma G}} \right|^2 . \tag{A.14}$$

Using the fields obtained by numerical simulation methods such as FDFD the transmission and reflection coefficients for the stubs (t_s and r_s) and cavity (t_c and r_c) can be extracted and substituted in Eq. A.6 to find their ABCD matrices

$$\begin{bmatrix} A_1 & B_1 \\ C_1 & D_1 \end{bmatrix} = \begin{bmatrix} A_5 & B_5 \\ C_5 & D_5 \end{bmatrix} = \begin{bmatrix} t_s - \frac{r_s^2}{t_s} & \frac{r_s}{t_s} \\ -\frac{r_s}{t_s} & \frac{1}{t_s} \end{bmatrix} , \tag{A.15}$$

$$\begin{bmatrix} A_3 & B_3 \\ C_3 & D_3 \end{bmatrix} = \begin{bmatrix} t_c - \frac{r_c^2}{t_c} & \frac{r_c}{t_c} \\ -\frac{r_c}{t_c} & \frac{1}{t_c} \end{bmatrix} . \tag{A.16}$$

By substituting equations (A.15) and (A.16) in Eq. A.14, the power transmission of the proposed absorption switch can be calculated as:

$$T = \left| \frac{t_s^2 t_c e^{-2\gamma G}}{1 - 2 r_s r_c e^{-2\gamma G} + (r_s^2 r_c^2 - r_s^2 t_c^2) e^{-4\gamma G}} \right|^2 . \tag{A.17}$$

Appendix B
Transmission Line Models

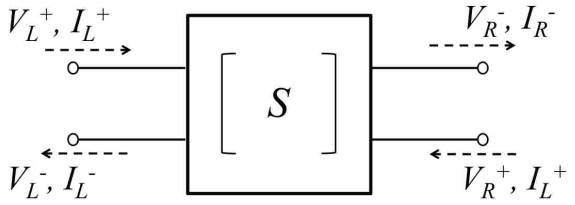

Figure B.1: Schematic diagram of modal propagation in a two-port device.

The transverse fields of traveling waves in an arbitrary waveguide can be written as [73]:

$$\mathbf{E}_t(x,y,z) = \mathbf{e}(x,y)(A^+e^{-\gamma z} + A^-e^{-\gamma z}) = \frac{\mathbf{e}(x,y)}{C_1}(V^+e^{-\gamma z} + V^-e^{-\gamma z}), \tag{B.1}$$

$$\mathbf{H}_t(x,y,z) = \mathbf{h}(x,y)(A^+e^{-\gamma z} - A^-e^{-\gamma z}) = \frac{\mathbf{e}(x,y)}{C_2}(I^+e^{-\gamma z} - I^-e^{-\gamma z}). \tag{B.2}$$

We assume that the propagation is in the z direction. Here, $\mathbf{e}$ and $\mathbf{h}$ are the transverse field variations of the mode and A^+, A^- are the field amplitudes of the traveling waves. Then the characteristic impedance Z_0 would be $\frac{V^+}{I^+} = \frac{V^-}{I^-} = Z_0$. The equivalent voltage and current waves can be defined as:

$$V(z) = V^+e^{-\gamma z} + V^-e^{-\gamma z}, \tag{B.3}$$

$$I(z) = I^+e^{-\gamma z} - I^-e^{-\gamma z}. \tag{B.4}$$

For any two-port device the scattering matrix S relates the voltage waves incident on the ports $\{V_L^+, V_R^+\}$ to those reflected from the ports $\{V_L^-, V_R^-\}$ as an input–output pair (Figure B.1).

$$\begin{bmatrix} V_L^- \\ V_R^- \end{bmatrix} = \begin{bmatrix} S_{11} & S_{12} \\ S_{21} & S_{22} \end{bmatrix} \begin{bmatrix} V_L^+ \\ V_R^+ \end{bmatrix}. \tag{B.5}$$

But when different components are cascaded, the overall scattering matrix for the system is not the product of individual scattering matrices. Thus what we need to do is to find first the transmission matrix T of each individual component and after that to obtain the overall transmission matrix which is the product of the cascaded components (Figure B.2).

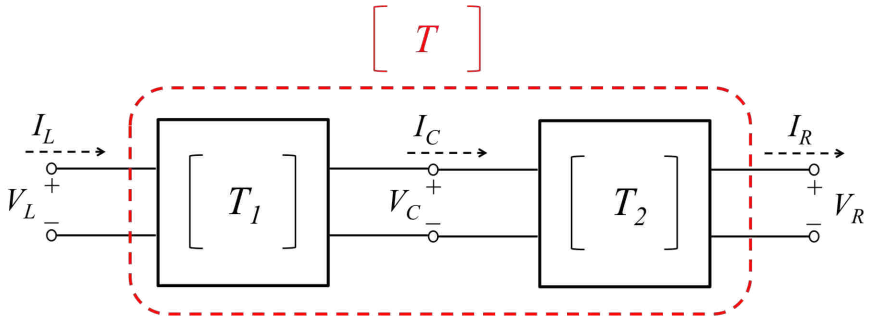

Figure B.2: Schematic diagram of a cascade connection of two two-port devices.

Defining total voltage and current at the i^{th} port as:

$$V_i = V_i^+ + V_i^-, \tag{B.6}$$

$$I_i = I_i^+ - I_i^-, \tag{B.7}$$

where $i = L, C$ or R, the transmission matrix for a two-port network relates the total voltages and currents (Figure B.2):

$$\begin{bmatrix} V_L \\ I_L \end{bmatrix} = \begin{bmatrix} T_{11} & T_{12} \\ T_{21} & T_{22} \end{bmatrix} \begin{bmatrix} V_R \\ I_R \end{bmatrix}. \tag{B.8}$$

The overall transmission matrix can be calculated as:

$$\begin{bmatrix} T_{11} & T_{12} \\ T_{21} & T_{22} \end{bmatrix} = \begin{bmatrix} T_{11}^1 & T_{12}^1 \\ T_{21}^1 & T_{22}^1 \end{bmatrix} \begin{bmatrix} T_{11}^2 & T_{12}^2 \\ T_{21}^2 & T_{22}^2 \end{bmatrix}. \tag{B.9}$$

The scattering matrix of the system can then be calculated as:

$$S = \begin{bmatrix} S_{11} & S_{12} \\ S_{21} & S_{22} \end{bmatrix} = \begin{bmatrix} \frac{T_{11}+\frac{T_{12}}{Z_0}-T_{21}Z_0-T_{22}}{T_{11}+\frac{T_{12}}{Z_0}+T_{21}Z_0+T_{22}} & \frac{2(T_{11}T_{22}-T_{12}T_{21})}{T_{11}+\frac{T_{12}}{Z_0}+T_{21}Z_0+T_{22}} \\ \frac{2}{T_{11}+\frac{T_{12}}{Z_0}+T_{21}Z_0+T_{22}} & \frac{-T_{11}+\frac{T_{12}}{Z_0}-T_{21}Z_0+T_{22}}{T_{11}+\frac{T_{12}}{Z_0}+T_{21}Z_0+T_{22}} \end{bmatrix}, \tag{B.10}$$

where Z_0 is the characteristic impedance of the transmission line [73]. Finally, the power transmission coefficient T_{TL} is defined as:

$$T_{\mathrm{TL}} = \left| \frac{V_R^-}{V_L^+}\Big|_{V_R^+=0} \right|^2 = |S_{21}|^2. \tag{B.11}$$

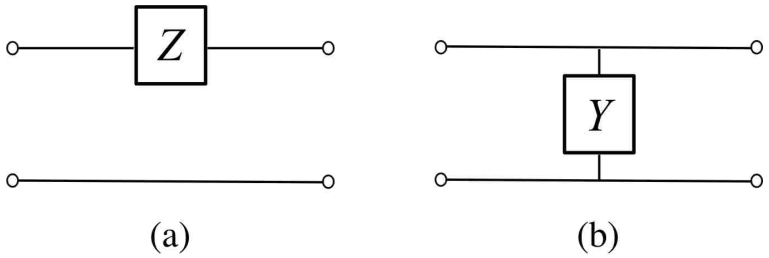

Figure B.3: Equivalent circuit model of series (a) and parallel (b) component in a transmission line model.

In the examples of Chapter 3 the structures are modeled using transmission line theory. Applying transmission line theory and assuming an equivalent circuit model for each component, and depending on whether it is connected in series or in parallel the transmission matrices T_s and T_p can be calculated as [73]:

$$T_s = \begin{bmatrix} 1 & Z \\ 0 & 1 \end{bmatrix}, \tag{B.12}$$

$$T_p = \begin{bmatrix} 1 & 0 \\ Y & 1 \end{bmatrix}, \tag{B.13}$$

where Z is the impedance and $Y = \frac{1}{Z}$ is the conductance of the equivalent circuit model of each component. The product of the individual transmission matrices will give us the

overall transmission matrix which can be used to find the scattering matrix of the system and consequently the power transmission.

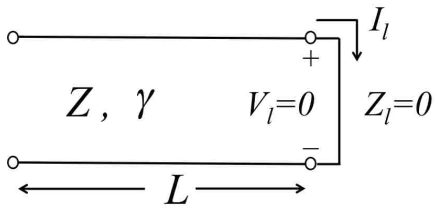

Figure B.4: Equivalent circuit model of a stub resonator which is a short-circuited transmission line resonator with propagation constant γ, and characteristic impedance Z.

Based on transmission line theory, the transmission line model of a stub resonator is a short-circuited transmission line resonator with propagation constant γ, and characteristic impedance Z (Figure B.4), which is connected in series to a transmission line. In our examples the line and the stubs both have the same width, the same propagation constant γ, and correspondingly the same characteristic impedance Z [73, 42] which is given by [41, 42]

$$Z = \frac{\gamma}{j\omega\varepsilon} w. \tag{B.14}$$

The impedance of each stub Z_s which is equivalent with a short-circuited transmission line resonator can be calculated as:

$$Z_s = Z \tanh(\gamma L), \tag{B.15}$$

where L is the length of the stub. Thus, for the first example of Chapter 3 the overall transmission matrix of the model of the structure of Figure 3.2 will be:

$$T = \begin{bmatrix} 1 & Z_{s1} \\ 0 & 1 \end{bmatrix} \begin{bmatrix} 1 & Z_{s2} \\ 0 & 1 \end{bmatrix} = \begin{bmatrix} 1 & Z_{s1} + Z_{s2} \\ 0 & 1 \end{bmatrix}, \tag{B.16}$$

where $Z_{s1} = Z \tanh(\gamma L_1)$ and $Z_{s2} = Z \tanh(\gamma L_2)$. This results in the following scattering matrix:

$$S = \begin{bmatrix} S_{11} & S_{12} \\ S_{21} & S_{22} \end{bmatrix} = \begin{bmatrix} \frac{\tanh(\gamma L_1)+\tanh(\gamma L_2)}{2+\tanh(\gamma L_1)+\tanh(\gamma L_2)} & \frac{2}{2+\tanh(\gamma L_1)+\tanh(\gamma L_2)} \\ \frac{2}{2+\tanh(\gamma L_1)+\tanh(\gamma L_2)} & \frac{\tanh(\gamma L_1)+\tanh(\gamma L_2)}{2+\tanh(\gamma L_1)+\tanh(\gamma L_2)} \end{bmatrix}, \tag{B.17}$$

and the transmission can be calculated as:

$$T_{\mathrm{TL}}(L_1, L_2) = |S_{21}|^2 = \left| 1 + \frac{1}{2}\left[\tanh(\gamma L_1) + \tanh(\gamma L_2) \right] \right|^{-2}. \tag{B.18}$$

The same approach can be applied to the second example with the difference of having a gap between the stub resonators which can be considered as a finite waveguide with length of $L = G$ and characteristic impedance of Z (Figure B.5).

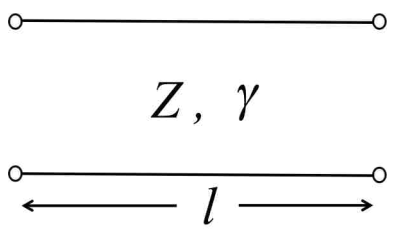

Figure B.5: Equivalent circuit model of a finite waveguide with length l, propagation constant γ, and characteristic impedance Z.

Its transmission matrix can be calculated as:

$$T = \begin{bmatrix} T_{11} & T_{12} \\ T_{21} & T_{22} \end{bmatrix} = \begin{bmatrix} \cosh(\gamma L) & Z\sinh(\gamma L) \\ Y\sinh(\gamma L) & \cosh(\gamma L) \end{bmatrix}. \tag{B.19}$$

Therefore, similarly the overall transmission matrix of the structure of Figure 3.8 can be obtained by the product of transmission matrices of cascaded stubs and waveguides

$$T = \prod_{i=1}^{13} T_i, \tag{B.20}$$

$$T_1 = T_3 = T_5 = \begin{bmatrix} 1 & Z_{s1} \\ 0 & 1 \end{bmatrix} = \begin{bmatrix} 1 & Z\tanh(\gamma L_1) \\ 0 & 1 \end{bmatrix}, \tag{B.21}$$

$$T_7 = T_9 = T_{11} = T_{13} = \begin{bmatrix} 1 & Z_{s2} \\ 0 & 1 \end{bmatrix} = \begin{bmatrix} 1 & Z\tanh(\gamma L_2) \\ 0 & 1 \end{bmatrix}, \tag{B.22}$$

$$T_2 = T_4 = T_6 = T_8 = T_{10} = T_{12} = \begin{bmatrix} \cosh(\gamma G) & Z\sinh(\gamma G) \\ Y\sinh(\gamma G) & \cosh(\gamma G) \end{bmatrix}. \tag{B.23}$$

In the third example of Chapter 3 the structure components are modeled as lumped circuit elements. The silicon and silver nanorods are equivalent to the parallel combination of a resistor, an inductor, and a capacitor. The transmission line model of the waveguide device of Figure 3.11 therefore consists of a shunt impedance Z_t coupled in parallel to a transmission line with characteristic impedance of Z_0 (Figure 3.12). Therefore, similarly the structure can be modeled by a circuit which consists of a parallel component as in Figure B.3(b). The shunt impedance can be calculated as:

$$Z_t = (Z_C^{-1} + R^{-1} + Z_L^{-1})^{-1} = [j\omega C + R^{-1} + (j\omega L)^{-1}]^{-1}. \tag{B.24}$$

Thus, the same approach can be applied to get the transmission matrix of the parallel component with the impedance of Z_t:

$$T = \begin{bmatrix} 1 & 0 \\ \frac{1}{Z_t} & 1 \end{bmatrix}, \tag{B.25}$$

and the scattering matrix of the system can be obtained by Eq. B.10. Correspondingly the power transmission coefficient will be:

$$T_{\mathrm{TL}} = |S_{21}|^2 = \left| \frac{2Z_t}{2Z_t + Z_0} \right|^2. \tag{B.26}$$

Appendix C
Proof of Eq. 4.25

Here we will show that the parts of surface integral I_S

$$I_S = \oiint_S \left(\hat{\mathbf{E}} \times \frac{d\mathbf{H}}{dp} - \frac{d\mathbf{E}}{dp} \times \hat{\mathbf{H}} \right) \cdot d\mathbf{s} = \oiint_S \left(\hat{\mathbf{E}} \times \frac{d\mathbf{H}}{dp} \right) \cdot d\mathbf{s} - \oiint_S \left(\frac{d\mathbf{E}}{dp} \times \hat{\mathbf{H}} \right) \cdot d\mathbf{s}, \quad \text{(C.1)}$$

corresponding to perfect electric conductors (PEC), perfect magnetic conductors (PMC) and radiation/absorbing boundaries (which can be considered as radiation or reflection-free boundary condition, RBC) vanish and it reduces to the integral over the surface of the ports (Eq. 4.19). Applying the boundary condition of PEC, PMC and the radiation/absorbing boundary condition (RBC) for $\mathbf{E}$, $\hat{\mathbf{E}}$ and also $\frac{d\mathbf{E}}{dp}$ to Eq. 4.17 we show that I_S would vanish on them.

At PEC the boundary conditions for $\hat{\mathbf{E}}$ and $\frac{d\mathbf{E}}{dp}$ are:

$$\mathbf{a}_n \times \hat{\mathbf{E}} = 0, \quad \text{(C.2)}$$

$$\mathbf{a}_n \times \frac{d\mathbf{E}}{dp} = 0. \quad \text{(C.3)}$$

From Eq. 4.13 and assuming the medium (device) properties over S are not affected by the perturbation in p (meaning $\frac{d\mu}{dp} = 0$ over S) we get:

$$\frac{d\mathbf{H}}{dp} = -\left(j\omega\mu\right)^{-1} \nabla \times \frac{d\mathbf{E}}{dp}. \quad \text{(C.4)}$$

Using the boundary condition of Eq. C.2 and Eq. C.4 the first term of the right side of Eq. C.1 can be written as:

$$\left(\hat{\mathbf{E}} \times \frac{d\mathbf{H}}{dp}\right) \cdot d\mathbf{s} = \left\{\hat{\mathbf{E}} \times \left[-\left(j\omega\mu\right)^{-1} \nabla \times \frac{d\mathbf{E}}{dp}\right]\right\} \cdot d\mathbf{s} = \left(d\mathbf{s} \times \hat{\mathbf{E}}\right) \cdot \left[-\left(j\omega\mu\right)^{-1} \nabla \times \frac{d\mathbf{E}}{dp}\right] = 0, \tag{C.5}$$

in which we have used the scalar triple product identity. If $\mathbf{a}$, $\mathbf{b}$, and $\mathbf{c}$ are three vectors, we have:

$$\mathbf{a} \cdot (\mathbf{b} \times \mathbf{c}) = \mathbf{c} \cdot (\mathbf{a} \times \mathbf{b}) = \mathbf{b} \cdot (\mathbf{c} \times \mathbf{a}). \tag{C.6}$$

Using Eq. 4.15 and Eq. C.3 the second term of the right side of Eq. C.1 can be written as:

$$\left(\frac{d\mathbf{E}}{dp} \times \hat{\mathbf{H}}\right) \cdot d\mathbf{s} = \left\{\frac{d\mathbf{E}}{dp} \times \left[-\left(j\omega\mu\right)^{-1} \nabla \times \hat{\mathbf{E}}\right]\right\} \cdot d\mathbf{s} = \left(d\mathbf{s} \times \frac{d\mathbf{E}}{dp}\right) \cdot \left[-\left(j\omega\mu\right)^{-1} \nabla \times \hat{\mathbf{E}}\right] = 0, \tag{C.7}$$

in which again scalar triple product identity (Eq. C.6) was used. Thus, substituting Eq. C.5 and Eq. C.7 into Eq. C.1 we get:

$$\iint_{S_{\mathrm{PEC}}} \left(\hat{\mathbf{E}} \times \frac{d\mathbf{H}}{dp} - \frac{d\mathbf{E}}{dp} \times \hat{\mathbf{H}}\right) \cdot d\mathbf{s} = 0, \tag{C.8}$$

where S_{PEC} is the part of S corresponding to perfect electric conductors (PEC).

We then consider a PMC portion of S, S_{PMC}. At PMC the boundary conditions for $\hat{\mathbf{E}}$ and $\frac{d\mathbf{E}}{dp}$ are:

$$\mathbf{a}_n \times \left(\nabla \times \hat{\mathbf{E}}\right) = 0, \tag{C.9}$$

$$\mathbf{a}_n \times \left(\nabla \times \frac{d\mathbf{E}}{dp} \right) = 0. \tag{C.10}$$

Using the boundary condition of Eq. C.10 and Eq. C.4 the first term of the right side of Eq. C.1 can be written as:

$$\left(\hat{\mathbf{E}} \times \frac{d\mathbf{H}}{dp} \right) \cdot d\mathbf{s} = \left\{ \hat{\mathbf{E}} \times \left[-\left(j\omega\mu\right)^{-1} \nabla \times \frac{d\mathbf{E}}{dp} \right] \right\} \cdot d\mathbf{s} = \hat{\mathbf{E}} \cdot \left\{ \left[-\left(j\omega\mu\right)^{-1} \nabla \times \frac{d\mathbf{E}}{dp} \right] \times d\mathbf{s} \right\} = 0. \tag{C.11}$$

By using Eq. 4.15 and Eq. C.10, and assuming that we have a reciprocal medium ($\mu^T = \mu$), , the second term of the right side of Eq. C.1 can be written as:

$$\left(\frac{d\mathbf{E}}{dp} \times \hat{\mathbf{H}} \right) \cdot d\mathbf{s} = \left\{ \frac{d\mathbf{E}}{dp} \times \left[-\left(j\omega\mu\right)^{-1} \nabla \times \hat{\mathbf{E}} \right] \right\} \cdot d\mathbf{s} = \left(\frac{d\mathbf{E}}{dp} \right) \cdot \left\{ \left[-\left(j\omega\mu\right)^{-1} \nabla \times \hat{\mathbf{E}} \right] \times d\mathbf{s} \right\} = 0. \tag{C.12}$$

Inserting Eq. C.11 and Eq. C.12 into Eq. C.1 we get:

$$\iint_{S_{\mathrm{PMC}}} \left(\hat{\mathbf{E}} \times \frac{d\mathbf{H}}{dp} - \frac{d\mathbf{E}}{dp} \times \hat{\mathbf{H}} \right) \cdot d\mathbf{s} = 0, \tag{C.13}$$

where S_{PMC} is the part of S corresponding to perfect magnetic conductors (PMC).

At RBC the boundary conditions for $\hat{\mathbf{E}}$ and $\frac{d\mathbf{E}}{dp}$ are [45]:

$$\nabla \times \hat{\mathbf{E}} = -\gamma \left(\mathbf{a}_n \times \hat{\mathbf{E}} \right), \tag{C.14}$$

$$\nabla \times \frac{d\mathbf{E}}{dp} = -\gamma \left(\mathbf{a}_n \times \frac{d\mathbf{E}}{dp} \right). \tag{C.15}$$

By using the boundary condition of Eqs. C.15 and C.4, the first term of the right side of Eq. C.1 can be written as:

$$\left(\hat{\mathbf{E}} \times \frac{d\mathbf{H}}{dp}\right) \cdot d\mathbf{s} = \left\{\hat{\mathbf{E}} \times \left[-\left(j\omega\mu\right)^{-1} \nabla \times \frac{d\mathbf{E}}{dp}\right]\right\} \cdot d\mathbf{s} = \left\{\hat{\mathbf{E}} \times \left[\gamma \left(j\omega\mu\right)^{-1} \left(\mathbf{a}_n \times \frac{d\mathbf{E}}{dp}\right)\right]\right\} \cdot d\mathbf{s}$$
$$= \gamma \left(j\omega\mu\right)^{-1} \left[\mathbf{a}_n \left(\hat{\mathbf{E}} \cdot \frac{d\mathbf{E}}{dp}\right) - \frac{d\mathbf{E}}{dp} \left(\hat{\mathbf{E}} \cdot \mathbf{a}_n\right)\right] \cdot d\mathbf{s}, \quad \text{(C.16)}$$

in which we have used the vector triple product identity:

$$\mathbf{a} \times (\mathbf{b} \times \mathbf{c}) = \mathbf{b} \left(\mathbf{a} \cdot \mathbf{c}\right) - \mathbf{c} \left(\mathbf{a} \cdot \mathbf{b}\right). \quad \text{(C.17)}$$

By using Eqs. 4.15 and C.14, the second term of the right side of Eq. C.1 can be written as:

$$\left(\frac{d\mathbf{E}}{dp} \times \hat{\mathbf{H}}\right) \cdot d\mathbf{s} = \left\{\frac{d\mathbf{E}}{dp} \times \left[-\left(j\omega\mu\right)^{-1} \nabla \times \hat{\mathbf{E}}\right]\right\} \cdot d\mathbf{s} = \left\{\frac{d\mathbf{E}}{dp} \times \left[\gamma \left(j\omega\mu\right)^{-1} \left(\mathbf{a}_n \times \hat{\mathbf{E}}\right)\right]\right\} \cdot d\mathbf{s}$$
$$= \gamma \left(j\omega\mu\right)^{-1} \left[\mathbf{a}_n \left(\frac{d\mathbf{E}}{dp} \cdot \hat{\mathbf{E}}\right) - \hat{\mathbf{E}} \left(\frac{d\mathbf{E}}{dp} \cdot \mathbf{a}_n\right)\right] \cdot d\mathbf{s}. \quad \text{(C.18)}$$

By inserting Eqs. C.11 and C.12 into Eq. C.1, the two terms of surface integral I_S cancel each other and we get:

$$\iint_{S_{\text{RBC}}} \left(\hat{\mathbf{E}} \times \frac{d\mathbf{H}}{dp} - \frac{d\mathbf{E}}{dp} \times \hat{\mathbf{H}}\right) \cdot d\mathbf{s} = 0, \quad \text{(C.19)}$$

where S_{RBC} is the part of S corresponding to radiation/absorbing boundaries (RBC). Thus, as shown above, the surface integral I_S would be zero and vanish on all PEC, PMC, and RBC portions of S and the only part of it which remains is over the port cross sections:

$$I_S = \sum_i \iint_{S_i} \left(\hat{\mathbf{E}} \times \frac{d\mathbf{H}}{dp} - \frac{d\mathbf{E}}{dp} \times \hat{\mathbf{H}}\right) \cdot d\mathbf{s}. \quad \text{(C.20)}$$

Appendix D
Boundary Conditions

To define the boundary condition for each port of our device (S_1 and S_2) let us assume that the waveguide ports are operating at a frequency at which only the dominant mode can propagate. For simplicity we consider the case that only tangential electric fields exist. Furthermore, let us assume that S_1 and S_2 are placed sufficiently far from the device, so that higher order modes which may be excited by the device die out before they reach S_1 and S_2.

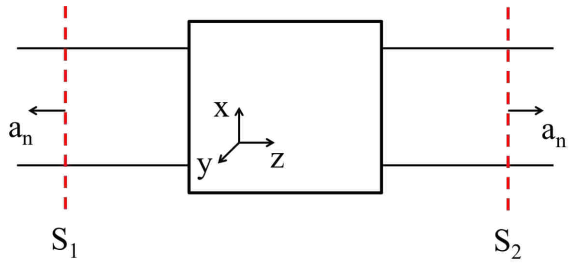

Figure D.1: A two-port device.

When the excitation is at port 1, the total electric field at S_1 can be expressed as a superposition of an incident wave $\mathbf{E}^{\text{inc}}$ and a reflected wave $\mathbf{E}^{\text{ref}}$:

$$\mathbf{E}_1 = \mathbf{E}_1^{\text{inc}} + \mathbf{E}_1^{\text{ref}} = E_0 \left(\hat{\mathbf{e}}_{1x} e^{-\gamma z} + \hat{\mathbf{e}}_{1y} e^{-\gamma z}\right) + R E_0 \left(\hat{\mathbf{e}}_{1x} e^{\gamma z} + \hat{\mathbf{e}}_{1y} e^{\gamma z}\right), \tag{D.1}$$

where E_0 denotes the magnitude of the incident electric field, $\mathbf{e}_{1x}$ and $\mathbf{e}_{1y}$ are the modal field vectors, R denotes the reflection coefficient, and γ is the propagation constant. From Eq. D.1 we obtain:

$$\mathbf{a}_n \times (\nabla \times \mathbf{E}_1) = \mathbf{a}_n \times \left[\nabla \times \left(\mathbf{E}_1^{\text{inc}} + \mathbf{E}^{\text{ref}}\right)\right] = -\mathbf{a}_z \times \left(\nabla \times \mathbf{E}_1^{\text{inc}}\right) - \mathbf{a}_z \times \left(\nabla \times \mathbf{E}^{\text{ref}}\right)$$

$$= \left(\mathbf{a}_{1y} \times \frac{dE_{1y}^{\text{inc}}}{dz} + \mathbf{a}_x \times \frac{dE_{1x}^{\text{inc}}}{dz} \right) + \left(\mathbf{a}_y \times \frac{dE_y^{\text{ref}}}{dz} + \mathbf{a}_x \times \frac{dE_x^{\text{ref}}}{dz} \right)$$

$$= -\gamma \mathbf{E}_1^{\text{inc}} + \gamma \mathbf{E}^{\text{ref}} = -\gamma \mathbf{E}_1^{\text{inc}} + \gamma \left(\mathbf{E}_1 - \mathbf{E}_1^{\text{inc}} \right) = \gamma \mathbf{E}_1 - 2\gamma \mathbf{E}_1^{\text{inc}}, \tag{D.2}$$

which can also be written as:

$$\mathbf{a}_n \times (\nabla \times \mathbf{E}_1) + \gamma \mathbf{a}_n \times (\mathbf{a}_n \times \mathbf{E}_1) = -2\gamma \mathbf{E}_1^{\text{inc}}. \tag{D.3}$$

If we define the linear operator P as:

$$P(\mathbf{E}_1) \equiv \gamma \mathbf{a}_n \times (\mathbf{a}_n \times \mathbf{E}_1), \tag{D.4}$$

then Eq. D.3 can be rewritten as:

$$\mathbf{a}_n \times (\nabla \times \mathbf{E}_1) + P(\mathbf{E}_1) = \mathbf{U}_1^{\text{inc}}, \tag{D.5}$$

where:

$$\mathbf{U}_1^{\text{inc}} \equiv -2\gamma \mathbf{E}_1^{\text{inc}} = 2\gamma \mathbf{a}_n \times \left(\mathbf{a}_n \times \mathbf{E}_1^{\text{inc}} \right) = 2P \left(\mathbf{E}_1^{\text{inc}} \right). \tag{D.6}$$

Similarly, the electric field at S_2 which is the transmitted wave $\mathbf{E}^t$ can be expressed as:

$$\mathbf{E}_1 = \mathbf{E}^t = T\mathbf{E}_0 \left(\hat{e}_{2x} e^{-\gamma z} + \hat{e}_{2y} e^{-\gamma z} \right). \tag{D.7}$$

where T denotes the transmission coefficient. Thus we have:

$$\mathbf{a}_n \times (\nabla \times \mathbf{E}_1) = \mathbf{a}_z \times (\nabla \times \mathbf{E}_1) = -\mathbf{a}_y \times \frac{dE_{1y}}{dz} - \mathbf{a}_x \times \frac{dE_{1x}}{dz} = \gamma \mathbf{E_1}, \tag{D.8}$$

which can also be written as:

$$\mathbf{a}_n \times (\nabla \times \mathbf{E}_1) = -P(\mathbf{E}_1). \tag{D.9}$$

Using the fact that in this case, when the excitation is from port 1, then the wave at S_2 is an output wave satisfying Maxwell's equations, we can get:

$$P(\mathbf{E}_1) = -\mathbf{a}_n \times (-j\omega\mu \cdot \mathbf{H}_1), \tag{D.10}$$

where $\mathbf{H}_1$ is the magnetic field when the excitation is at port 1. Knowing that P is a linear vector operator, we can use the modal vectors $\mathbf{e_2}$, $\mathbf{h_2}$ at port 2 and write Eq. D.10 as:

$$P(\mathbf{e_2}) = -\mathbf{a}_n \times (-j\omega\mu \cdot \mathbf{h_2}) = \mathbf{a}_n \times (j\omega\mu \cdot \mathbf{h_2}). \tag{D.11}$$

Also for the adjoint problem, when the excitation is at port 2, the boundary condition at S_1 is:

$$\mathbf{a}_n \times \left(\nabla \times \hat{\mathbf{E}}_2\right) + P\left(\hat{\mathbf{E}}_2\right) = 0, \tag{D.12}$$

and at S_2 is:

$$\mathbf{a}_n \times \left(\nabla \times \hat{\mathbf{E}}_2\right) + P\left(\hat{\mathbf{E}}_2\right) = \hat{\mathbf{U}}_2^{\text{inc}}, \tag{D.13}$$

where

$$\hat{\mathbf{U}}_2^{\text{inc}} = 2P\left(\hat{\mathbf{E}}_2^{\text{inc}}\right). \tag{D.14}$$

Vita

Pouya Dastmalchi was born in 1984 in Rasht, Iran. He graduated from Mirza Koochak Khan High School (NODET) in 2002. He proceeded to get his B.Sc. and M.Sc. in electrical engineering from the Khaje Nasir Toosi University of Technology (KNTU) in Tehran in 2007 and 2010, respectively. In August 2011 he came to Louisiana State University to pursue graduate studies. He is currently a candidate for Doctor of Philosophy degree in Electrical Engineering which will be awarded in December 2015.